Investigations of the Generation of Tunable Continuous-Wave Terahertz Radiation and Its Spectroscopic Applications

Vom Fachbereich Physik
der Technischen Universität Darmstadt

zur Erlangung des Grades
eines Doktors der Naturwissenschaften
(Dr. rer. nat.)

genehmigte Dissertation von
Dipl.-Phys. Icksoon Park
aus Yeonsan/Südkorea

Referent: Prof. Dr. W. Elsäßer
Korreferent: Prof. Dr. P. Meißner

Tag der Einreichung: 05.12.2006
Tag der Prüfung: 29.01.2007

Darmstadt 2007
D17

Contents

Chapter 1

Introduction

In the past two decades, the era of a before difficult accessible frequency region in the electromagnetic spectrum has been opened in science. This is the Terahertz (THz) frequency region. The Terahertz ($1\,\mathrm{THz} = 10^{12}\,\mathrm{Hz}$) region is usually defined as the frequency range between 0.1 THz and 10 THz corresponding to wavelength range from 3 mm to 30 μm and lies between the microwave and the infrared light regime. While both neighboring frequency regions have been extensively investigated and developed, the THz region remained the least explored region, commonly known as the THz gap. This is because of the lack of efficient sources and detectors in the THz region. However, starting with picosecond optoelectronic switching in silicon [1], the THz gap has recently begun to be filled with huge progress devoted to research for new sources and detectors. This progress in THz technology has also woken the immense interest for its applications in many areas. Most fundamental molecules (e.g. water, oxygen and carbon monoxide) and chemical substances have their rotational and vibrational absorption lines in the THz range. THz radiation penetrates many non-polar and non-metallic materials such as paper, textiles, woods and plastics. However, THz radiation is reflected by metals and is absorbed by polar molecules such as water. THz radiation is non-ionizing and is not harmful for living cells. Such characteristic features attract the rising interest for THz applications in many areas such as basic science, manufacturing, security, medicine and broadband THz communications.

One of the potential applications for THz technology can be found in the astronomical and atmospheric spectroscopy. Many spectral lines emitted by interstellar dust clouds fall in the THz region and several of these have not yet been identified. Approximately 50 % of the total luminosity and 98 % of the photons emitted since the Big-Bang fall into the THz region [2]. Interstellar space or planetary atmospheres can be monitored for water, oxygen, and carbon monoxide. Sensing of the atmosphere of the Earth can provide insight into ozone formation and destruction. Since many gases exhibit characteristic absorption spectra in the THz region arising from rotational quantum transitions, THz radiation can be used for gas monitoring and analysis of gas mixtures by identifying these rotational absorption spectra. THz radiation is adequate for ap-

plications in nondestructive inspection and security screening of packages, mails and luggage at airport for explosives, non-metallic weapons, chemical agents and drugs. Since many package materials such as cardboard, plastics, and paper are transparent to THz radiation, THz radiation allows to image objects inside packages made of such materials [3, 4]. The transmission or reflection patterns versus frequency of concealed objects provide signatures specific to the chemical composition of the objects. Explosives, drugs, chemical and biological agents have their characteristic spectra in the THz region. THz spectroscopy allows to analyze and identify such substances contained in a package [5]. THz imaging can also be used for quality control in manufacturing processes. For example, voids inside soft materials such as plastics can be detected by observing a change in the THz transmission through the sample. In contrast, X-ray transmission provides only low contrast between air and soft materials. Biomedical imaging is another potential THz application. Since THz radiation is strongly absorbed by water, differences in water content in tissue give an imaging contrast. Even biological constituents have distinct signatures responding to THz radiation. For example, THz imaging can reveal the contrast between healthy tissue and cancer [6] or can be used for DNA analysis [7]. THz radiation also finds its applications in the basic research such as fundamental processes in semiconductors [8]. Moreover, the THz region offers the possibility of THz communications with larger bandwidth compared to microwave communications, but with a restriction due to strong absorption by water vapor in the atmosphere. Most of these potential applications are currently under investigation.

Such huge interest in the THz technology and its applications drives considerable research activity for efficient THz sources and sensitive detectors. Due to the fact that the THz region lies between electronics and photonics with respect to the accessible spectral region, a variety of THz sources have been developed from electronics, optics and a mixture of both. There are several ways to detect THz radiation, e.g., thermal detectors such as Golay cells and helium cooled bolometers, photoconductive [9, 10] and electro-optic detection [11, 12]. In particular, the photoconductive and electro-optic detection can provide information on both amplitude and phase of THz radiation. The most challenging part of THz technologies is the realization of efficient THz sources. Meanwhile, several methods for THz generation have been developed, which can be classified into two classes: broadband (pulse) and narrowband (continuous-wave) sources. Most broadband THz sources are based on the generation of pulsed THz radiation by exciting materials with ultrashort laser pulses, using mechanisms such as carrier acceleration in photoconductive antennas [13, 14], optical rectification in nonlinear media [15] and surface current at semiconductors [16, 17]. The pulsed THz sources enable broadband THz spectroscopy, termed THz time-domain spectroscopy (THz-TDS), up to 50 THz [18] with a snapshot, but they give a low spectral resolution of several tens of GHz.

Compared to pulsed THz sources, continuous-wave (CW) THz sources provide a THz spectrum with a narrower linewidth and a higher spectral THz power. CW THz sources are of considerable significance for high-resolution THz spectroscopy, THz sensing and broadband THz communications. Gunn diodes, backward wave oscillators, CO_2-laser pumped gas laser, nonlinear optical difference frequency generation [19], optical parametric oscillators [20], free-electron lasers, quantum cascade lasers [21] and photomixers [22] belong to CW THz sources.

Broadband tunability and power levels of at least tens of microwatt are highly desirable for CW THz spectroscopy. In addition, it is also desirable that the THz source is compact, cost-efficient and operating at room temperature. Some CW THz sources discussed above can deliver sufficient power. However, they are bulky, expensive and have a limited frequency-tunability. CW THz sources that are compact and tunable throughout the frequency range from 100 GHz to 10 THz with tens of microwatt power levels still remain a technological challenge. A portable THz source enables THz technologies to be expanded on a large scale to commercial applications in security sensing, luggage inspection and medical diagnostics in practics. A simple configuration of THz sources even is desired for easy maintenance of the devices. Moreover, the stability of THz radiation is a requirement for reliable measurements.

In order to realize such CW THz sources, photomixing is the most potential technique. Photomixing uses two frequency laser beams to generate carrier-modulation on a prebiased photoconductor (i.e., a photomixer) that has a carrier lifetime shorter than 1 picosecond. The photocurrent is modulated at the difference (beat) frequency of two laser beams and is coupled to an antenna, which subsequently couples out THz radiation. The generated THz radiation can have a narrow linewidth and can be tuned over the THz frequency range by varying the difference frequency of the two laser beams. For THz generation by photomixing, the stability of THz radiation is linked to the stability of the optical beat signals. Therefore, the realization of a stable optical beat signal is essential for stable THz radiation. Here, dual-mode lasers have certain advantages to achieve such stability. A dual-mode laser can provide frequency-stable beat signals. Two modes propagating through the same laser cavity experience in large part the same fluctuations. Thus, such fluctuations in each mode compensate each other at the beat frequency so that the beat frequency is more stable than the frequency of each optical mode. Thus, the linewidth of the beat signal is expected to be narrower than that of each mode. Additionally, since the two modes propagate collinearly, the spatial overlap of the two modes can be inherently achieved. Especially the stable beat frequency and the inherent spatial overlap of the two laser modes raise hopes of realizing a high quality THz radiation source by means of a dual-mode laser.

For realization of compact, cost-efficient optical sources, semiconductor lasers are very

attractive. Semiconductor lasers are compact with a size of millimeters or smaller and cost-efficient. They have high wall-plug efficiencies of more than 50 %, long device lifetimes, and a broad gain spectrum which enables a wide frequency-tunability of more than 20 THz by using frequency-selective tuning methods. Furthermore, high-power semiconductor lasers with CW output powers of several watts are commercially available. Therefore, semiconductor lasers are potential optical sources to achieve widely tunable dual-mode operation with high power. In addition to scientific attraction of THz technologies, such advantages of semiconductor lasers motivate the present work.

The aim of this work is the realization of stable CW THz radiation sources, the frequency of which is tunable in the THz frequency range between 0.1 and 10 THz. This is achieved via photomixing of two simultaneously oscillating modes emitted from one semiconductor laser medium. Furthermore, the generated THz radiation by the realized THz radiation-source should be capable of applications such as spectroscopy and gas sensing.

The present work is organized as follows:

In chapter 2, a short introduction to semiconductor lasers, external cavity lasers, dual-mode theory and dynamics are given. On the basis of spectrally selected feedback using an external cavity configuration, two concepts for frequency-tunable dual-mode semiconductor lasers are developed and experimentally realized. By employing narrow stripe semiconductor lasers as gain medium, the frequency-tunability and emission characteristics of the realized dual-mode external cavity semiconductor lasers (2λ-ECSLs) are investigated. During dual-mode operation of the SL, four-wave mixing (FWM) signals are generated due to nonlinear interactions of the intense laser field and the semiconductor medium. In chapter 3, frequency-tunable CW THz radiation is generated via photomixing by applying the realized 2λ-ECSLs. Firstly, general principles of photomixing, photoconductive materials and antennas are discussed. Secondly, the experimental setup for THz generation and its detection methods are described. Subsequently, the generation of THz radiation is investigated and the generated THz radiation is temporally and spectrally analyzed. Furthermore, the polarization characteristics of THz radiation are investigated. In chapter 4, the realized THz-system is tested in spectroscopic applications comprising THz transmission studies of several materials and absorption spectra of HCl and H_2O molecules. In chapter 5, high-power broad area semiconductor lasers (BALs) are employed as gain mediums, forming a dual-mode external cavity BAL (2λ-ECBAL) configuration. Firstly, THz radiation is generated by photomixing and spectrally characterized. Since BALs generally exhibit the multitude of lateral modes in addition to many longitudinal modes, the principle of spatially filtered feedback is employed in the 2λ-ECBAL for lateral mode control. Longitudinal dual-mode operation with single lateral mode emission of BALs is inves-

tigated and the total intensity modulation is studied. Finally, spectrally and spatially controlled dual-mode emission of BALs is investigated in detail. In chapter 6, FWM phenomena observed for dual-mode operation of narrow stripe SL are studied in detail. Since this nonlinear optical processes in the SL indicates a possibility of direct generation of THz radiation in SL itself, direct THz generation in SL is investigated. In the final chapter, the results obtained in this work are summarized.

Chapter 2

Tunable Dual-Mode Semiconductor Lasers

Dual-mode lasers are attractive optical sources for photomixing due to the possibility of their stable beat frequencies and inherent spatial overlap of two laser modes. There have been many studies for the realization of dual-mode lasers, including solid-state lasers [23], fiber lasers [24, 25], and semiconductor lasers (SLs) [26, 27, 28, 29, 30, 31, 32], which are still a subject of research. In particular, a single dual-mode SL that provides a compact configuration, a wide frequency-tunability [33] and high output power is desirable for application in generation of tunable THz radiation. For such a light source, a frequency-tunable dual-mode SL employing an external cavity configuration is a potential optical source for photomixing.

In this chapter, frequency-tunable dual-mode SLs in external double-cavity configurations will be investigated. First, a short introduction to SLs, tunable external cavity configurations, and dual-mode theory will be given. Finally, two concepts for realization of frequency-tunable dual-mode external cavity SLs will be studied. The emission characteristics and frequency-tunability of dual-mode operation will be discussed in detail.

2.1 Semiconductor Lasers

Semiconductor lasers are among the most important coherent light sources in modern technologies. Wide applications for research and commercial purposes originate from their distinguishable features. SLs are directly pumped by injecting electrical current into them and have a low electrical power consumption, high conversion efficiencies from electric to optical power exceeding 50 %, broad bandwidth range and a low price per piece. The capability of their output modulation by high-speed direct current modulation even make them a key component in optical communications. Additionally, their overall small size enable them to be integrated monolithically with electronic circuits, forming optoelectronic devices. These achievements are based on the progress in fundamental research of SLs and manufacturing technology.

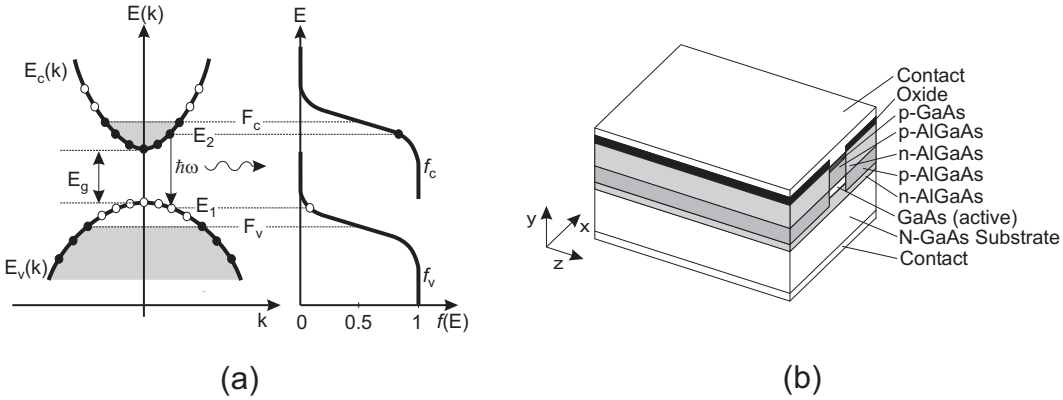

Fig. 2.1: Schematic of parabolic band structure $E(k)$ in a direct semiconductor (left) and quasi-Fermi-distributions $f(E)$ (right) (a) and an index-guided semiconductor laser (b). Open circles represent empty states and the dark circles represent occupied states. The coordinates x, y and z represent the lateral, transversal and axial direction. From Ref. [34]

2.1.1 Principle of Semiconductor Lasers

For lasing operation, the optical gain achieved by the stimulated emission must exceed the optical losses, which requires population inversion in the laser medium. For SL, the population inversion is achieved by forming a *p*-*n* junction of n- and p-doped semiconductors. When the forward bias is applied across the junction, a population-inverted layer (active layer) is created in the *p*-*n* junction. In this active layer, stimulated emission occurs due to electron-hole recombination. The two cleaved crystal facets of the semiconductor perpendicular to the junction plane provide the optical feedback. The population inversion is maintained via carrier injection by an external power supply.

On the left hand side of Fig. 2.1(a), an inverted energy band structure $E(k)$ is displayed for a direct semiconductor in which the minimum of the conduction band lies at the same k-value as the maximum of the valence band. The right hand side shows the corresponding quasi-Fermi distributions in both bands. Under current injection, charged carriers (both electrons and holes) are injected into the conduction and valence bands and the semiconductor is in thermal nonequilibrium state. Through the ultrafast carrier-carrier scattering ($< 1\,\mathrm{ps}$), the carriers are in thermal quasi-equilibrium within each band, before the interband transition (time-scale of the order of nanoseconds) occurs. The carrier distribution within each band is described by the quasi-Fermi-Dirac functions f_c for conduction band and f_v for valence band,

$$f_{\mathrm{c}}(E,T) = \frac{1}{e^{(E-F_{\mathrm{c}})/k_{\mathrm{B}}T}+1} \qquad \textit{and} \qquad f_{\mathrm{v}}(E,T) = \frac{1}{e^{(E-F_{\mathrm{v}})/k_{\mathrm{B}}T}+1}, \tag{2.1}$$

with the corresponding quasi-Fermi energy levels F_{c} and F_{v}. The position of quasi-Fermi levels depends on the carrier density and the temperature. If the condition

$$E_{\mathrm{g}} < E_2 - E_1 = \hbar\omega < F_{\mathrm{c}} - F_{\mathrm{v}} \tag{2.2}$$

is satisfied, where E_{g} represents the energy gap between the conduction and valence band, the stimulated electron-hole recombination dominates the absorption and other losses and the lasing operation is achieved. The relation $E_2 - E_1 = \hbar\omega$ with $E_1 < E_2$ represents energy conservation for the transition from E_2 to E_1. Due to momentum conservation and negligible photon momentum in comparison to the momentum of the carriers, the radiative interband transitions occur only at the same k-vector.

The most common SL structures are edge-emitting SLs. Figure 2.1(b) shows a schematic of an index-guided edge-emitting SL. Generally, the active region is embedded between two cladding layers of a higher band gap and a lower refractive index than those of the active layer. This double-heterostructure confines not only carriers to the active region due to the band gap difference but also optical modes close to the active region due to the refractive index difference. This provides carrier- and optical mode-confinement in the transversal direction of the SL. Lateral confinement of the optical mode is achieved via spatially restricted current injection (gain-guided structure) or by implementing a lateral refractive index step (index-guided structure). With the progress in growth techniques, the thickness of the active layer can be reduced to about 5 nm, forming quantum-well (QW) structures, however, then deserving additional waveguiding layers. QW SLs exhibit small threshold current, low temperature sensitivity and excellent modulation characteristics. Most of todays commercial SLs are QW structures.

2.1.2 Tunable External Cavity Semiconductor Lasers (ECSLs)

Frequency-tunable SLs have been extensively studied and are still a subject of investigation due to their potential application in many areas such as atomic spectroscopy and optical communications [35]. The tuning of lasing wavelength (i.e. frequency) of a SL can be achieved, e.g. by changing the temperature of the SL or the injection current into the SL. Monolithic tunable lasers are another method for frequency-tuning, e.g. b multi-segment structures. Such lasers have a periodic structure in the laser cavity in the form of a distributed feedback (DFB) or a distributed Bragg reflector (DBR). The frequency tuning is achieved by changing the injection current into the laser. A tuning

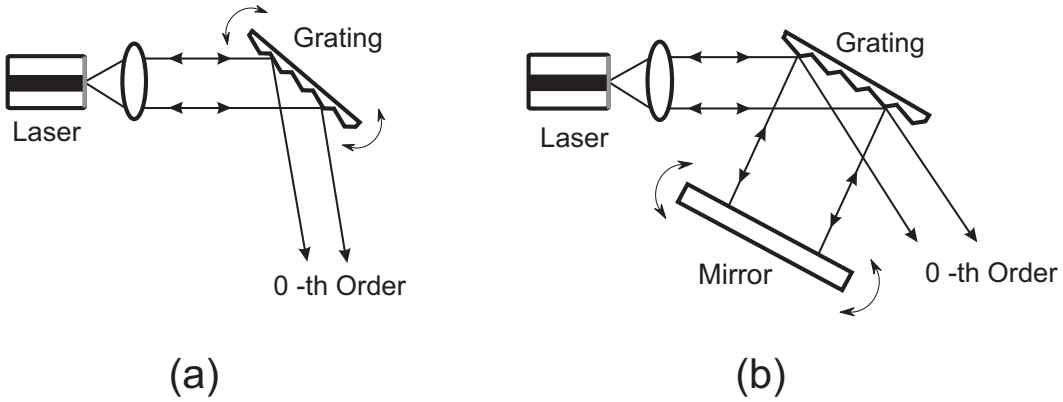

Fig. 2.2: Schematic for external cavity lasers in (a) Littrow and (b) Littman-Metcalf configuration.

range of 114 nm has been reported [36]. However, these methods are not appropriate for applications which need wide frequency-tuning with a constant optical power, because the optical power of SLs using such methods changes with the frequency-tuning.

A simple approach for wide frequency-tuning of SLs is using external cavity configuration comprising a SL as a gain medium, frequency-selective filters, and mirrors for feedback. The frequency selection and tuning are performed external to the SL medium. For stable operation of the SL on an externally selected frequency, the laser facet facing the external cavity is antireflection coated. As a frequency-selective filter, a diffraction grating, an interference filter (Fabry-Perot etalon), an acoustooptic tunable filter, or a birefrigent filter can be used. The principle of the frequency-tuning is the spectrally filtered feedback of a resonant mode in the external cavity. Such tunable external cavity SLs (ECSLs) are advantageous in comparison to solitary SLs. The linewidth of ECSLs is reduced due to the longer photon lifetime in the external cavity. Moreover, SLs have a wide gain bandwidth of several tens of nanometer. Therefore, wide tuning range can be achieved by using a proper filter. Two simple ECSL-configurations using a diffraction grating are schematically depicted in Fig. 2.2. One concept is the so-called Littrow-configuration [37], as shown in Fig. 2.2(a). The collimated beam from the AR-coated front facet is incident onto a reflection grating. The zeroth-order diffraction beam is coupled out as output for applications. The first order diffraction beam of the grating is angularly dispersed depending on the frequency. The frequency-tuning is accomplished as the desired frequency is reflected back into the laser by tilting the grating. Here, the grating plays the role of both filter and mirror so that the laser resonator is composed of the rear-facet of the SL and the external grating. This configuration is simple and compact. However, the output beam displaces as the grating is tilted. This is disadvantageous for applications which need constant output direction.

Moreover, the frequency selectivity is relatively low because only a small number of the grating-grooves are illuminated. An alternative external cavity concept is the so-called Littman-Metcalf-configuration (in short, Littman-configuration) [38, 39, 40, 41], which is shown in Fig. 2.2(b). The collimated output beam of SL is incident onto a grating. The first-order diffraction beam of the grating is directed onto a high-reflective external mirror. The frequency-tuning is achieved by tilting the mirror and feeding the selected frequency back onto the grating and subsequently into the laser. Hence, the laser resonator consists of the rear-facet and the external mirror. The zeroth-order beam is used as output. This configuration provides a constant output direction and better mode-selectivity due to large number of illuminated grating-grooves and the fact that the light is dispersed twice by the grating. However, the output power is lower than that of the Littrow-configuration. These external cavity concepts are simple and compact and provide a wide frequency-tuning range. A wide tuning range of even 240 nm at a center wavelength of 1.5 μm has been reported in [42].

The frequency tunability of SL using a single external cavity allows for a possibility to realize a frequency-tunable dual-mode SL using an external double-cavity. Therefore, the external cavity configuration is a potential method for frequency-tunable dual-mode SLs. In the following sections, dual-mode emission of SL will be discussed.

2.1.3 Dual-Mode Theory

Dual-mode operation is the simplest form of multimode operation of a laser and has gained interest some in research [43, 44, 45, 46, 47]. Two modes compete for the available gain in the laser and oscillation of one mode reduces the gain available for the other. The dual-mode operation of the laser can be described in a simplified model by the rate equations [43] for the intensities I_1 and I_2 of the two modes 1 and 2, respectively,

$$\frac{dI_1}{dt} = (\alpha_1 - \beta_1 I_1 - \theta_{12} I_2) I_1 \tag{2.3}$$

$$\frac{dI_2}{dt} = (\alpha_2 - \beta_2 I_2 - \theta_{21} I_1) I_2, \tag{2.4}$$

where α_i is the unsaturated net gain for the ith mode, β_i is the self-saturation coefficient, and θ_{ij} is the cross-saturation coefficient. In a steady state, these equations give solutions for I_1 and I_2, which are related by a coupling constant

$$C \equiv \frac{\theta_{12}\theta_{21}}{\beta_1 \beta_2}. \tag{2.5}$$

Depending on the value of C, the coupling strengths are classified into three cases. For $C = 1$ (neutral coupling), only one mode oscillates and the other is suppressed. For $C > 1$ (strong coupling), a single-mode operation of one of the modes is stable and the dual-mode operation is unstable. That is, even if the two modes initially start to oscillate simultaneously, small perturbations will cause the laser to a single-mode operation of only one of the modes. When $C < 1$ (weak coupling), both modes oscillate simultaneously and share the same gain medium. Under this condition, the stability of dual-mode operation can be strongly supported by spatial hole burning and spontaneous emission [48].

In particular, the stabilization of the difference frequency of the two modes is of significant importance because it will play an important role for the frequency-stability of the THz radiation. In this point, dual-mode lasers provide frequency-stable beat signals [49]. For a heterodyne method employing two independent lasers, the fluctuations of each mode are statistically random and the fluctuations of their difference frequency are additive. Therefore, the difference frequency is less stable than each laser mode. In comparison, for a dual-mode laser, the two coaxial modes share the same laser cavity. The frequencies of the two modes can then be expressed by $f_1 = m_1 c/2L$ and $f_2 = m_2 c/2L$, where m_1 and m_2 are two integers, c is the velocity of light in vacuum, and L is the optical path-length in the cavity. When f_1 and f_1 are differentiated with respect to L, the relation

$$\frac{\Delta f_i}{f_i} = \frac{\Delta f_2 - \Delta f_1}{f_{21}} = -\frac{\Delta L}{L}, \qquad i = 1, 2, \tag{2.6}$$

holds, where Δf_i represents fluctuations of f_i and $f_{21} = f_2 - f_1$. Since f_1 and f_2 follow fluctuations of L in phase, the fluctuations Δf_{21} of their difference frequency are subtractive giving $\Delta f_{21} = \Delta f_2 - \Delta f_1$. For $f_1 \simeq f_2 \gg f_{21}$, equation (2.6) gives then

$$\Delta f_1 \simeq \Delta f_2 \qquad \text{and} \qquad \Delta f_{21} \ll \Delta f_i, \qquad i = 1, 2. \tag{2.7}$$

Equation (2.7) expresses that the difference frequency of the two modes sharing the same cavity can be more stable than each mode. Thus, a dual-mode laser has advantage for generation of frequency-stable beat signals compared to a heterodyne technique employing two independent lasers.

2.1.4 Dynamics of Dual-Mode External Cavity Semiconductor Lasers

As shown in section 2.1.2, external cavity configurations provide an effective method to realize frequency-tunable SLs. As the SL in such configurations is subjected to optical feedback, the SL can exhibit a variety of dynamics induced by spectrally selective optical feedback and such dynamics have been extensively studied [50, 51, 52, 53, 54]. A dual-mode SL system based on spectrally filtered feedback from external double-cavity configurations can also exhibit various dynamics [32, 47, 55]. The dynamics of such a dual-mode SL system can be characterized into five regimes [47]: coherent, semicoherent, multimode, chaotic, and multimode chaotic operation. Coherent dual-mode lasing regime is the dual-mode operation in which each of the two main mode contains only a single external cavity mode. The total intensity shows a simple harmonic modulation at the difference frequency. For semicoherent dual-mode lasing regime, the optical spectrum is dominated by two selected main peaks. However, these peaks actually comprise several external cavity longitudinal modes. Therefore, the total intensity shows a harmonic modulation at the main difference frequency, accompanying a slow envelope modulation due to the presence of the external cavity modes. Multimode dual-mode lasing regime is the case for which each of the main peaks in the optical spectrum contains not only dense external cavity modes but also several longitudinal solitary laser modes. The total intensity reveals a slow envelope modulation due to the external cavity modes in addition to a fast envelope modulation due to solitary laser modes. In the case of chaotic and multimode chaotic dual-mode lasing regimes, the laser dynamics show a broadband and pulsing total intensities, which are characteristics of a chaotic state.

The best case for the generation of high-quality THz radiation is the coherent dual-mode lasing regime because the total intensity exhibits high contrast at the difference frequency. Therefore, motivated by these two reasons of frequency-stability and high-quality intensity modulation, this work pursues the stable beat signal generation of a SL in a coherent dual-mode lasing regime.

2.2 Realization of Frequency-Tunable Dual-Mode Semiconductor Lasers

The tunability of frequencies using spectrally filtered feedback in external cavity configurations provides clues for the realization of tunable dual-mode SLs. In particular, the concept of spectrally selective external cavities is attractive because of its simple setup,

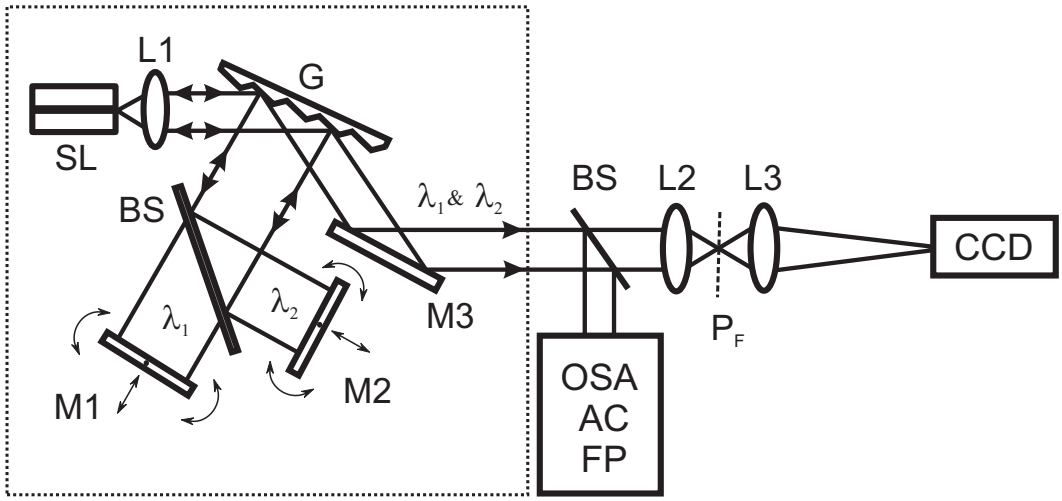

Fig. 2.3: Scheme for dual-mode semiconductor laser in the Double-Littman-Configuration; L1, L2 and L3: lenses, BS: beam splitter, M1, M2 M3: mirrors, G: grating, OSA: optical spectrum analyzer, AC: autocorrelator, FP: Fabry-Perot interferometer, CCD: CCD-camera.

wide frequency-tunability, and narrow linewidth of the selected modes. In this section, two different external cavity configurations will be studied, which enable tunable dual-mode emission of SLs. The emission characteristics of SLs in such configurations will be investigated.

2.2.1 Dual-Mode SL Using a Double-Littman-Configuration

One concept for the realization of tunable dual-mode SL is to build two external cavities using the Littman-configuration, i.e., a Double-Littman-configuration. The experimental setup for the Double-Littman-configuration is depicted in the dotted box in Fig. 2.3. The laser system consists of a SL, an aspheric collimation lens, a diffraction grating (G, 1200 grooves/mm), a 50/50 beam splitter (BS), and two high-reflective mirrors (M1 and M2 with a reflectivity of more than 98 %)). A commercial index-guided, multiple-quantum-well (MQW) SL (GaAlAs, Hitachi) with a stripe width of 5 μm and a length of 670 μm is used as a gain medium. The SL has a high-reflective rear facet and a low-reflective front facet. The threshold current of the solitary laser is $I_{th} = 41$ mA. The free running SL emits in a single longitudinal mode at a central wavelength of 784 nm and provides a maximum output power of 50 mW. The laser beam is TE-polarized (i.e., parallel to the active layer of the SL). The laser is thermally stabilized at room temperature with an accuracy of ± 0.01 K. The laser beam from the front facet is col-

limated by an antireflection-coated aspheric lens (L1) with a focal length of 3.1 mm (NA 0.68) and is directed onto a diffraction gating. The first-order diffraction beam of the grating is coupled into the external double-cavity with a total length of 17 cm. The beam is divided into two beams by a beam splitter, each of which is directed into each branch of the cavity. Within each branch of the cavity, the selection of the desired wavelength is performed by spectrally selected feedback of the laser beam via tilting the external mirror and simultaneously moving the mirror along the beam direction. Therefore, the laser system comprises two Littman-cavities sharing one grating and one gain medium. Since the output facet of the SL has a residual reflectivity, only the external modes which are resonant with the solitary laser modes will be effectively amplified. The zeroth-order grating beam is coupled out as output beam. In particular, for SLs which allow only one laser-facet to be coupled out, this configuration is appropriate. It provides a high mode-selectivity but at low feedback strength. In addition, this configuration provides a constant output beam direction, which is necessary for the photomixing technique to generate THz radiation.

The output beam is spectrally characterized by an optical spectrum analyzer (OSA, Anritsu) with a resolution of 0.05 nm (24 GHz at a wavelength of 785 nm). Due to the limited spectral resolution of the OSA, the external cavity modes with a mode spacing smaller than 24 GHz cannot be resolved by the OSA. Therefore, a scanning Fabry-Perot interferometer (FP, Melles Griot) with a free spectral range of 10 GHz and a resolution of 38 MHz is employed for fine spectrum resolution. In order to investigate the spatial intensity profile of the laser output facet, the zeroth-order beam is focussed by an aspheric lens (L2) with a focal length of 5 mm onto a virtual plane P_F. The image at P_F is projected onto the CCD-camera chip by an aspheric lens (L3) with a focal length of 6.2 mm. The CCD-camera provides time-averaged images. The image at P_F gives spatial intensity distribution and is the same image which is projected on the photoconductive material for photomixing.

Since electronic methods detecting signals with a central frequency of THz are not yet available, an intensity autocorrelation technique is used with a collinear autocorrelator (AC, APE) to verify simultaneous oscillation of the two laser modes [56]. An intensity autocorrelator is a type of Michelson-interferometer with a nonlinear optical medium such as a second-harmonic-generation (SHG) crystal and a detector such as a photomultiplier. The intensity for a collinear dual-mode beam having the same polarization of the partial beams can be expressed as

$$I(t) = I_1 + I_2 + 2\sqrt{I_1 I_2}\cos\omega t, \tag{2.8}$$

where I_1 and I_2 are intensities of the mode 1 and 2, respectively, ω is the angular

difference frequency of the two modes, and t is the time. The laser beam is divided by a beam splitter into two beams, one of which is variably delayed with respect to the other. Two beams are then spatially overlapped in the SHG crystal. The SHG signal is measured as a function of delay-time τ, which yields an autocorrelation trace whose intensity A is proportional to the intensity autocorrelation function

$$A(\tau) \propto \int I(t)I(t-\tau)dt = (I_1 + I_2)^2 + 2I_1 I_2 \cos \omega\tau. \tag{2.9}$$

The intensity autocorrelation trace will exhibit a cosinusoidal intensity modulation with a period corresponding to the difference frequency of the two modes, when the two modes oscillate simultaneously. In this chapter, intensity autocorrelation measurements will be discussed with respect to the simultaneous oscillation of two laser modes only. Measurements using intensity autocorrelation will be reviewed in detail in chapter 5 to determine the degree of intensity modulation of dual-mode beam.

In the following sections, the emission characteristics of the SL in a single Littman-cavity will be investigated in order to determine the performance of the SL with respect to frequency-tuning. the tunability of the SL. Subsequently, tunable dual-mode emission of the SL in the Double-Littman-configuration is characterized. Finally, another ECSL-configuration for tunable dual-mode emission will be presented as an alternative method.

2.2.1.1 Emission Characteristics of SL in a single Littman-Configuration

The basic concept for wavelength tuning of the laser is the spectrally filtered feedback of laser modes. In order to characterize the tunability of the laser, the SL is employed in a single Littman-configuration which consists of the grating G and one of the external mirrors (i.e., the other mirror is blocked) depicted in Fig. 2.3. The power of the zeroth-order beam is of 70 % of the total output power of the solitary laser and 30 % of the total output power is directed towards the external cavity. Therefore, 9 % of the total output power is reflected from the external cavity back toward the laser.

One effect of the feedback is the reduction of the threshold current of the laser. Figure 2.4(a) shows the threshold current versus tuned wavelength of the laser in the range of 778 and 784 nm. The threshold current decreases as the wavelength increases from 778 nm to 781.4 nm, at which the threshold current reaches a minimum. Above 781.4 nm, the threshold current increases with the wavelength. In the whole wavelength range, the threshold current of the SL with the feedback is lower than without

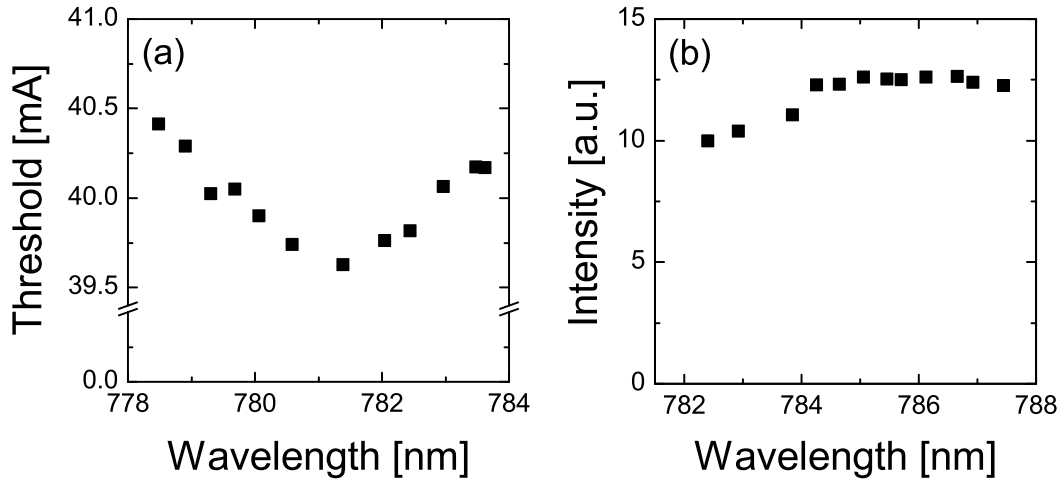

Fig. 2.4: Threshold current at various wavelengths (a) and output intensity at various wavelengths and at an injection current of $4.4I_{th}$ (b) of an ECSL. The laser is in the Littman-Metcalf configuration.

the feedback. The maximum threshold reduction amounts to 3 % of the solitary laser at 781.4 nm. The curve of the threshold current versus wavelength reflects the gain profile of the SL at an injection current near the threshold. That is, the laser has a gain maximum at 781.4 nm and the gain decreases as the wavelength is distant from 781.4 nm. Fig. 2.4(a) shows that the wavelength tuning range of the employed SL for an external mode is about 5.1 nm, which corresponds to a difference frequency of 2.5 THz. At further wavelength tuning, the solitary laser modes which lie near the gain maximum acquire enough gain and oscillate simultaneously in addition to the externally selected mode. This limitation of the tuning range is due to the residual reflectivity of the laser's front facet as well as the low feedback strength. An extension of the tuning range can be achieved by an antireflection-coating of the laser facet and higher feedback strength.

The wavelength tuning and the behavior of the output power of the laser at high injection currents are significant for high-power application of the tunable SL. Figure 2.4(b) shows the optical intensity versus tuned wavelength of the laser in the range of 782 and 788 nm. The laser is driven at an injection current of $4.4I_{th}$. At high injection currents, the operating wavelength of the laser shifts to longer wavelength region due to thermal heating of the active region of the laser. The intensity increases slightly with the tuned wavelength to 784 nm and is constant at longer wavelengths. The power difference in the investigated wavelength range is within 1.6 % of the maximum power. This behavior indicates that the gain becomes more flat at high injection currents and the laser exhibits constant performance almost independent of the tuned wavelengths.

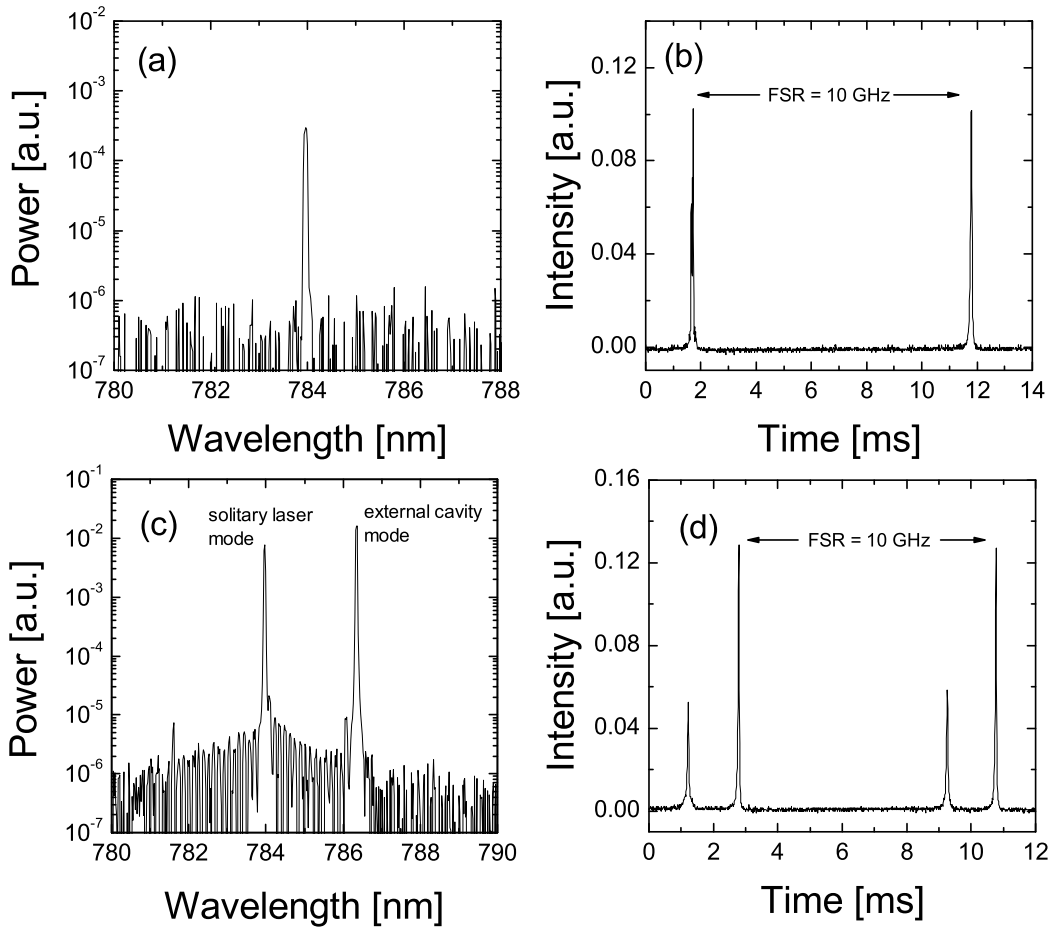

Fig. 2.5: Optical spectra of SL in the Littman-Metcalf-Configuration: (a) OSA-spectrum and (b) Fabry-Perot-spectrum of the free running SL; (c) OSA-spectrum and (D) Fabry-Perot-spectrum of the dual-mode emission.

The tuning range at the given injection current is limited to 5 nm due to the residual reflectivity of the laser's front facet. At further tuned wavelengths, the solitary laser modes begin to oscillate simultaneously.

An interesting phenomenon is that under these conditions the dual-mode emission of the SL can be achieved in a single Littman-configuration. When the position of an external mode in the gain spectrum and the feedback strength (for example, using a variable attenuator) from the external cavity are carefully adjusted, a single external mode at the selected gain position and a single solitary laser mode at the gain maximum oscillate simultaneously. An optical spectrum of the dual-mode emission of the SL in the single Littman-configuration is shown in Fig. 2.5. The SL is driven with an injection current of $4.1 I_{th}$ and the total output power amounts to 34 mW. For comparison, an

optical spectrum of the free running SL is displayed in Fig. 2.5(a). The free running SL emits a single-mode at 783,98 nm, which can be verified by a single peak in the Fabry-Perot spectrum (Fig. 2.5(b)) with a free spectral range (FSR) of 10 GHz. For dual-mode emission, the OSA-spectrum (Fig. 2.5(c)) shows two peaks at 783.98 and 786.34 nm and a weak peak at 781.62 nm. The Fabry-Perot spectrum shown in Fig. 2.5(d) confirms the purity of the dual-mode emission of the SL. The weak peak at 781.62 nm is a newly generated four-wave mixing (FWM) signal due to nonlinear interactions of the two intense optical fields with the SL medium. FWM phenomena will be discussed in detail in chapter 6. When the external cavity is blocked, the external mode and the FWM signal disappear and only the solitary laser mode oscillates at 783.98 nm. The sidemode suppression ratio between the dual-mode and other modes is more than 30 dB. The simultaneous oscillation of the two modes has been verified by observation of the intensity autocorrelation trace modulated with a period corresponding to the difference frequency. As mentioned above, when the external modes are selected distant from the gain maximum and the feedback strength is properly adjusted, the solitary laser mode at the gain maximum acquires enough gain due to the residual reflectivity of the laser's front facet and oscillates beside the external mode. That is, the cavity of the solitary laser, on the one hand, and the cavity composed of the external mirror and the laser's rear-facet, on the other hand, together constitute a double-resonator system. In this configuration, the dual-mode emission of the SL can be achieved in the difference frequency range between 800 GHz and 1.5 THz with a total output power of about 34 mW. At difference frequencies smaller than 800 GHz, the dual-mode emission cannot be achieved due to strong competition between the solitary laser mode and the external cavity mode. At difference frequencies larger than 1.5 THz, the external cavity mode reaches the edges of the gain spectrum and the solitary laser mode dominates. In addition, the tuning range of the difference frequency in this configuration is restricted to half the possible gain range. Since the solitary laser mode at the gain maximum cannot be arbitrarily selected, only half the gain spectrum can be used for wavelength selection. However, the realization of the tunable dual-mode emission of the SL in the external cavity configuration constitutes the basis of new configurations for tunable dual-mode SLs.

Another interesting phenomenon is that the single-mode SL exhibits in some cases multimode emission with optical feedback. Figure 2.6(a) and (b) show scanning Fabry-Perot traces for a single-mode and a multimode operation of the SL with the optical feedback, respectively. The mode spacing for the multimode emission is 880 MHz, which corresponds to the external cavity length of 17 cm. By fine tilting and moving the external mirror, the single-mode emission can be achieved. Besides spectral purity of the external cavity mode, the intensity stability of the multimode emission compared to the single-mode emission is a significant factor for applications needing stable laser

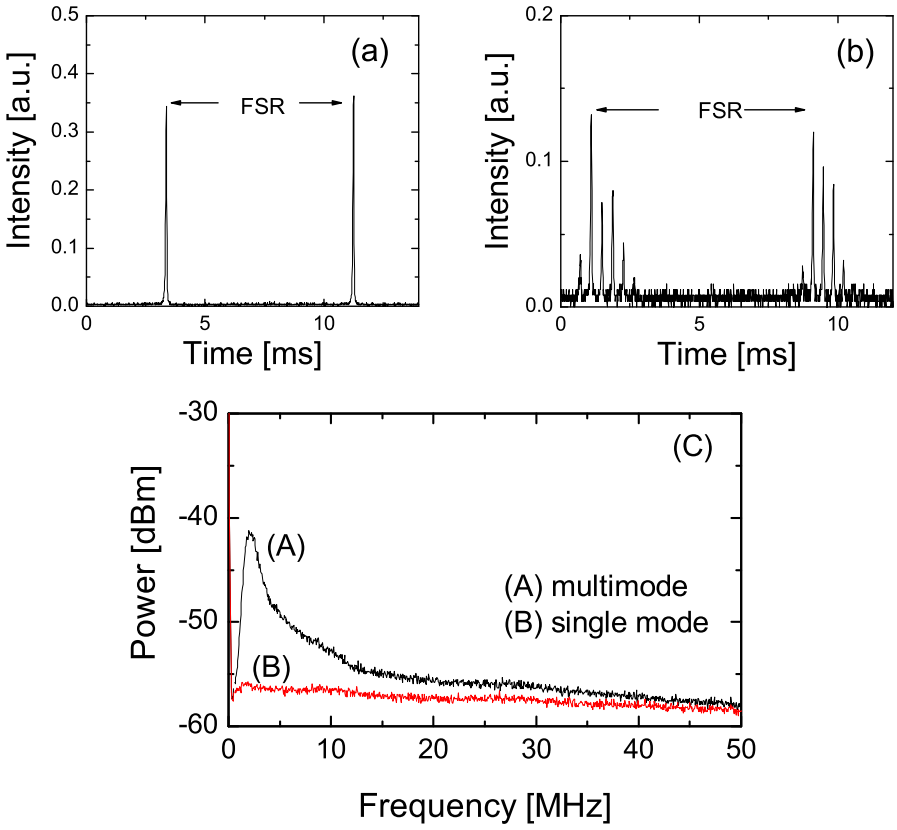

Fig. 2.6: Fabry-Perot spectra of single external mode (a) and multiple external mode emission (b) and corresponding intensity power spectrum (c) monitored by an electrical spectrum analyzer. FSR = 10 GHz.

output power.

In order to compare intensity fluctuations for multimode and single-mode emission with the optical feedback, the intensity noise of the laser light is analyzed. The laser light for multimode and single-mode emission is respectively detected by a photodiode with a cut-off frequency at 150 MHz. The AC component of the photocurrents is filtered with a bias-tee and is amplified with an amplifier. Then the signal is monitored with an electrical spectrum analyzer (HP6468). The intensity power spectrum of the multimode emission of the SL is shown in Fig. 2.6(c) as a function of frequency up to 50 MHz. For comparison, the intensity power spectrum of the single-mode emission is also displayed in Fig. 2.6(c). The power for the single-mode emission ((B) in Fig. 2.6(c)) exhibits a nearly constant behavior with frequency. In contrast, multimode emission ((A) in Fig. 2.6(c)) shows a larger power than the single-mode emission over the whole frequency range. Above 2 MHz the power decreases with increasing frequency. The

roll-off of the power below 2 MHz might be due to the low frequency roll-off of the detector. The power between 2 and 15 MHz is particularly strong and the difference of the power between the multimode and the single-mode emission at 2 MHz amounts to about 15 dB. The strong power at low frequencies may be due to mode competition between simultaneously oscillating external cavity modes. This result indicates that the dual-mode emission with external multimode oscillation in each of the two laser modes has large intensity fluctuations. Therefore, it is highly desirable to achieve dual-mode emission of the SL with a single-mode in each of the externally selected modes.

Based on the results obtained in this section, the realization of frequency-tunable dual-mode operation of the SL using the Double-Littman-configuration will be addressed in the following. In addition, each of the two modes will be controlled to achieve pure dual-mode emission.

2.2.1.2 Emission Characteristics of Dual-Mode Emission

The Double-Littman-configuration provides the desired wavelength-tunable dual-mode operation of the SL. Two optical spectra recorded by the OSA are depicted in Fig. 2.7. Figure 2.7(a) shows two external modes at wavelengths 785,2 and 785.86 nm with a difference wavelength of 0.66 nm, which corresponds to a difference frequency of 321 GHz. Two small peak at 784.54 and 786.52 nm in the spectrum are newly generated FWM signals. Figure 2.7(b) shows externally selected dual-mode emission at wavelengths 783.28 and 786.86 nm with a difference frequency of 3.58 nm, which corresponds to a difference frequency of 1.74 THz. In contrast to the case of the previous section, each mode can be individually tuned over the whole gain spectrum. By using variable attenuators in the external cavities or slight tilting of the external mirrors from the beam axis, the feedback strength can be controlled and the relative intensity of the two modes can be varied. Both modes are confirmed by a polarizer to be TE-polarized. By using the Double-Littman configuration, the difference frequency can be varied discontinuously between 100 GHz and 1.8 THz in multiples of 63 GHz, which is the mode spacing of the solitary SL. The achieved maximum output power amounts up to 35 mW. The sidemode suppression ratios of both laser modes excepting the FWM modes are better than 30 dB over the entire tuning range. As discussed in the previous section, the tuning range is limited due to the residual reflectivity of the laser's output facet. The achievable minimum difference frequency is limited by the mode spacing of the solitary SL. Although two external modes can be tuned further in the gain spectrum to achieve larger difference frequency, the solitary laser modes at the region of gain maximum acquire enough gain at larger difference frequencies and oscillate simultaneously with the two external modes. Therefore, the maximum difference frequency is limited by

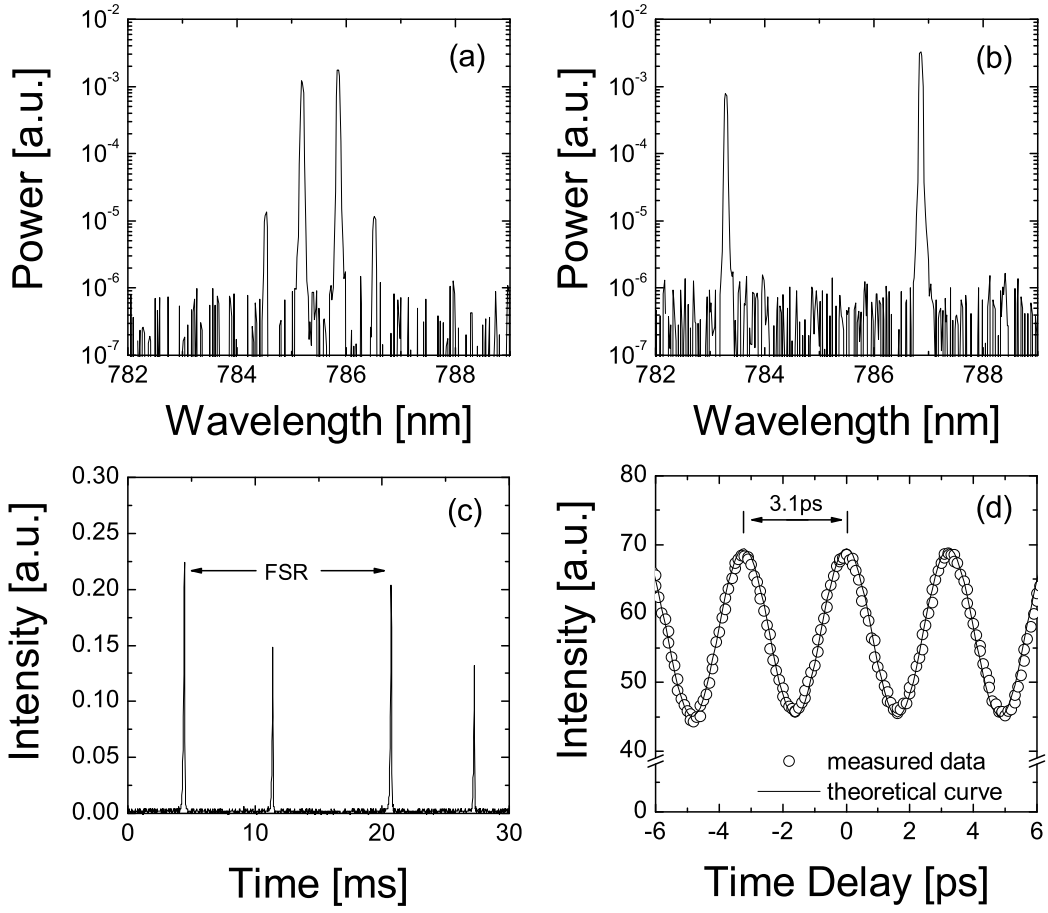

Fig. 2.7: Optical spectra for dual-mode operation with difference wavelengths of 0.66 nm (a) and 3.58 nm (b). Fabry-Perot spectrum (c) and intensity autocorrelation trace (d) for the dual-mode operation with difference wavelengths of 0.66 nm. FSR = 10 GHz.

the start of the oscillation of the solitary laser modes.

The spectral purity of the dual-mode emission has been confirmed by Fabry-Perot spectra. Figure 2.7(c) shows a Fabry-Perot spectrum for a dual-mode operation with a difference wavelength of 0.66 nm corresponding to Fig. 2.7(a). The spectrum exhibits pure dual-mode emission in a FSR of 10 GHz. The linewidth of each mode is also measured by using the Fabry-Perot interferometer and amounts to 60 MHz. This dual-mode emission containing only a single external cavity mode in each of the laser modes is the desirable case for application to high-quality THz wave-generation because the resultant THz wave is highly coherent at the selected difference frequency. In contrast, although only two peaks with a tuned difference frequency are recorded in the OSA, the Fabry-Perot spectrum shows in some cases multimode emission with a mode spacing of

the external cavity for each peak so that the spectrum consists of two external mode-groups. Nevertheless, the transition of multimode emission to single-mode emission can be achieved by fine adjustment of the external feedback. The multimode emission might influence the coherence of the generated THz wave at the selected difference frequency. The coherence of the generated THz wave depending on the single-mode and multimode emission will be discussed in chapter 3.

The intensity modulation of the laser beam with a difference frequency is achieved when the two modes oscillate simultaneously. The simultaneous oscillation of the two external modes can be monitored by an intensity autocorrelation measurement. Figure 2.7(d) shows a measured intensity autocorrelation trace for the dual-mode emission with a difference frequency of 321 GHz shown in Fig. 2.7(a). The value of the background of the autocorrelation trace in 2.7(d)lies near 30. The autocorrelation-intensity is displayed as a function of the time-delay. The open circles represent experimental data and the solid line is a theoretical curve modulated by $\cos\omega\tau$, where ω and τ represent angular modulation frequency and the time-delay, respectively. The experimental data exhibit a cosinusoidal waveform with a period of 3.1 ps and coincide with the theoretical curve representing a cosinusoidal modulation with a difference frequency of $f(= 2\pi/\omega)$ = 321 GHz. The contrast of the modulation remains almost the same over the whole time-delay of 125 ps, which is the time-delay limit of the employed autocorrelator. This indicates a phase coherence of the dual-mode beam and a linewidth smaller than 8 GHz of the modulated signal. The simultaneous oscillation of two laser modes is confirmed at all difference frequencies by the intensity autocorrelation measurements. Therefore, the results indicate that frequency-tunable dual-mode emission in the SL is realized by using the Double-Littman-external-cavity-configuration. The realized dual-mode external cavity SL (2λ-ECSL) will be used in the next chapter for the generation of THz radiation.

2.2.2 Spatial Intensity Distribution of Dual-Mode Emission

One of the significant parameters relevant to mixing efficiency of the two laser modes is the spatial intensity distributions of the laser beam for dual-mode emission in the focal point P_F shown in Fig 2.3. For the application to photomixing, the laser beam is focussed on a small area of micrometer-size. Since even SL with a stripe width of 5 μm can exhibit laterally higher-order modes [57], the beam quality might not be no longer as good as for pure fundamental mode emission. In particular, structured intensity profile due to laterally higher-order operation reduces the focusable optical power. Furthermore, the mixing efficiency of the two laser modes can be reduced if each mode oscillates in lateral modes of different orders. In addition to Fabry-

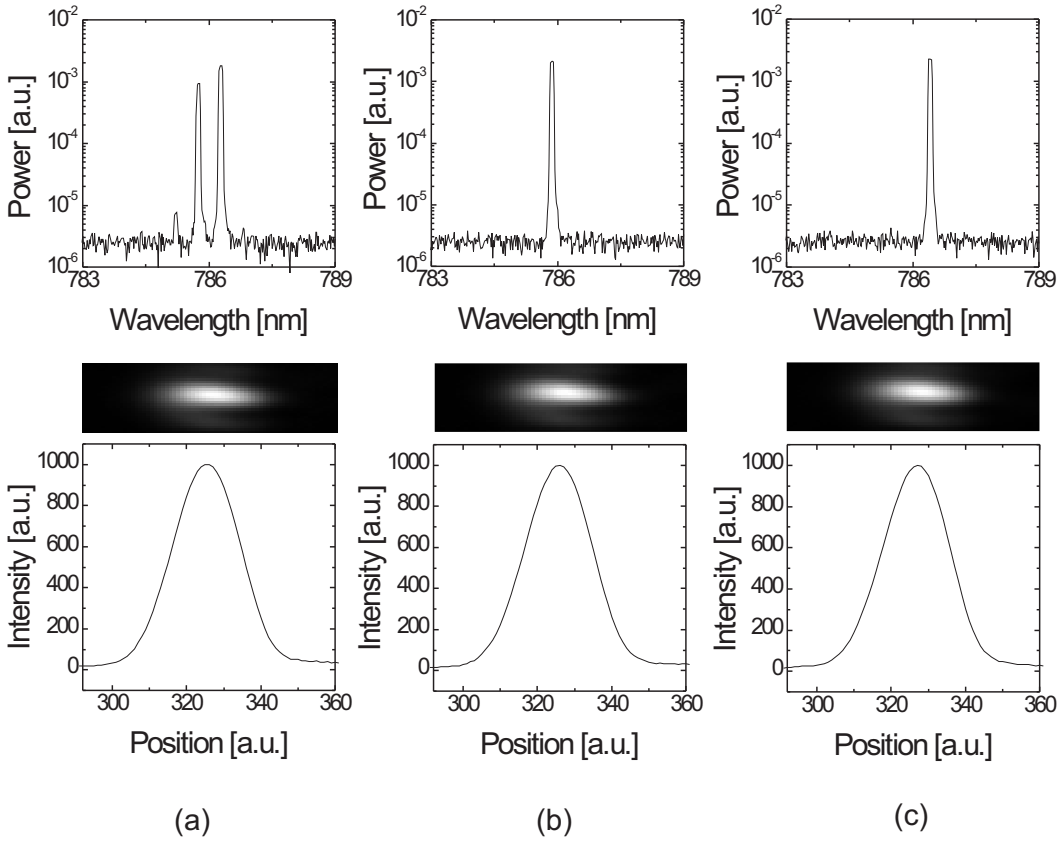

Fig. 2.8: Optical spectra and its corresponding beam intensity profiles at the focal point P_F acquired with a CCD-camera (a) for dual-mode emission with a double-feedback at M1 and M2, (b) and (c) for single-mode emission with a single feedback at M1 and M2, respectively.

Perot spectrum exhibiting spectral characteristics, the time averaged (i.e., temporally integrated) spatial intensity distribution at P_F provides the spatial characteristics of the dual-mode beam. The intensity profile at P_F can be monitored by a CCD-camera. This temporally integrated image of the spatial intensity distribution at P_F represents intensity profile of the laser output facet.

Figure 2.8 shows OSA-spectra (top diagrams) for dual-mode and single-mode emission with optical feedback, the beam images (middle diagrams) acquired with the CCD-camera and the corresponding intensity profile in lateral direction of the SL, respectively. The laser is driven at $I_{inj} = 4.4I_{th}$. The difference wavelength is 0.52 nm which corresponds to a difference frequency of 252 GHz. The OSA-spectrum in Fig. 2.8(a) shows two external modes near 786 nm and two FWM signals near 785 and 787 nm. The purity of the single-mode emission of each mode has been confirmed by the Fabry-

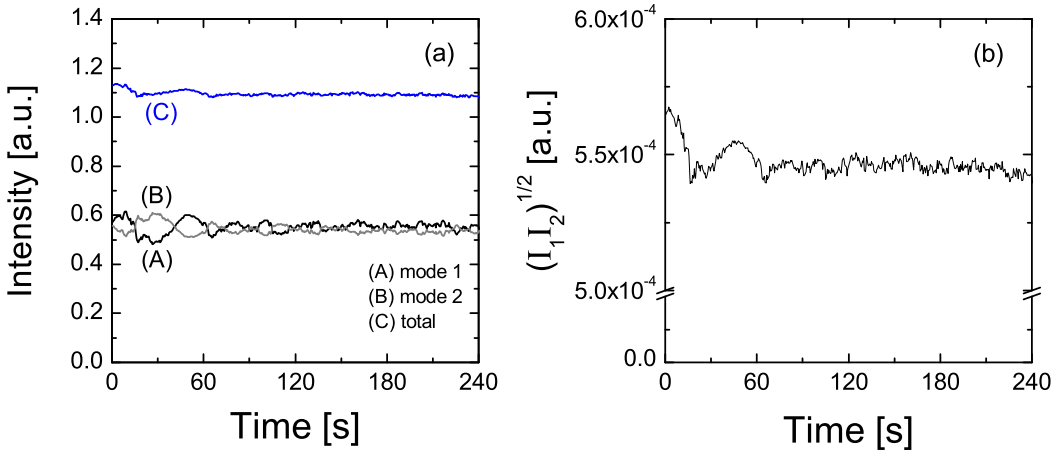

Fig. 2.9: Time evolution of dual-mode emission (a) and intensity product-term of the two modes (b) : intensity of mode 1 (A), mode 2 (B), and total intensity (C).

Perot interferometer exhibiting only two modes within the FSR for dual-mode emission. The CCD-image and the corresponding intensity profile exhibit Gaussian distribution with a spatial ratio of 1:4 in transverse and lateral directions. Figures 2.8(b) and (c) show measurements obtained for individual single external mode near 786 nm, respectively, also exhibit the same Gaussian intensity distribution. The Fabry-Perot spectrum has exhibited single-mode emission in each case. The Gaussian intensity profile and the Fabry-Perot spectrum exhibiting single-mode emission of each mode, therefore, indicate that the laser emits fundamental lateral mode for dual-mode and single-mode emission. Hence, the intensity profile of the laser has high beam quality.

2.2.3 Temporal Behavior of Dual-Mode Emission

For stable beat signals and stable THz radiation, it is significant to achieve temporally stable dual-mode emission of the laser. In order to investigate the time-evolution of the dual-mode emission, the temporal behavior of the two modes is analyzed by detecting each intensity of the two spectrally resolved modes. The laser is driven at a constant injection current of $4.5I_{th}$. The output beam of the 2λ-ECSL is incident on a grating (1800 grooves/mm). The dual-mode beam is then spectrally separated into two beams by the grating and each beam contains only one frequency. The two beams are detected simultaneously by two detectors (photodiodes, UDT10D), respectively.

Temporal emission properties of the two laser modes with a difference frequency of 515 GHz and in a time interval of 240 s since the start of the dual-mode operation are displayed in Fig. 2.9. (A) and (B) in Fig. 2.9(a) show the temporal intensity-behaviors

of the mode 1 and 2, respectively. (C) in Fig. 2.9(a) shows the temporal behavior of the total intensity of the two modes. The curves (A) and (B) show slight fluctuations in 60 s with a deviation within 7 % of each average intensity. After 60 s, each mode stabilizes with a deviation within 3 % of the average intensity. Total intensity (curve (C)) of the dual-mode emission shows a constant temporal behavior in the whole time interval with a deviation within 1.5 % of the average total intensity. As can be shown by curves (A) and (B), fluctuations in the intensity of one mode accompanies anticorrelated fluctuations in the intensity of the other mode. Because the two laser modes share the same gain, an increase (decrease) of the power of one mode is accompanied by a decrease (increase) of the power of the other mode. Due to the anticorrelation of the two modes, the total intensity is more stable than the intensity of each mode. This is shown in Fig. 2.9 as a more stable temporal behavior of the total intensity than of each mode.

In particular, in the expression $I_1 + I_2 + 2\sqrt{I_1 I_2}\cos\omega t$ describing the intensity modulation of the dual-mode emission, the stability of the intensity product-term $\sqrt{I_1 I_2}$ is relevant to the stability of THz radiation. The AC component of the total intensity is responsible for the AC component of antenna-photocurrent which generates THz radiation. This AC component is represented by the product-term of both intensities. The temporal behavior of the intensity product-term of the two modes is displayed in Fig. 2.9(b), which is numerically calculated from Fig. 2.9(a). The intensity product-term shows small fluctuations with a deviation of about 2 % of the averaged intensity-product in 60 s and stabilizes after 60 s to a constant value with a deviation of about 1 % of the averaged intensity-product. This result indicates that the AC component of the antenna-current generated by photomixing of the two laser modes exhibits a constant behavior with the same deviation as the deviation of the intensity-product. Due to a quadratic relation between the antenna-photocurrent and the THz generation, which will be discussed in the next chapter, fluctuations of the generated THz radiation then are expected to lie within 4 % in 60 s and 2 % after 60 s of the average power. The temporal behavior of the generated THz radiation will be discussed in the next chapter.

2.2.4 Dual-Mode SL Using a Double-Littrow-Configuration

After successful demonstration of tunable dual-mode operation of SL using the Double-Littman-configuration in the previous sections, an alternative concept for the realization of tunable dual-mode SL will be investigated in this section. This concept is to build two external cavities using the Littrow-configuration, i.e., Double-Littrow-configuration. The experimental setup for the tunable dual-mode SL using the Double-

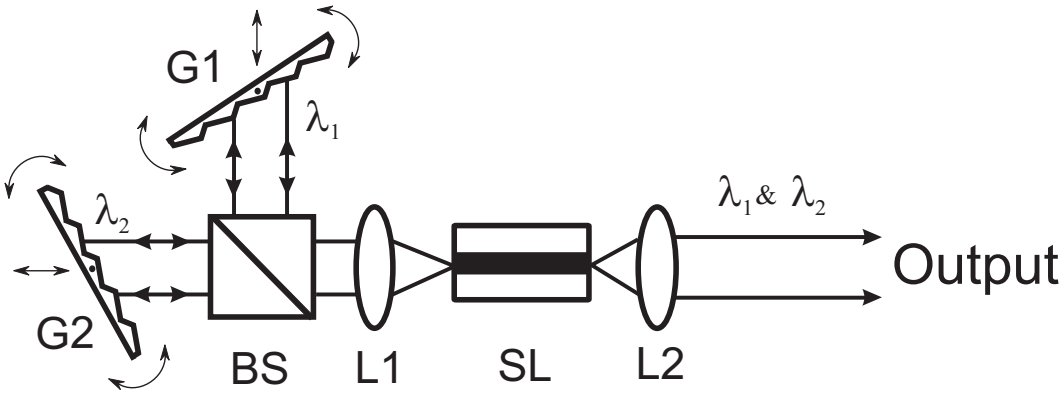

Fig. 2.10: Schematic for a dual-mode semiconductor laser in the Double-Littrow-Configuration: diffraction gratings (G1 and G2), aspheric lenses (L1 and L2), beam splitter (BS).

Littrow-configuration is depicted in Fig. 2.10. The laser system consists of a SL, two aspheric lenses (L1 and L2), a 50/50 beam splitter (BS), and two diffraction gratings (G1 and G2 with 1200 grooves/mm) with a reflectivity of 65 % in the first order diffraction beam. A ridge waveguide SL (FBH, Ferdinand-Braun-Institut für Höchstfrequenztechnik) with a stripe-width of 3 μm and a length of 1.2 mm is used as a gain medium. The SL has a threshold current of $I_{th} = 50$ mA and emits TE-polarized light at a central wavelength of about 828 nm with a longitudinally multimode and a laterally fundamental mode. The maximum output power amounts to about 120 mW. The rear facet of the laser is antireflection (AR)-coated with a reflectivity of 0.5 % and the uncoated front facet has a reflectivity of 30 %. The laser beam from the AR-coated rear facet is collimated by an aspheric lens (L1) with a focal length of 3.1 mm (NA 0.68) and is coupled into the external double-cavity with a length of 20 mm. The collimated beam is divided into two beams by a 50/50 beam splitter. Within each branch, the beam is incident on a grating and the first order diffraction beam of the grating is reflected back into the laser. The selection of the desired wavelength in each resonator is achieved by tilting the external grating and simultaneously moving the grating along the beam direction by a piezo-electric transducer (PZT). Therefore, the laser system consists of two Littrow-cavities. The output coupling of the SL for applications is achieved by collimating the beam from the front facet by an aspheric lens (L2) with a focal length of 3.1 mm (NA 0.68).

Although the mode-selectivity of the grating in the Littrow-cavity is lower than in the Littman-cavity due to a smaller number of illuminated grooves, this Double-Littrow-configuration provides several advantages compared to the Double-Littman-configuration shown in Fig. 2.3. The beam from the AR-coated facet is only coupled to

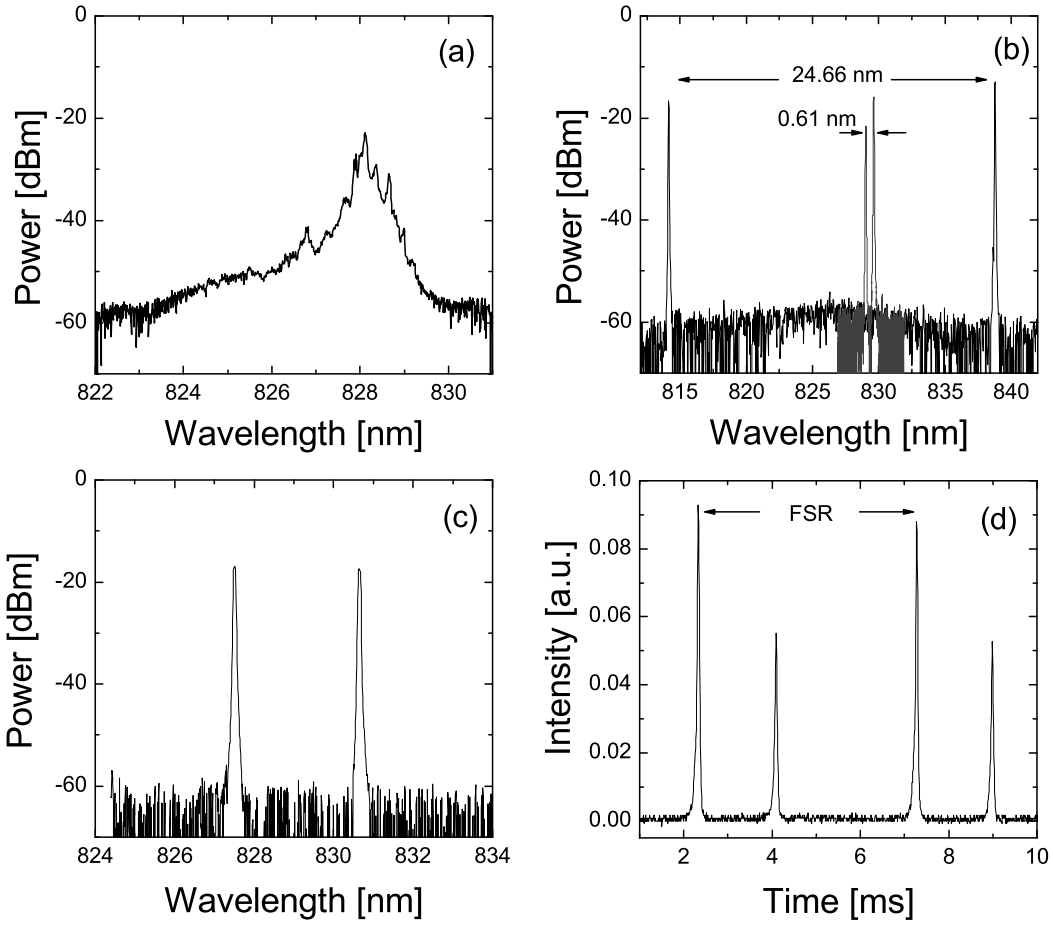

Fig. 2.11: Optical spectra of free running and dual-mode emissions of SL: (a) OSA-spectrum of free running SL; (B) OSA-spectra of dual-mode emission with difference wavelengths (frequencies) of 0.61 nm (266 GHz) and 24.66 nm (10.8 THz); (c) OSA-spectrum of dual-mode emission with difference wavelengths of 3.14 nm (1.37 THz); (d) Fabry-Perot spectrum monitored simultaneously for (c). The laser is driven at $3.4I_{th}$. The output power amounts to 55 mW. FSR = 10 GHz

external resonators for the wavelength selection. Therefore, using high reflectivity gratings improves resonator quality so that the output power and the sidemode suppression can be improved and the linewidth can be in effect narrowed. The high sidemode suppression also results in a wider tuning range. Furthermore, the beam collimation for the external resonators can be performed independent of the collimation of the output beam. Hence, optimum collimation for the wavelength selection and the output coupling can be achieved individually. Moreover, the resonator-length in this configuration can be made shorter than in the Double-Littman-configuration. Therefore, the laser system can be made compacter. Furthermore, wider external mode-spacing can

be achieved, which enables better external mode-selection in each resonator.

Figure 2.11 shows OSA-spectra of the free running and dual-mode emissions of the SL. The laser is driven at an injection current of $I_{inj} = 3.4I_{th}$ and operates at room temperature. The spectrum of the free running SL (Fig. 2.11(a)) exhibits a multitude of longitudinal modes (not fully resolved) with a maximum peak near a wavelength of 828 nm and within a spectral range of more than 2 nm. By spectrally filtered feedback in each resonator, frequency-tunable dual-mode emission is achieved. Figure 2.11(b) shows two spectra for the dual-mode emission of the SL with difference wavelengths of 0.61 and 24.66 nm, respectively. They correspond to difference frequencies of 266 GHz and 10.8 THz, respectively. By tilting the external gratings, each mode can be tuned independently over the whole gain spectrum. The difference frequency of the two modes can be tuned in the range between 100 GHz and 10 THz with tuning steps smaller than 23 GHz (i.e., 0.05 nm), possibly discontinuous below the resolution limit implied by the OSA. The single-mode operation of each external mode is achieved by the PZT and confirmed by monitoring the spectrum using the Fabry-Perot interferometer with a FSR = 10 GHz. Figure 2.11(c) and (d) show an OSA-spectrum and its corresponding Fabry-Perot spectrum monitored for dual-mode emission with a difference wavelength (frequency) of 3.14 nm (1.37 THz), respectively. The Fabry-Perot spectrum exhibits only two external modes in the FSR. The linewidth of each external mode measured by the Fabry-Perot interferometer amounts to about 120 MHz. The simultaneous oscillation of two external modes is confirmed by the intensity autocorrelation measurement which shows harmonic intensity modulation with a period corresponding to the difference frequency. The output power of 60 mW is achieved at $I_{inj} = 3.6I_{th}$. The sidemode suppression amounts to more than 40 dB. FWM signals are also observed for the dual-mode emission of the SL. Although external modes can be selected at difference frequencies larger than 10 THz, the solitary laser modes lying in the region of the gain maximum acquire enough gain due to residual reflectivity of the rear facet such that solitary laser modes oscillate simultaneously with the two external modes. The tunable difference frequency range from 100 GHz to 10 THz achieved in this work is, however, covering the desired frequency range for THz technology.

2.3 Summary

In this chapter, two concepts for tunable dual-mode emission of SL have been presented. They are based on the spectrally selected feedback in the external double-cavity configuration.

One concept is the Double-Littman-configuration. This is a modified Littman-con-

figuration comprising two Littman-cavities, in which the desired wavelengths can be selected by filtered feedback of the spectrally resolved beam via tilting two external mirrors. By using an index-guided SL as a gain medium, the tunable dual-mode operation is achieved with a maximum output power of 35 mW. The simultaneous oscillation of the two modes is confirmed by an intensity autocorrelation technique. Each mode can be tuned in the whole gain spectrum and contains a single external cavity mode with a linewidth of 60 MHz. The difference frequency can be varied from 100 GHz to 1.8 THz with an almost constant output power-performance. Even though two modes are anti-correlated with each other, because they share the same gain of the laser, they are temporally stable. The spatial intensity distribution of the SL for dual-mode emission exhibits a Gaussian form, which reveals high beam quality.

Another promising concept for tunable dual-mode SL is the Double-Littrow-configuration, which consists of two Littrow-cavities. The wavelength tuning is achieved by tilting two gratings which perform not only spectral resolution but also feedback of the desired wavelengths. Using a ridge waveguide SL with a maximum output of 120 mW as a gain medium, tunable dual-mode operation is realized with a tuning range from 100 GHz to 10 THz. An output power of up to 60 mW is achieved for the dual-mode emission and each mode contains a single external mode with a linewidth of 120 MHz.

The realized stable, frequency-tunable dual-mode emission of SLs provides the basis for generation of stable, frequency-tunable THz radiation. Generation of THz radiation employing the two concepts for dual-mode SL shown in this chapter will be discussed in the next chapter. Moreover, for dual-mode emission in both external cavity configurations, four-wave mixing phenomena are observed, which originate from nonlinear interactions of the optical fields with the SL-medium. This phenomenon will be discussed in chapter 6.

Chapter 3

Generation of Tunable CW THz Radiation via Photomixing

THz technology has attracted growing attention due to its potential applications of THz radiation to spectroscopic identification of chemical elements and nondestructive imaging of materials which are opaque to visible and infrared light. Recently, several techniques for the generation and detection of THz radiation have been developed and tested for spectroscopic and imaging applications. For such applications, in particular, the frequency stability of the THz radiation is an important factor. Furthermore, it is desirable for commercial applications that THz sources should be compact and cost-effective. One method to realize such sources is photomixing.

In this chapter, successful realization of a compact, cost-effective, frequency-tunable CW THz radiation source and generation of frequency-tunable CW THz radiation is presented. The THz radiation is generated via photomixing of two laser modes on photoconductive antennas. As optical laser sources, frequency-tunable 2λ-ECSLs are employed which were discussed in chapter 2. Wide tunability of the THz radiation frequency is achieved by tuning the difference frequency of the two laser modes.

The first part of this chapter gives an overview of photomixing mechanisms and photoconductive antennas. Subsequently, experimental methods for generation and characterization of THz radiation are presented. Finally, the generated THz radiation is characterized.

3.1 Principle of Generation of CW THz Radiation via Photomixing

A method to generate CW THz radiation is optical heterodyne conversion, or photomixing, of two CW laser beams using a photoconductive THz-emitter system [22]. A photoconductive material with a short carrier lifetime ($< 1\,\mathrm{ps}$) is illuminated with

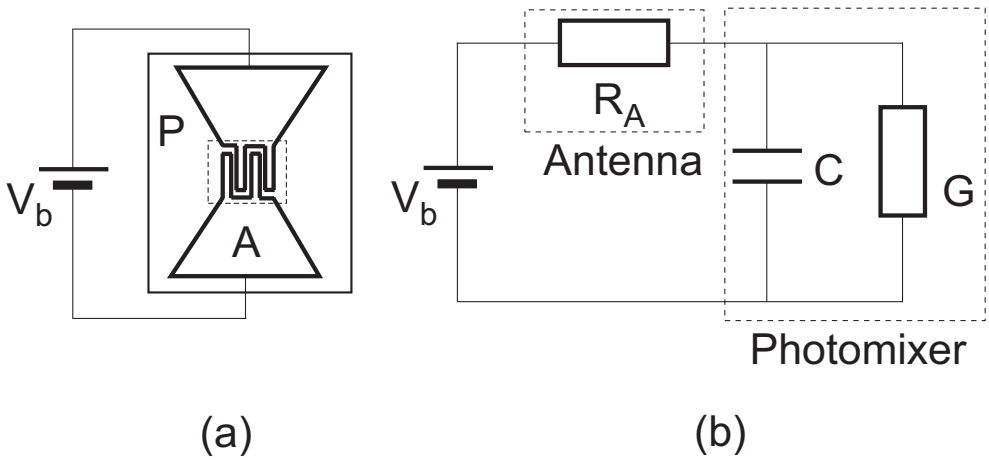

Fig. 3.1: Schematic diagrams of a THz-emitter (a) and its equivalent circuit model (b). The photomixer comprises the photoconductor and electrodes shown in the dotted box in (a). P: photoconductor, A: antenna, C: capacitance of the photomixer, G: conductance of the photomixer, V_b: bias voltage, R_A: radiation resistance of the antenna.

two CW laser beams whose photon energy is higher than the band gap of the material. The heterodyne mixing of two beams modulates the conductance of the material with the difference frequency of the two beams. When a bias is applied to the THz-emitter and the difference frequency lies in the THz range, the photocurrent is modulated at the THz frequency. The CW THz wave is then radiated from the THz-emitter into free space.

The THz-emitter consists of a photoconductor, electrodes, and an antenna. The schematic diagram of the THz-emitter is displayed in Fig. 3.1(a). The photoconductor plays the role of a switch whose conductance can be modulated through the creation of photocarriers in response to the light. The photocarriers in the photoconductor are coupled to the antenna and the external circuit through the electrodes. The electrodes define the geometry of the photoconductive gap and their design is significant for the efficiency of the photomixing. The photoconductive gap and electrodes constitute a photomixer (displayed in the dotted box in Fig. 3.1(a)), which converts the optical modulation to the electrical modulation. The antenna couples the electrical signal to the free space electromagnetic signal. The electrodes and the antenna are connected to the external circuit, through which a bias (V_b) can be applied to the photoconductive gap. The equivalent circuit model of the THz-emitter is displayed in Fig. 3.1(b) [22, 58, 59]. The current in the biased circuit is modulated at the difference angular frequency ω by the photoconductance $G(t)$ which is a function of the absorbed optical power. A capacitance C of the photoconductive gap is connected parallel to G. C

represents charge accumulation at the electrodes and depends on the electrode geometry and the dielectric constant of the photoconductive material. G and C together describe the photomixer (the right dotted box in Fig. 3.1(b)). In a radiation resistance R_A representing the antenna (the left dotted box in Fig. 3.1(b)), the electrical power is dissipated and its component oscillating with ω is radiated as the THz wave.

3.1.1 Photomixing

When two laser beams with average powers P_1 and P_2, angular frequencies $\omega_1 = 2\pi f_1$ and $\omega_2 = 2\pi f_2$, and aligned linear polarization illuminate the photomixer, the instantaneous optical power incident on the photomixer is given by

$$P(t) = P_1 + P_2 + 2\sqrt{mP_1P_2}\cos\omega t, \tag{3.1}$$

where $\omega = \omega_1 - \omega_2$ is the angular frequency difference, and m is the mixing efficiency of the beams. m is a measure of the spatial overlap of the incoming beams, and has values between 0 (no overlap) and 1 (perfect overlap) [22, 60]. Here, the terms that vary at optical frequencies ω_1, ω_2, and $\omega_1 + \omega_2$ are ignored because the photoconductor cannot respond to such rapid variation with the time scale much shorter than the photocarrier lifetime of the photoconductor.

The time-dependent photoconductance $G(t)$ is given by [22]

$$G(t) = G_0\left(1 + \frac{2\sqrt{mP_1P_2}\sin(\omega t + \phi)}{P_0\sqrt{1+\omega^2\tau^2}}\right), \tag{3.2}$$

where $G_0 = e(\mu_e+\mu_h)\eta_e P_0\tau F_p/h\nu$ is the DC conductance for the averaged total incident power $P_0 = P_1 + P_2$, τ is the photocarrier lifetime, and $\phi = \tan^{-1}(1/\omega\tau)$ is the phase shift depending on the carrier lifetime. In the expression for G_0, e is the electron charge, μ_e and μ_h are the electron and hole mobilities, respectively, η_e is the external quantum efficiency (number of photocarrier pairs generated per incident photon), $h\nu$ is the mean photon energy of the laser beam, and F_p is a factor depending on the geometry of the photomixer.

The time-dependent conductance modulates the bias current at frequency ω, and the power delivered to R_A is radiated into free space as the electromagnetic wave at the same frequency. Solving the dynamic current equation for the circuit in Fig. 3.1(b), the THz radiation output power $P_{\mathrm{THz}}(\omega)$ is given in the small-signal limit, where $G_0R_A \ll 1$, by [22]

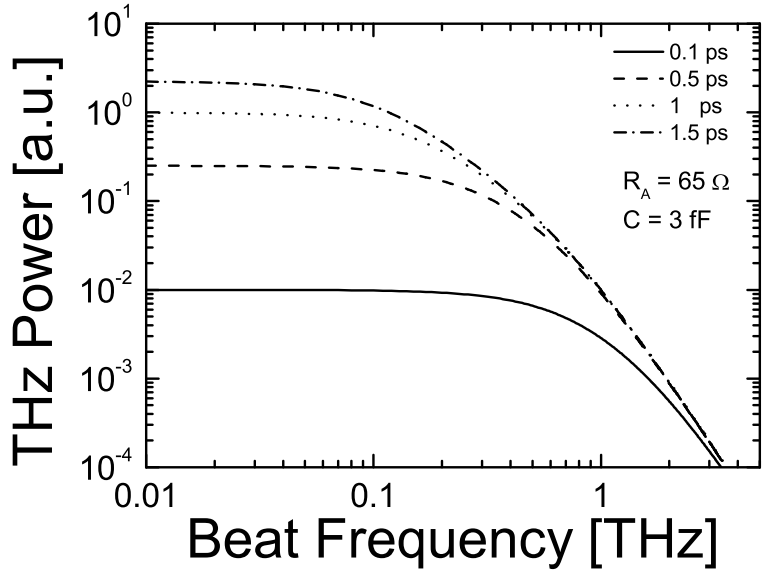

Fig. 3.2: Diagram for the theoretical THz output power according to Eq. (3.4) as a function of beat frequency for carrier lifetimes of 0.1, 0.5, 1, and 1.5 ps of the photoconductor. $R_A = 65\,\Omega$ and $C = 3\,\mathrm{fF}$ have been assumed.

$$P_{\mathrm{THz}}(\omega) = 2(V_b G_0)^2 R_A \frac{m P_1 P_2}{P_0^2[1+(\omega\tau)^2][1+(\omega R_A C)^2]}. \tag{3.3}$$

The value of P_{THz} is maximized when $m = 1$ and $P_1 = P_2 = P_0/2$ for other fixed parameters. Eq. (3.3) can then be written as

$$P_{\mathrm{THz}}(\omega) = \frac{I_0^2 R_A}{2[1+(\omega\tau)^2][1+(\omega R_A C)^2]}, \tag{3.4}$$

where $I_0 = V_b G_0$ is the DC photocurrent. Equation (3.4) expresses that the THz radiation output power $P_{\mathrm{THz}}(\omega)$ is proportional to the square of the DC photocurrent I_0, and consequently to the square of the bias voltage V_b, and shows a linear dependence on the radiation resistance R_A of the antenna. Since G_0 is proportional to the total optical power P_0, $P_{\mathrm{THz}}(\omega)$ is proportional to the square of P_0. For frequency-independent antennas such as self-complementary antennas [61], R_A is independent of the frequency. Then, the spectral bandwidth of the THz radiation is limited by the carrier lifetime τ and the $R_A C$ time constant. In the limit of high frequency, where $\omega\tau \gg 1$ and $\omega R_A C \gg 1$, $P_{\mathrm{THz}}(\omega) = I_0^2 R_A / 2\omega^4 (\tau R_A C)^2$, thus, $P_{\mathrm{THz}}(\omega) \sim \omega^{-4}$. Therefore, the decrease in THz output power at $-12\,\mathrm{dB/octave}$ is expected in the high frequency limit.

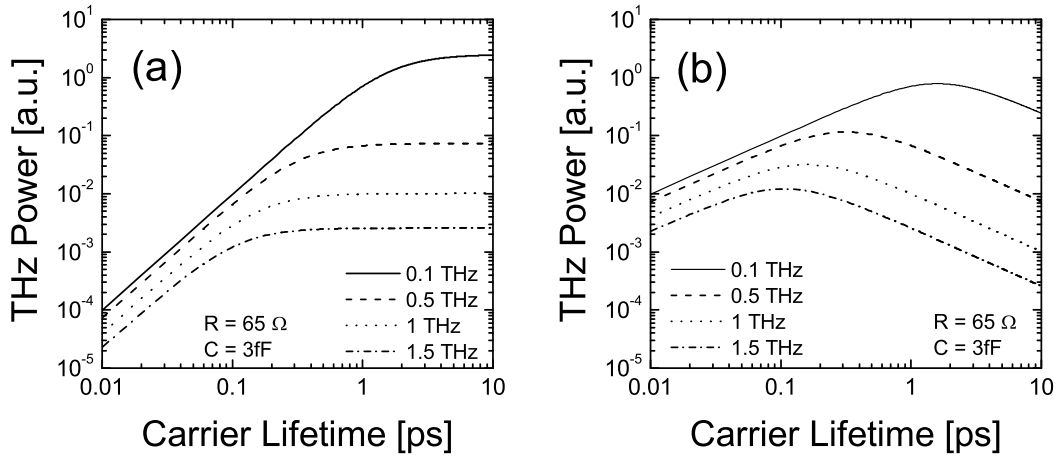

Fig. 3.3: Diagrams for the theoretical THz output power (a) according to Eq. (3.5), and (b) at a given P_{Joule} limit (Eq. (3.6)) as a function of carrier lifetime for beat frequencies of 0.1, 0.5, 1, and 1.5 THz, respectively. $R_A = 65\,\Omega$ and $C = 3\,\text{fF}$ are substituted in both equations.

Since G_0 is proportional to photocarrier lifetime τ, equation (3.4) can be expressed, assuming the other quantities fixed, as

$$P_{\text{THz}}(\omega) \sim \frac{\tau^2}{[1+(\omega\tau)^2][1+(\omega R_A C)^2]}. \tag{3.5}$$

The theoretical behavior of $P_{\text{THz}}(\omega)$ according to Eq. (3.5) is plotted in Fig. 3.2 as a function of the beat frequency of the two laser beams for several photocarrier lifetimes of the photoconductor. Here, $65\,\Omega$ and $3\,\text{fF}$ are inserted for R_A and C, respectively, which are values of the same order of magnitude for typical photomixers and antennas. The frequency behavior of $P_{\text{THz}}(\omega)$ is flat at low frequencies, and shows the roll-off of $-12\,\text{dB/octave}$ at high frequencies depending on the carrier lifetime. $P_{\text{THz}}(\omega)$ shows higher power for the longer carrier lifetime than for the shorter lifetime. The theoretical carrier lifetime dependence of the THz output power is displayed in Fig. 3.3(a) for several beat frequencies. $P_{\text{THz}}(\omega)$ increases with increasing τ and becomes flat for large τ. At any given τ, $P_{\text{THz}}(\omega)$ for lower frequencies is higher than for higher frequencies. For high frequencies, where $\omega\tau \gg 1$, $P_{\text{THz}}(\omega)$ becomes independent of τ.

The power delivered from the applied bias to the photoconductive resistance is dissipated as Joule heat (DC power) which is given by $P_{\text{Joule}} = G_0 V_b^2$. This heat causes in practice thermal damage of the photomixer. Thus, the available DC photocurrent for the photomixer is limited by the DC power limit. Eq. (3.4) can be rewritten as [59]

$$P_{\mathrm{THz}}(\omega) \sim \frac{P_{\mathrm{Joule}}\tau}{[1+(\omega\tau)^2][1+(\omega R_A C)^2]}, \tag{3.6}$$

which describes the maximum available THz output power at any given frequency and any given DC power limit for the photomixer. The theoretical P_{THz} behavior at any given P_{Joule} limit is displayed in Fig. 3.3(b) as a function of carrier lifetime for several beat frequencies. The available $P_{\mathrm{THz}}(\omega)$ at any given frequency and any given DC power limit has a maximum at a particular carrier lifetime τ_{op}. This optimum carrier lifetime τ_{op} can be obtained by differentiating Eq. (3.6) with respect to τ [59], which yields the condition for τ_{op}

$$\omega\tau_{op} = 1. \tag{3.7}$$

For too short carrier lifetimes, the photoconductance cannot be modulated enough to give a high AC current amplitude. For too long carrier lifetime, heating in the photomixer increases due to the charge accumulation. To avoid thermal damage of the device, the bias must be decreased, which in turn reduces the AC current. Thus, both cases reduce the available THz output power.

As shown in this section, the performance of the photomixing depends on several factors such as carrier lifetime, capacitance of the photomixer, radiation resistance of the antenna, and incident optical power. For effective generation of the THz radiation, such factors must be optimized.

3.1.2 Optical Power Dependence of THz Generation

As shown in the previous section, the THz power which is induced by the AC component of the photocurrent via photomixing is proportional to the power product of individual modes and is maximized when both modes have the same power at a given total optical power. That is, maximum THz power is generated when the photocurrent is perfectly modulated by complete modulation of the incident light intensity. This is an ideal case for generation of THz radiation with maximum THz power. In practice, one mode has more or less power than the other. In this case, the generated THz power is lower than that of the ideal case due to the decrease in the photocurrent modulation, i.e., the minimum of the modulated light intensity is not zero. Although the modulation of the total light intensity is not perfect due to beating of the two modes with unequal powers, the difference of the maximum and the minimum intensity of the modulated light increases if the total optical power increases. This results in an increase in the amplitude of the AC component of the photocurrent. Therefore, the THz radiation

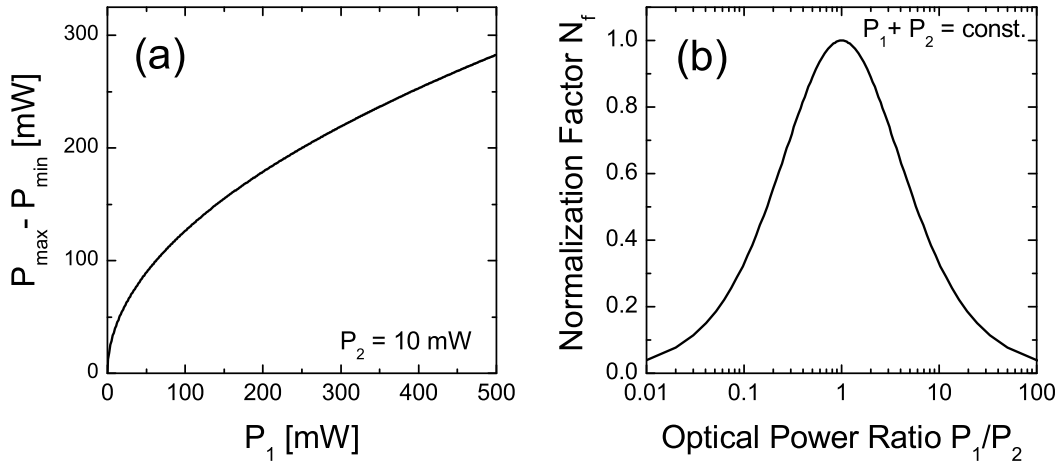

Fig. 3.4: Dependence of photomixing on optical power. (a): The difference between the maximum P_{max} and the minimum P_{min} of the optical power modulation: The power P_1 of one mode is varied and the power P_2 of the other is held constant at 10 mW. (b) Normalization factor N_f defined as ratio of THz power to the maximum achievable THz power as a function of optical power ratio of the laser modes. The total optical power is assumed to be constant.

is generated with higher power than that of the case with lower total optical power. Furthermore, an increase in the power of only one mode, keeping the other constant, results in an increase not only in the DC component but also in the AC component of the photocurrent so that the THz radiation is generated with increased power.

An example is displayed in Fig. 3.4(a). The difference between the maximum P_{max} and the minimum P_{min} of the modulated total optical power is depicted for the case of increasing power of one mode P_1 and holding the other P_2 constant at 10 mW. Eq. (3.1) indicates that the power difference $P_{max} - P_{min}$ increases with increase in P_1. Since $P_{max} - P_{min}$ is proportional to the square root of the power product of both modes, the generated THz power increases linearly with P_1. Therefore, increasing the total output power using high power SLs such as broad area SLs can achieve more THz power. However, the allowed optical power is limited by the acceptable power limit for the photomixer since the Joule heating in the photomixer at high DC photocurrents arising from high optical excitation causes thermal damage to the photomixer. It must be kept in mind that the equal power of both modes generates the maximum THz power in any case.

Another point which should be taken into account is the effectiveness of the THz generation when two laser modes have unequal powers at a constant total optical power. This point is especially important for the present work in which two laser modes

are generated simultaneously in the same semiconductor laser medium. A perfect equal optical power distribution into both modes is difficult to achieve due to mode competition between the participating modes. Therefore, it is necessary to look how sensitive the generated THz power is influenced by optical power differences of both laser modes. Since the maximum THz power is generated when both laser modes have the equal power, the effectiveness can be visualized by comparing the THz power generated by modes with unequal optical powers with the maximum THz power. The effectiveness can be expressed as a normalization factor N_f which is defined as the ratio of the generated THz power to the maximum achievable THz power at a given total optical power and a given frequency. As expressed by Eq. (3.3), the generated THz radiation is proportional to the product of the individual powers of both laser modes, expressed as $P_{THz} \sim P_1 P_2$. For the maximum THz power $P_{THz}(max)$, it meets the condition that $P_1 = P_2 = P_0/2$, where $P_0 = P_1 + P_2$ is the total optical power. The normalization factor is then given by

$$N_f = \frac{P_{THz}}{P_{THz}(max)} = \frac{4P_1P_2}{(P_1 + P_2)^2}. \tag{3.8}$$

Fig. 3.4(b) shows an illustration of the normalization factor of the THz generation as a function of the power ratio of both laser modes. The total optical power is assumed to be constant. It is irrelevant which mode has higher power than the other. N_f decreases as the power difference of both modes increases. If the optical power of one mode is 50 % higher than that of the other mode, N_f amounts to 0.96. This means that the THz power deviates 4 % from the ideally achievable power. For an optical power ratio of 2, the THz power deviation amounts to 11 %. Though the optical power of one mode is half the optical power of the other mode, the generated THz power amounts to 89 % of the ideal case. The THz power falls down to 50 % of the maximum available power only at a power ratio of 5.8. Therefore, slight difference in optical powers of both modes is not critical for effective generation of THz radiation.

Another significant meaning of N_f can be found by characterizing the THz radiation emitted by the THz-emitter. The THz emission is influenced by several factors of the THz-emitter such as optical power, applied bias voltage, characteristics of antennas and photomixers. Whereas the optical power and the applied bias voltage influence the generated THz power at a given THz frequency, the frequency characteristics of the generated THz radiation are determined by the antenna and the photomixer. In general, the THz-emitter is driven by a constant bias voltage so that the influence of the bias voltage can be assumed to be constant. However, in contrast to the bias voltage, the optical power is often subject to fluctuations so that the total optical power varies in time. Thus, to acquire the accurate frequency characteristics of the THz emission,

the generated THz power should be normalized to the square of the total optical power or, equivalently, to the square of the photocurrent of the antenna. This normalization filters out the influence of fluctuations in the total optical power. This holds for the ideal case for which the antenna photocurrent is modulated completely. However, the modulation of the photocurrent and in turn the generated THz power are dependent on the relative power of the participating modes, as discussed above. The normalization only by the photocurrent can thus lead to the false interpretation of the result for the case of $P_1/P_2 \neq 1$, which cannot be identified by the photocurrent alone. This contribution due to the difference in relative optical powers of both modes can be filtered out by normalizing the generated THz power to N_f. This additional normalization factor N_f compensates the deviation from the real frequency characteristics of the generation of THz radiation caused by the optical power difference of both modes.

Normalization of the generated THz radiation to both photocurrent and N_f gives characteristics of the THz emission which depend only on photoconductive materials and antenna structures. Therefore, for understanding the emission characteristics, it is necessary to have a closer look on the photoconductive materials and antennas.

3.1.3 Low-Temperature-Grown GaAs

For THz photoconductive applications such as photomixing or photoconductive detection, it is necessary to employ photoconductive materials with characteristic properties of short carrier lifetimes, high carrier mobilities, high electric breakdown fields, and high dark resistivities. The most important property of the material is the short carrier lifetimes, so that the material can respond to the optical modulation on subpicosecond time scales. The high carrier mobilities permit high photoconductivities. The high electric breakdown fields and dark resistivities allow application of large external fields and minimize dark currents. Low-temperature-grown GaAs (LT-GaAs) has the desired properties and is well suited for THz application.

LT-GaAs is grown by molecular beam epitaxy (MBE) on a GaAs substrate under As-rich conditions at substrate temperatures of approximately 200 °C, which are lower than the normal growth temperatures of 550 °C − 650 °C for high quality GaAs. LT-GaAs incorporates excess As with a concentration of 1 % − 2 % in the form of point defects − As antisites, As interstitials, or Ga vacancies − in the material [62, 63, 64, 65, 66, 67]. The incorporation of the excess As creates additional midgap states in the band gap of GaAs. The amount of excess As generally increases as the growth temperature is lowered. As-grown (i.e., unannealed) LT-GaAs can exhibit carrier lifetime as short as 90 fs [68] as a result of rapid trapping of electrons from the conduction band into the midgap states. However, such material has a low resistivity of about 10 Ωcm [67] due

to hopping conduction between these states [69]. By a post-growth anneal of LT-GaAs at temperatures above 500 °C, the excess As precipitates and forms As clusters so that the concentration of the As point defects is reduced. The annealed material has a high resistivity of about $10^7\,\Omega$cm [70]. However, the carrier lifetime also increases with increasing anneal temperature. Thus, a compromise between short carrier lifetimes and high resistivities has to be made with the appropriate combination of growth and anneal conditions. There is still controversy in relation to the role of point defects and As precipitates in explaining the optical and semi-insulating characteristics of annealed LT-GaAs [67, 71]. It has been suggested that the point defect dominates for as-grown materials, whereas the As precipitates play a significant role for annealed materials [72]. However, the microscopic mechanisms explaining these optical and semi-insulating characteristics of annealed LT-GaAs are not yet clearly known. It has been reported that LT-GaAs with high resistivity and with short carrier lifetime of about 100 fs can be obtained at anneal temperatures below 550 °C [68, 70]. The mobilities of the photoexcited carriers in LT-GaAs have been studied by many groups and give values from 120 cm^2/Vs to 4000 cm^2/Vs [63, 73, 74, 75]. Therefore, the short carrier lifetime, high mobility, and semi-insulating nature make LT-GaAs an attractive photoconductor for photomixing.

3.1.4 THz Antennas

The THz wave generated by photomixing is coupled out to free space as radiation by an antenna. Hence, it is instructive to introduce some basic principles of antennas. These principles enable to design antenna structures appropriate for desired purposes and understand characteristics of radiation emitted from the antennas. A general and detailed description about antennas can be found in Refs. [61, 76]

A time-varying current source has an accelerated charge distribution associated with it and creates a disturbance in the electromagnetic fields. This disturbance propagates away as radiation from the source of the disturbance. If charges oscillate, a regular disturbance is created and the propagating radiation is continuous. Antennas are designed to support charge oscillations. As current oscillations proceed in time on an antenna, the continuous radiation propagates away from the antenna. An antenna is a device that provides a means for radiating or receiving waves. In other words, it converts a guided wave on a transmission line to a free space wave (and vice versa in the receiving case). In general, antennas can be classified by their performance into four types [61]: electrically small, resonant, broadband, and aperture antennas. The antenna performance is characterized by parameters such as radiation pattern (which gives the angular variation of the generated radiation around the antenna), polarization

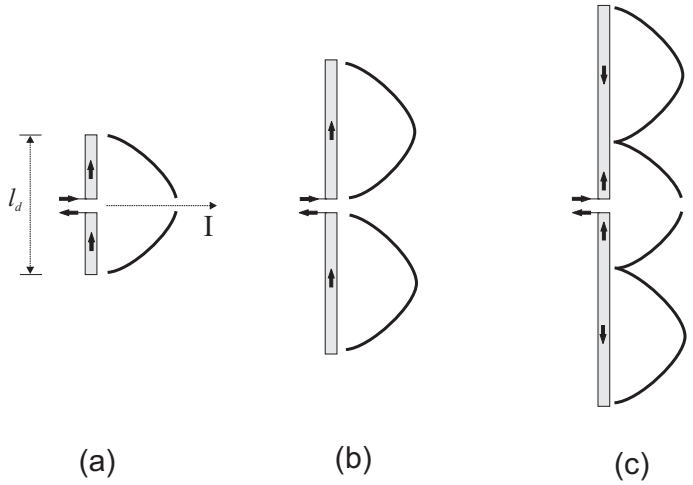

Fig. 3.5: Center-fed dipole antennas with various dipole lengths (l_d), and current distributions (I) on the dipoles. (a): $l_d = \lambda/2$ (half-wave dipole), (b): $l_d = \lambda$ (full-wave dipole), and (c): $l_d = 3\lambda/2$. The sinusoidal curves represent the current distributions on the dipoles. Arrows on the dipoles indicate relative current directions

(which describes the vector nature of electric fields radiated by the antenna), bandwidth (which is the range of frequencies with acceptable performance), and impedance. Especially resonant and broadband antennas concern the present work for the generation of THz radiation.

3.1.4.1 Dipole Antenna

A dipole antenna is a resonant antenna with a narrow bandwidth. The current distribution on the dipole antenna is approximately sinusoidal and must be zero at the ends. In Fig. 3.5, dipole antennas with various dipole lengths are plotted with current distribution on the dipoles. A widely used dipole antenna is the half-wave dipole antenna on which the current distribution varies as one-half of a sine wave with a maximum at the center. The currents on the top and the bottom halves of the antenna are in the same direction at any instant of time. Thus the radiation will be reinforced in a direction normal to the dipole due to effects from each half and will be weakest along the dipole axis. For dipoles longer than one wavelength, the currents on the antenna are not all in the same direction. It is then expected to observe large canceling effects in the radiation pattern due to oppositely directed currents on the antenna. The radiation pattern will be a multiple lobe structure. As the dipole becomes smaller than a wavelength, the pattern approaches that of the electrically small dipole, whose extent is much less than a wavelength. An electrically small dipole has smaller radiation resistance than

an ideal dipole which has a uniform current along the dipole. The smaller radiation resistance results in smaller radiation power than that of the ideal dipole. The larger radiation resistance associated with the uniform current of the ideal dipole can be approximately realized by providing a mechanism for charge accumulation at the dipole ends. One of the methods achieving this is to place horizontal transmission lines at the ends of the dipole. Since the current is sinusoidal along the wires with a zero at the ends, the horizontal wires provide an effective place for the charge to be stored. If the length of the dipole is much smaller than the wavelength, the current on the dipole is nearly constant. The radiation fields from the currents on the horizontal transmission wires almost cancel in the far field and the radiation comes mainly from the short vertical dipole. Hence, the antenna approximates an ideal dipole. An H-shaped dipole antenna exhibits this structure, which will be shown in section 3.2.1.

The dipole antenna has a radiation pattern which is well known from the dipole radiation and radiates a wave with linear polarization parallel to the dipole direction. Since dipoles are resonant-type antennas, their bandwidth is narrow, which amounts to about $8\,\% - 16\,\%$ of the center frequency [61]. In principle, the bandwidth of the dipole antenna is wider if the dipole becomes thicker. Therefore, the improvement of the bandwidth can be achieved by making the dipole thicker or employing a flat metal strip for dipole.

3.1.4.2 Log-Periodic Circularly Toothed Planar Antenna

In many applications, it is desirable that antennas operate effectively over a wide range of frequencies. Such antennas are referred to as broadband antennas. For broadband antennas, the bandwidth is generally defined as the ratio of an upper to a lower frequency for which their performance is acceptable [61]. An antenna can be classified into a broadband antenna if it operates over a bandwidth of 2:1 or 3:1, even though its pattern and impedance may change over that range. Bow-tie, spiral, and log-periodic antennas belong to this category. It is also desirable that the pattern and impedance of an antenna remain constant over a very wide range of frequencies. An antenna with constant pattern, impedance and polarization over a broad bandwidth is referred to as a frequency-independent antenna. However, few antennas fulfill these criteria.

Frequency-independent antennas can be designed by two principles: specification by angles, and self-complementary structure. It has been noted that if the shape of the antenna can be specified entirely by angles rather than lengths, its performance will be independent of frequency [77]. In addition, if the shape of the antenna is identical to that of its own complement, its impedance is independent of frequency and antenna shape [78]. The theoretical value of the impedance is then equal to $189\,\Omega$ in free space

and 72 Ω on a GaAs substrate. This is the self-complementary principle. Antennas that deviate from the self-complementary principle still have the broad bandwidth, but their impedance will vary with frequency. In many applications this may not cause significant trouble. A characteristic of frequency-independent antennas is their self-scaling behavior. Most radiation is emitted from the so-called active region. The active region is the portion of the frequency-independent antenna where its width (or its circumference) is one half-wavelength (or one wavelength). Since a resonance will build up in the current distribution where the width (or circumference) is one half-wavelength (or one wavelength), this resonance will be highly damped by radiation so that most of the current is dissipated in this resonance [77]. As the frequency changes, the active region moves to a portion of the antenna where the width is a half-wavelength. That is, the current can adjust in the region of the antenna structure as the frequency changes.

Frequency-independent antennas designed by the two design principles require a structure of infinite extent. However, the antenna in practice is of finite length, and its bandwidth is reduced since currents are abruptly terminated at the antenna ends, which is termed the end effect (i.e., the effect of finite length). The end effect can be reduced by designing the antenna structure such that its electrical properties vary periodically with the logarithm of the frequency [79]. Although this logarithmically periodic (log-periodic) antenna has the radiation characteristics and impedance repeating periodically with the logarithm of the frequency, the variations are practically small and the antenna is commonly regarded to be frequency-independent.

One of the log-periodic antennas is the log-periodic circularly toothed planar antenna depicted in Fig. 3.6. It is a bow-tie structure modified by a tooth structure. The log-periodic structure is defined by design parameters shown in Fig. 3.6. One parameter is the ratio of edge distances of successive teeth τ_a given by radii $R_n, R_{n+1}, ...$ from the center of the antenna and is defined by

$$\tau_a = \frac{R_{n+1}}{R_n} < 1. \tag{3.9}$$

The radii $r_n, r_{n+1}, ...$ give the same ratio. τ_a is constant and determines the period of the structure. If f_{n+1} and f_n are frequencies from adjacent periods having an identical performance, then

$$\tau_a = \frac{f_n}{f_{n+1}}, \tag{3.10}$$

where $f_n < f_{n+1}$. The tooth-width σ is another parameter, which is defined by

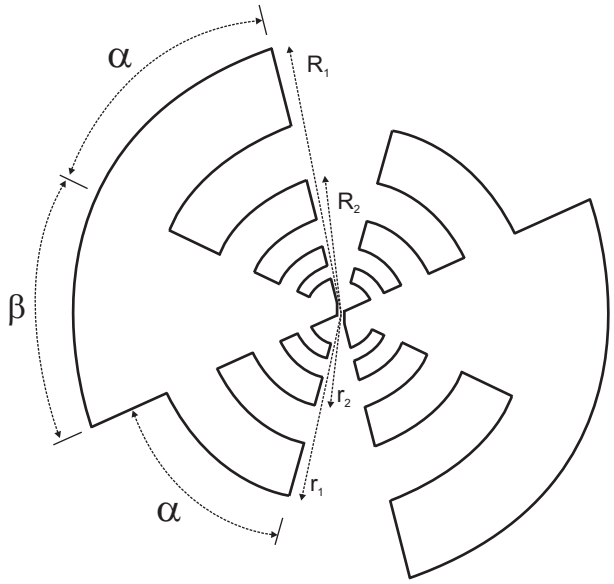

Fig. 3.6: Log-periodic circularly toothed planar antenna

$$\sigma = \frac{r_n}{R_n} < 1, \tag{3.11}$$

giving a relation of $\sigma = \sqrt{\tau_a}$ if the widths of the teeth and anti-teeth are equal. α and β are the angles determined by the teeth and bow-tie shape, respectively. The antenna structure can be made self-complementary by properly adjusting α and β.

Resonances are built on the teeth which are about one quarter-wavelength long so that most of the current appears on the resonant teeth (the active teeth). The frequency of periodic operation is limited by the largest and the smallest tooth which are about one quarter-wavelength long. The upper frequency limit of periodic operation is determined by the smallest tooth near the center, and the lower frequency limit is determined by R_1 and the angles α and β. The radiation is linearly polarized parallel to the active teeth edges, and the polarization direction will tilt periodically with frequency. Radiation patterns have two lobes whose maximums are directed normal to the plane of the antenna. It has been found that the radiation patterns are nearly uniform over a 10:1 bandwidth [79].

3.2 Experimental Setup

In chapter 2, as sources 2λ-ECSLs have been developed which emit two wavelengths whose difference wavelength can be tuned in the THz range. Using these lasers as

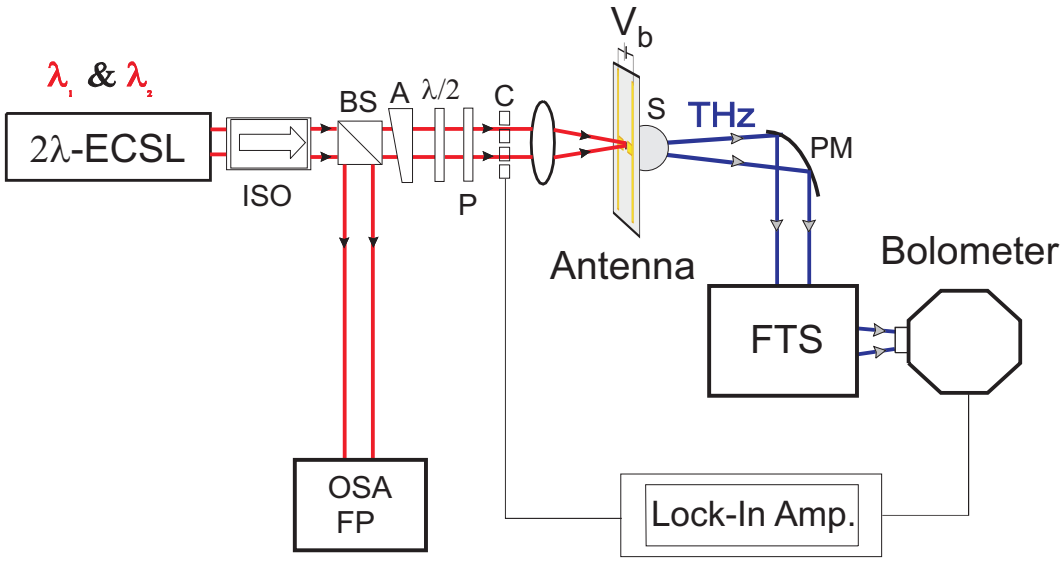

Fig. 3.7: Schematic of the experimental setup for generation and detection of tunable CW-THz radiation (ISO: optical isolator, BS: beam splitter, A: variable attenuator, $\lambda/2$: $\lambda/2$-plate, P: polarizer, C: chopper, V_b: bias voltage applied to antenna, S: Si lens, PM: parabolic mirror, FTS: Fourier-Transform spectrometer, OSA: optical spectrum analyzer, FP: Fabry-Perot interferometer).

optical sources, the generation of THz radiation has been performed via photomixing, and the generated THz radiation has been characterized.

The experimental setup of the tunable CW-THz system is depicted schematically in Fig. 3.7. A tunable dual-mode semiconductor laser with a double-external-cavity-configuration (2λ-ECSL) developed in the context of the presented work is used as an optical laser source. The collimated light emerging from the 2λ-ECSL is sent through an optical isolator (ISO, Isowave) to a beam splitter (BS). The beam splitter extracts a small portion of the incident light, which is used to monitor the optical spectrum of the laser light by an optical spectrum analyzer (OSA, Anritsu MS9710C) with a resolution of 0.05 nm and a scanning Fabry-Perot interferometer (FP, Melles Griot) with a free spectral range of 10 GHz. The other portion of the beam from the beam splitter is guided to an antenna through a variable beam-attenuator followed by a $\lambda/2$-plate and a polarizer. The laser light is chopped by a chopper with a duty cycle of 50 % and is then focussed by an aspheric lens with a focal length of 6.2 mm on the biased photomixer of the LT-GaAs antenna chip. The generated THz radiation is coupled out into free space through a hyperhemispherical high-resistivity Si lens (S) with a diameter of 10 mm which is attached to the backside of the antenna chip. The THz radiation is then collimated by an off-axis parabolic mirror (PM) with an off-axis focal length

of 43 mm and directed into a Fourier-Transform spectrometer (FTS) for the spectral characterization of the generated radiation. The outgoing radiation is detected by a liquid-Helium-cooled Si bolometer at the exit of the FTS. To improve the signal-to-noise ratio, a lock-in amplifier (SR530, Stanford Research Systems) is employed whose time-constant is set to 300 ms and whose reference frequency is provided by the mechanical chopper at a frequency of 137 Hz. In most of the cases for investigation of THz radiation, another parabolic mirror with an off-axis focal length of 10 cm is used instead of the FTS to focus the collimated THz radiation directly into the bolometer.

Two types of 2λ-ECSLs are used as optical dual-mode laser sources in the present investigation. Narrow stripe SLs emitting laterally single-mode are employed as SL sources in both types to avoid additional effects which can possibly arise in the case of multiple lateral modes. In chapter 5, generation of THz radiation using a SL with multiple lateral modes will be described. In the first type of 2λ-ECSL, a SL (Hitachi, HL7851G) with a central wavelength of 785 nm and a maximum output power of 50 mW is employed in a Double-Littman-Configuration. One facet of the laser has a high reflectivity and the other, which is used as light-emitting facet, has a low reflectivity. The laser is enclosed in a so-called TO-9 can and only one facet is accessible to couple out the light into free space. Therefore, the external Double-Littman-Resonator is used for this laser. The resonator length of the laser is about 670 μm so that the mode separation amounts to 0.13 nm (corresponding to 63 GHz at 785 nm). The resonator length of the external cavity is about 17 cm so that the spectral spacing of the external cavity-modes amounts to 880 MHz. The maximum available output power of this 2λ-ECSL is about 35 mW.

The other type of 2λ-ECSL employs a ridge waveguide SL (FBH) with a central wavelength of 825 nm and a maximum output power of 100 mW. Both laser facets of the FBH SL are accessible so that one facet with a reflectivity of 0.5 % is used for an external Double-Littrow-Resonator and the other with 34 % reflectivity is used as the output facet. The external resonator length is about 2.5 cm (corresponding to a mode space of 6 GHz). The resonator length of the solitary FBH SL is about 1.2 mm, which corresponds to a mode spacing of 37 GHz. The available output power of the FBH SL in this configuration amounts to about 55 mW. 2λ-ECSLs are sensitive to mechanical vibration and thermal influence coming from the environment. Especially because the laser-chip of FBH SL is exposed to the atmosphere, it is very sensitive to fluctuations caused by environmental air. In contrast to FBH SL, the laser HL7851G is enclosed in a TO-9 can so that it undergoes smaller fluctuations and emits light more stably than FBH SL. Therefore, most of the investigations have been performed using HL7851G in the Double-Littman-Configuration. Nevertheless, FBH SL in Double-Littrow-Configuration has proved to be useful for achieving a large detuning frequency

and effective generation of THz radiation. This will be shown in section 3.3.7.

The optical isolator is employed to prevent unwanted feedback of laser light from the Fabry-Perot interferometer and from the antenna chip. Especially the intensity of the reflected light at the antenna is too strong to maintain the stable dual-mode operation of the SL without optical isolation. This is due to the following fact. The laser light is focussed on the photomixer of the antenna chip which consists of LT-GaAs material and the metallic electrodes. The light reflected from the LT-GaAs and especially from the electrodes, which may act as mirrors, effectively propagates along the same route as the incident light back to the laser. Therefore, a high optical isolation is necessary to prevent instabilities of the laser emission arising by feedback from the antenna. The optical isolation of the used isolator in the present work is about 47 dB at a wavelength of 785 nm. In order to control the polarization state of the laser light, a $\lambda/2$-plate is placed in the laser beam and the polarization of the light is confirmed by a subsequent polarizer. As will be shown in the present chapter, maintaining a definite polarization state of the laser light with respect to the geometry of the photomixer is essential for effective generation of THz radiation. It should be noted that using a $\lambda/2$-plate and a polarizer to control the polarization state of the laser light needs extreme care. Because the laser light is focussed on the photomixer whose area amounts to $10\,\mu\mathrm{m}^2$, a slight deviation of the spot point of the laser light reduces the effectiveness of the photomixing. It is found that the rotation of the $\lambda/2$-plate and the polarizer displaces the spot point on the photomixer. This decreases the antenna current which is in turn related to the decrease of the THz generation. In order to achieve an optimal position of the spot on the photomixer, the antenna must be displaced to the position of the spot. However, this displacement again changes the optimal coupling of the generated radiation to the detector, which again needs to be adjusted to get an optimal coupling. Therefore, focussing the laser light on the photomixer and coupling the generated radiation into the bolometer require considerable care. The antenna chip is held by a plate which is placed on a micrometer-translator movable in 2 dimensions. The position of the antenna is controlled in a plane perpendicular to the incident light by two micrometer-screws for a coarse displacement and by two piezoelectric translators for a fine translation. The antennas are biased by a constant voltage source (Rohde & Schwarz DC Power Supply) up to a maximum of 20 V. This bias limit is set to avoid possible thermal burnout of the antenna that would occur at higher bias voltages. Employing the hyperhemispherical Si lens provides an efficient coupling of THz radiation from the antenna into free space. An antenna on a dielectric substrate radiates most of its power into the substrate rather than into the air [80]. The ratio of the radiation power into the dielectric to that into the air is $\epsilon_r^{1.5}$ [81], where ϵ_r is the relative dielectric constant of the substrate. For GaAs-substrate with $\epsilon_r = 12.9$, it is expected that 98 % of the power is transmitted into the substrate. However, the

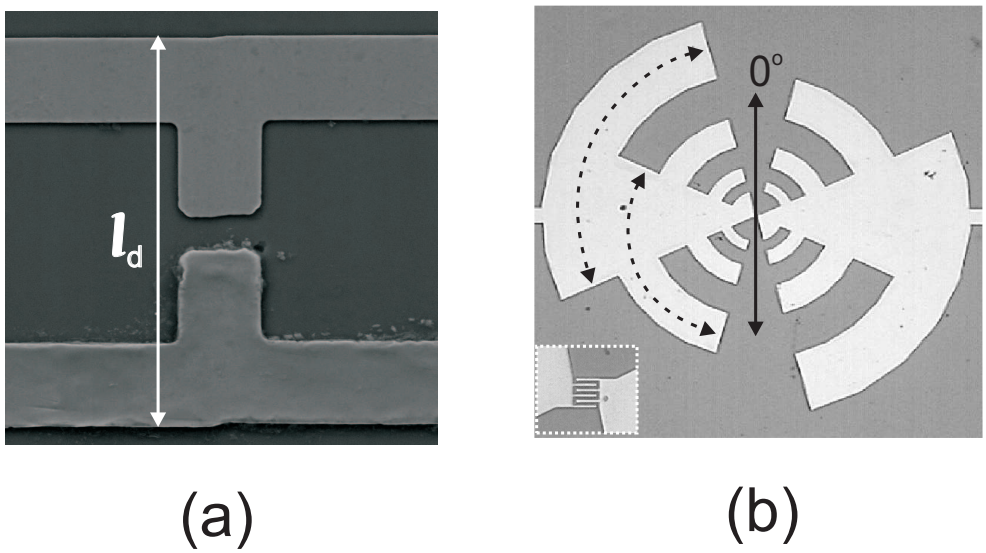

Fig. 3.8: Photograph of antennas. (a) a H-dipole antenna with a dipole length of l_d, (b) a log-periodic circular-toothed planar antenna with 6 teeth and 6 interdigitated electrode fingers (in inset at the left corner). The dashed lines represent the arc lengths l_1 and l_2 of the teeth. The vertical solid line in the middle of the log-periodic antenna designates the reference direction for the optical and THz-wave polarization.

radiation in the substrates that is transmitted at angles larger than the critical angle is entirely reflected due to the difference in the dielectric constants from the substrate into the air and is trapped as substrate modes. Therefore the radiation suffers from power loss into the substrate modes. A method to eliminate substrate modes is to place a dielectric lens such as a Si lens having approximately the same dielectric constant of $\epsilon_r = 11.7$ as the substrate on the substrate. Then, the lens does not support the substrate modes and couples most of the power into the free space of the substrate side. Nevertheless, there exists power loss due to the dielectric attenuation in the lens and the reflection from the lens into air. Studies about several types of lens geometry such as elliptical, hemispherical or hyperhemispherical lenses and their influence on the radiation coupling have been reported. The details are discussed in Refs. [81, 82, 83].

3.2.1 Properties of the Antennas

In the present work, two types of antennas are used to generate THz radiation. A photograph of the employed antennas is shown in Fig. 3.8. One type is an H-shaped dipole antenna with a dipole length of 70 μm and a width of 4 μm. There is a gap in

the center of the dipole with a length of 5 μm which serves as a photomixer with an area of 20 μm^2. The H-dipole structure is built lithographically by depositing 20 nm Ti and 100 nm Au on LT-GaAs with a thickness of 2 μm which, in turn, is grown on a 508 μm thick GaAs-Substrate. Resonance occurs when the dipole length l_d (white solid line in Fig. 3.8(a)) is equal to $\lambda_g/2$ [84], where the effective wavelength is given by $\lambda_g = \lambda_0/\sqrt{\epsilon_{eff}}$ with the effective dielectric constant $\epsilon_{eff} = (\epsilon_r + 1)/2$. Here, λ_0 is the free-space wavelength and $\epsilon_r = 12.9$ is the relative permittivity of GaAs. Thus, the resonance frequency for this dipole antenna is expected to be 810 GHz.

The other antenna-type is a log-periodic circular-toothed planar antenna [85]. The log-periodic antenna is fabricated on a 600 nm thick LT-GaAs layer by lithography. A 400 nm thick AlGaAs layer is grown on a semi-insulating GaAs substrate with a thickness of 350 μm. The LT-GaAs is then grown as an active photoconductive layer on the AlGaAs layer. A SiO_2 layer of 100 nm is deposited as antireflection coating onto the LT-GaAs layer. The log-periodic antenna has a photomixer with six 1 μm wide interdigitated electrode fingers with gaps of 1 μm between each of them. The fingers are 9 μm long so that the photomixer has an area of 10 μm by 11 μm. The antenna and finger structures are deposited directly on the LT-GaAs layer by evaporating a platinum layer with a thickness of 100 μm. The interdigitated electrode structure provides an increase in the length of the semiconductor-metal interface at the electrodes, which in turn increases the photocurrent in comparison to a conventional gap photomixer (i.e., photomixer without interdigitated electrodes). This improves the generated THz power. However, the inclusion of interdigitated electrodes leads to an increase in the device heating and in the capacitance. The resulting parasitic capacitance amounts to be about 3 fF [86], which restricts performance of the antenna at higher frequencies than 800 GHz. The log-periodic circularly toothed planar antenna is specified by the following design parameters [86, 87]: the outer radius is 640 μm, $\tau_a = \sigma^2 = 0.5$, where τ_a is the ratio of edge distance of successive teeth, and σ is the tooth-width. There are 3 teeth at each side of the bow-tie shape. The angle sustained by teeth and a bow-tie geometry is 50° each. The innermost portion of the antenna structure has a bow-tie shape with a bow angle of 100°. It has been obtained from a simulation [88] that the antenna impedance amounts to about 65 Ω, smaller than the self-complementary value of 72 Ω. Hence, the radiation power is slightly lower than that of the self-complementary antenna. As a result of log-periodic geometry, the antenna impedance as a function of frequency also shows a periodic behavior around 65 Ω. The real part of the impedance, Re{impedance}, is shown in Fig. 3.9. The frequencies corresponding to the maximums of Re{impedance} in Fig. 3.9 represent the simulated resonant frequencies of the antenna.

From the given antenna parameters, the resonant frequencies of the antenna can be cal-

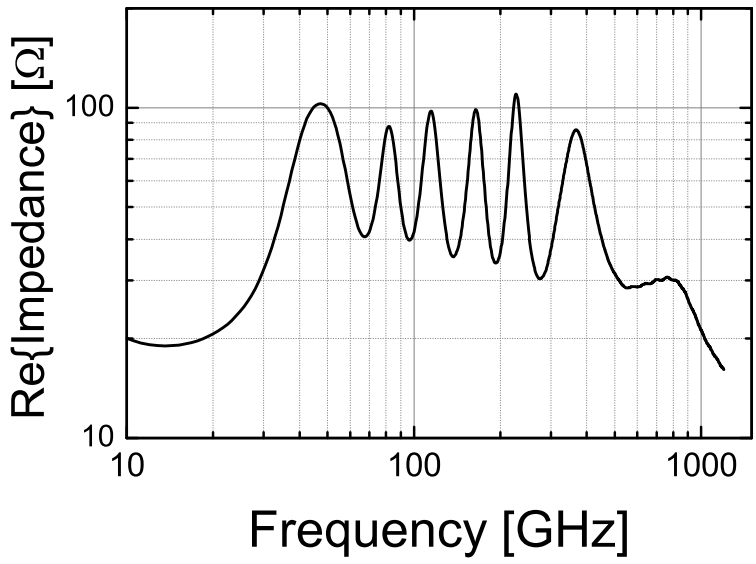

Fig. 3.9: The simulated real part of the impedance of the log-periodic antenna where the roll-off at 800 GHz is determined by photomixer. Courtesy of C. Sydlo.

culated analytically. The antenna is resonant when the tooth arc lengths are equal to $\lambda_g/4$, or alternatively, when the arc lengths l_n (such as black dashed lines in Fig. 3.8(b)) are equal to $\lambda_g/2$ [89, 90]. Using $l_n = \pi\overline{R}/2$ with $\overline{R} = (R_n + r_n)/2$, the resonant frequencies corresponding to the centers of the teeth can be calculated. The calculated resonant frequencies are listed in table 3.1. The table also contains the resonant frequencies obtained by the simulation in Fig. 3.9 and the calculated operating frequency ranges of teeth considering the inner and the outer arc lengths of each tooth.

tooth No. n	$f_{R,a}$ [GHz]	$f_{R,s}$ [GHz]	frequency range [GHz]
1	60	47.2	50.8 - 71.8
2	84	81.6	71.8 - 101.5
3	120	114	101.5 - 143
4	168	164	143 - 203
5	240	228	203 - 287
6	336	367	287 - 406

Tab. 3.1: Resonant frequencies f_R of the log-periodic antenna and the operation frequency range of each tooth. $f_{R,a}$ and $f_{R,s}$ denote analytically calculated and simulated resonant frequencies, respectively. The outer most and the inner most teeth are numbered 1 and 6, respectively.

As shown in table 3.1, the resonant frequencies obtained by the analytical calculation and the simulation show slight differences. The analytical values are calculated assuming that the antenna is resonant at the center of the tooth. However, it is not yet clearly known whether the antenna is actually resonant at the center of the tooth. Therefore, the simulated values are chosen as reference for the resonance frequencies.

3.2.2 Bolometer

For detection of the THz radiation, several methods can be employed such as the photoconductive method [9], electro-optical method [11], and direct detection using thermal detectors such as a Golay cell, Deuterated Triglycine Sulfate (DTGS) detectors [91], and bolometers. Among thermal detectors, bolometers are the most sensitive and broadband detectors and are especially adequate for detection of far-infrared radiation with very low power below picowatts. A bolometer consists of an absorbing element with heat capacity C connected to a thermal bath at temperature T_0 through thermal conductance G. The absorber converts the incident radiation into heat. The balance between the power variation ΔP of the incident radiation and the heat leakage into the thermal bath results in the temperature variation ΔT of the absorber. An electrical resistance thermometer such as doped Si or Ge which is attached to the absorber measures the temperature variation of the absorber via the resulting resistance change $\Delta R = (dR/dT)_{T_0}\Delta T$. In the case of a constant bias current, a small current I is sent through the thermometer and a voltage output $\Delta V = I\Delta R$ proportional to ΔP is obtained through an associated readout circuitry. Placing a Winston cone in front of the detection element maximizes the collection of incoming radiation onto the detection element. The operating frequency range is usually determined by a series of bandpass filters located in front of the Winston cone. In order to achieve the highest sensitivity, the bolometer is usually operated at or below liquid Helium temperature. The performance of the bolometer increases as the operating temperature is lowered. More detailed description about bolometers is given in Refs. [92, 93].

In the present work, a silicon bolometer (Infrared Laboratories) cooled at 4.2 K has been used to achieve high sensitivity. It consists of a doped Si element in vacuum attached to a cooled substrate by lead wires. Two filters for frequencies 800 cm^{-1} and 100 cm^{-1} are positioned in front of a Winston cone. The signal output is amplified by a preamplifier with a gain of either 200 or 1000. It has a responsivity of $2.39 \times 10^5\, VW^{-1}$ (given by manufacturer) at the operating temperature 4.2 K.

Bolometers offer essentially no spectral resolution. In order to achieve spectral resolution, bolometers can be incorporated into a Fourier transform spectrometer, which will be described in the next section.

3.2.3 Fourier Transform Spectrometer

In the range of far-infrared wavelengths, a Fourier transform spectrometer (FTS) is usually used as a spectroscopic tool. The advantages of FTSs compared to conventional grating spectrometers arise from the following points. Since information of all spectral elements in a given spectrum range is incident on a detector at the same time, information about the entire spectral range can be acquired with a constant resolution during an entire scan. The interferometer can also have a large entrance aperture so that it can collect large amount of energy at high resolution. These advantages result in fast scanning times and a large signal-to-noise ratio, and are especially important for far-infrared wavelength range, where there is a lack of intensive light sources and sensitive detectors.

The basic principle of FTS is based on a two-beam interferometer. The incident beam is divided by a beam splitter into two beams, which pass different optical path lengths. The two beams overlap again at the exit of the interferometer to form a resulting beam. The intensity of the resulting beam is recorded as a function of optical path difference of the two beams using a detector. The recording of the detected signal versus optical path difference is called the interferogram. It contains the whole information about the incident spectrum. The spectrum, i.e., intensity versus frequency, can finally be obtained by Fourier analysis of the interferogram. Resolving powers of the two-beam interferometers are limited only by the maximum optical path difference of the interferometers. The detailed theory and applications of the FTS can be found in Refs. [94, 95].

In the present work, a calibrated and modified FTS (Polytec FIR30) [96] is used for spectral analysis of the generated THz radiation. The optical part of the FTS is schematically depicted in Fig. 3.10. It consists of a Michelson interferometer for the spectral range from $10\,\mathrm{cm}^{-1}$ to $1000\,\mathrm{cm}^{-1}$ and a Si bolometer as a detector. Two plane mirrors M1 and M2 guide the incident beam to a beam splitter BS. The Michelson mirrors consist of a movable plane mirror M3 and a fixed plane mirror M4. The plane mirror M5 guides the superimposed beam to an off-axis paraboloid M6 which focuses the beam on the detector outside the interferometer.

For different wavelength ranges, four polyethylene terephthalate (also called Mylar) films with different thickness mounted on a rotatable wheel are used as beam splitters. The operating frequency range and the corresponding beam splitter thickness are described in table 3.2.

Since the spectral characterization of the radiation in the present work is concentrated between 100 GHz and 1 THz, only the beam splitter with the thickness of $50\,\mu m$ is of interest. It should be noted that, in contrast to the classical Michelson interferometers,

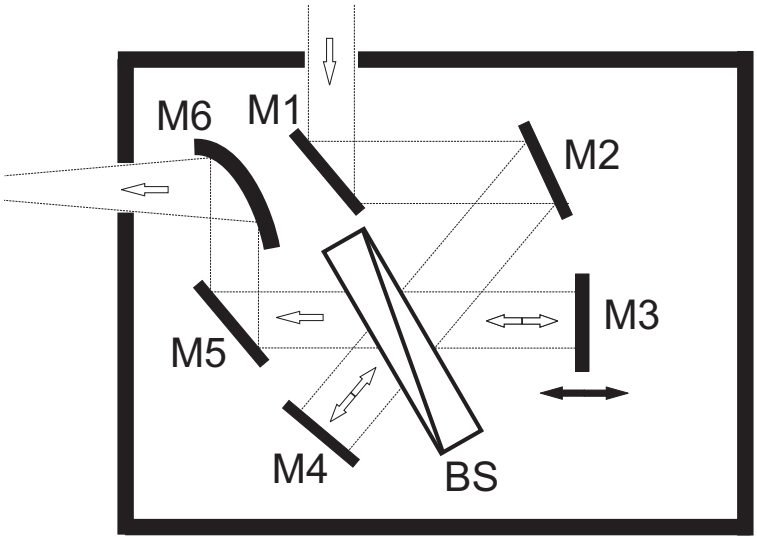

Fig. 3.10: Experimental setup of a Fourier Transform Spectrometer

frequency range [cm^{-1}]	15-45	30-140	100-380	300-1000
thickness [μm]	50	15	6	2.5

Tab. 3.2: Beam splitters employed in the FTS

the light path to the beam splitter in the employed interferometer has an incident angle of about 30°. This configuration is more advantageous due to the following two aspects. It reduces, on the one hand, the surface area of the beam splitter which is necessary to be illuminated at a given beam diameter. On the other hand, effects of polarization which can occur due to reflection at the beam splitter are suppressed. The movable mirror is operated by an electric motor with a minimum step increment of 2 μm. Its displacement is measured by a linear incremental measurement system (Heidenhain LIDA 181). The minimum achievable optical path difference of the interferometer, thus, amounts to 4 μm. This minimum achievable path difference limits the highest resolvable frequency which is sometimes called the Nyquist frequency. The present interferometer can resolve the smallest wavelength of 8 μm. The mirror can be moved to a maximum distance of 10 cm so that the theoretical maximum frequency resolution is 1.5 GHz. The electronic control of the interferometer and the recording of the interferogram are performed by a computer.

3.3 Results and Discussion

The generation of THz radiation using photomixing of two laser modes is a method to realize a tunable CW THz source. In this section, the generated THz radiation is characterized. Most of the investigation of generation of THz radiation is performed by using the Double-Littman-Configuration, in which the HL7851G SL with a central wavelength of 785 nm is employed, since the laser showed stability against fluctuations caused by environmental air. The generation of THz radiation using the FBH SL with a central wavelength of 830 nm in the Double-Littrow-Configuration will be shown in a following section. Most of the signals recorded by lock-in detection are amplified by a preamplifier with a gain of 200 so that the real bolometer signal amounts to (lock-in signal)/200. If another gain of the preamplifier is used in the measurements, then it will be described explicitly in the context. Since the lock-in signal is proportional to the detected THz radiation power, the lock-in signal power and the THz radiation power are used equivalently in the present section unless it is explicitly mentioned.

In the following, the generation of THz radiation via photomixing is characterized. A log-periodic circular-toothed planar antenna is employed as a radiation emitter. The generation characteristics are first investigated, followed by the temporal behavior of the generated radiation. After subsequent investigations of the influence of the optical polarization on the generation of THz radiation and spectral analysis of THz radiation, frequency- and polarization-dependence of THz radiation are investigated. Finally, the generation of THz radiation using a H-dipole antenna is investigated.

3.3.1 Characteristics of THz Radiation Generation

In the present section, the generation of THz radiation is characterized. The incident dual-mode laser light with a difference frequency of 321 GHz and a total output power of 21 mW is chopped at 185 Hz and focussed on the photomixer device which is biased by a voltage source. Since the laser beam is chopped by a chopper with a duty cycle of 50 %, the averaged total optical power incident on the photomixer amounts to 10.5 mW. To characterize the bias voltage dependence of the THz generation, the applied bias voltage is varied from 0 to 20 V at a constant optical power of 10.5 mW incident on the photomixer. For characterization of the optical power dependence of the THz generation, the bias voltage is held constant at 18 V and the optical power incident on the photomixer is varied from 0.5 to 10.5 mW by using a variable attenuator. Although the applied electric field is nonuniform for interdigitated electrode fingers, the electric field E_b can be simply approximated by the relation of $E_b = V_b/d_g$, where V_b is the bias voltage between the electrode fingers and d_g is the spacing between the fingers. Here,

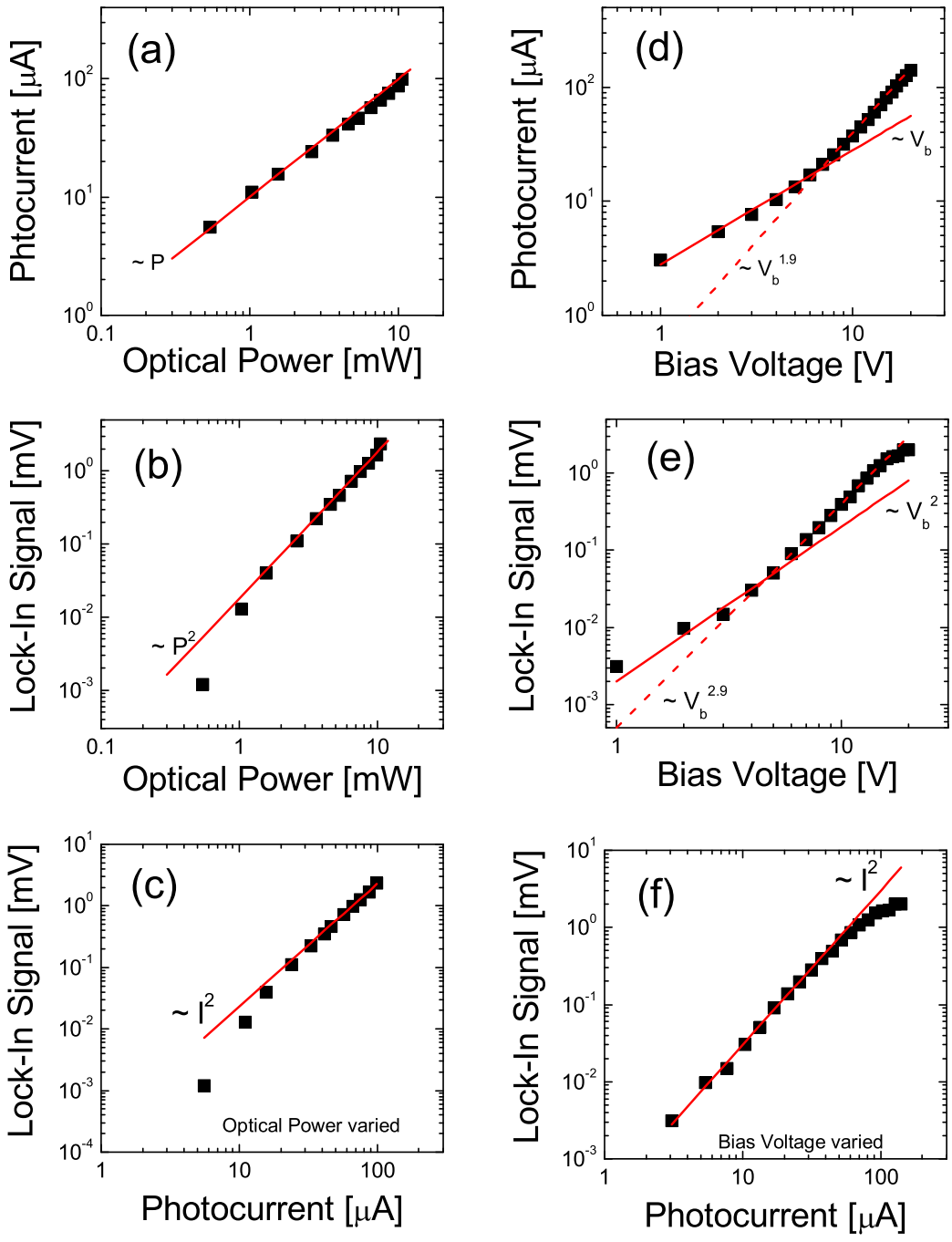

Fig. 3.11: The measured (open squares) and fitted (solid and dashed lines) relations between: (a) photocurrent and optical power, (b) lock-in signal and optical power, (c) lock-in signal and photocurrent measured by variation of the optical power at a constant bias voltage of 18 V (left); (d) photocurrent and bias voltage, (e) lock-in signal and bias voltage (f) lock-in signal and the photocurrent measured by variation of the bias voltage at a constant optical power of 21 mW (right).

the resulting field E_b amounts to $1.8 \times 10^5\,\mathrm{Vcm}^{-1}$, which lies below the breakdown field of about $5 \times 10^5\,\mathrm{Vcm}^{-1}$ in typical LT-GaAs [97]. The results are depicted in Fig. 3.11.

First, the optical power dependence of THz generation is characterized. The photocurrent increases linearly with increasing optical power (Fig. 3.11(a)) at a fixed bias voltage. This relation is expected from the well-known photoelectric effect. The solid line displays the fitted linear relation ($\sim$ P). From the measured relation between the photocurrent and the optical power, an external quantum efficiency η_e of the photomixer can be estimated according to $I = \eta_e(e/h\nu)P$, where I, e, $h\nu$ and P represent photocurrent, electron charge, photon energy, and optical power incident on the photomixer, respectively. η_e indicates the efficiency of converting the optical signal incident on the photomixer to an electrical signal and is experimentally determined to be about 0.008 using the data of Fig. 3.11(a). Since the photomixer employs an electrode finger structure, η_e comprises the loss due to the reflection of the laser light from the finger. The optical coupling efficiency η_{op}, which accounts for the reflection loss of the laser light incident from the air onto the photomixer, can be expressed as [22, 98]

$$\eta_{op} = \frac{N_g d_g}{N_g d_g + N_e d_e} \frac{4 n_{\mathrm{LT}}}{(n_{\mathrm{LT}} + 1)^2}, \tag{3.12}$$

where n_{LT} is the (wavelength-dependent) refractive index of the LT-GaAs, d_g and d_e represent the width of the gap between the electrode fingers and the width of the fingers, respectively, and N_g and N_e represent the number of gaps and the electrodes, respectively. Assuming that the reflection of the laser light from the photoconductive material is negligible due to the antireflection coating with SiO_2, η_{op} can be approximated as

$$\eta_{op} = \frac{N_g d_g}{N_g d_g + N_e d_e}. \tag{3.13}$$

With $N_g = 5$ and $N_e = 6$ and the same width size for both gaps and electrodes, η_{op} is estimated by Eq. (3.13) to be 0.45. Furthermore, the quantum efficiency η_i of the photoconductive material, indicating the number of photocarriers generated per photon entering the material, has to be taken into account for η_e. Therefore, η_e can be expressed as $\eta_e = \eta_{op}\eta_i$. The quantum efficiency η_i of the photoconductive material is then determined by the above values for η_e and η_{op}. Assuming that all incident photons are absorbed in the material, η_i amounts to 0.018. It should be noted here that the optical coupling efficiency is dependent on the polarization orientation of the incident laser light with respect to the electrodes, which will be discussed in detail in section 3.3.3. The dependence of THz radiation power on the optical power is displayed in

Fig. 3.11(b). The THz radiation power increases quadratically with the optical power at a fixed bias voltage. The maximum obtained signal-to-noise ratio amounts to 144:1 at 10.6 mW. Since the photocurrent is linearly proportional to the optical power, the THz radiation power also increases quadratically with the photocurrent, as shown in Fig. 3.11(c). The solid lines in the figures represent the fitted quadratic relations of the THz radiation power to the optical power and the photocurrent, respectively. These relations are expected from the photomixing theory, as has been presented in section 3.1.1.

For the case of bias voltage dependence of the photocurrent at a constant incident optical power incidence, as shown in Fig. 3.11(d), the photocurrent shows a linear ($\sim V_b$, displayed by the fitted solid line) dependence on the bias voltage up to 6 V and a superlinear ($\sim V_b^{1.9}$, displayed by the fitted dashed line) dependence at higher bias voltages. The linear dependence indicates ohmic transport in bulk LT-GaAs [99]. The superlinear bias dependence of the photocurrent has also been observed previously [99, 100, 101] and is attributed to the field-dependent carrier lifetime in the LT-GaAs [101]. At high bias voltages the carrier lifetime increases with increasing bias, which results in an increase in the steady-state electron concentration. Thus, the photocurrent increases superlinearly with increasing bias at high bias voltages. The generated THz radiation power as a function of bias voltage is depicted in Fig. 3.11(e). The THz radiation power shows a quadratic increase with bias voltage up to 5V, followed by a superquadratic increase at higher voltages up to 16 V. Above 16 V, the radiation power increases with a saturation feature. The displayed solid and dashed fit-lines represent the quadratic ($\sim V_b^2$) and superquadratic ($\sim V_b^{2.9}$) relations between the THz radiation power and the bias voltage, respectively. While the quadratic increase is predicted by the photomixing theory, the superquadratic behavior is expected from the superlinear increase in photocurrent as a function of bias voltage at high bias, since the generated THz radiation power should be proportional to the square of the photocurrent. Therefore, it is expected that the radiation power should exhibit a dependence of $\sim V_b^{3.8}$ on the bias voltage. However, the measured data exhibits a relation of $\sim V_b^{2.9}$. This result indicates that at high bias the increased photocurrent may contain more DC photocarriers not contributing to the generation of THz radiation, which is more clearly exhibited in Fig. 3.11(f). The THz radiation power increases quadratically with photocurrent up to 37 μA, as depicted by the fitted line of $\sim I^2$, followed by a saturation feature at higher photocurrents. This saturation may be due to the photocarriers which are not modulated at the beat frequency of the two laser modes. These DC photocarriers could be due to, on the one hand, an increase of lifetime with increasing bias as mentioned above and, therefore, cannot be modulated by the beat frequency of the laser modes at a given frequency. Therefore, the generated THz radiation power is lower than expected. On the other hand, another reason could be the possible generation of photocarriers in the

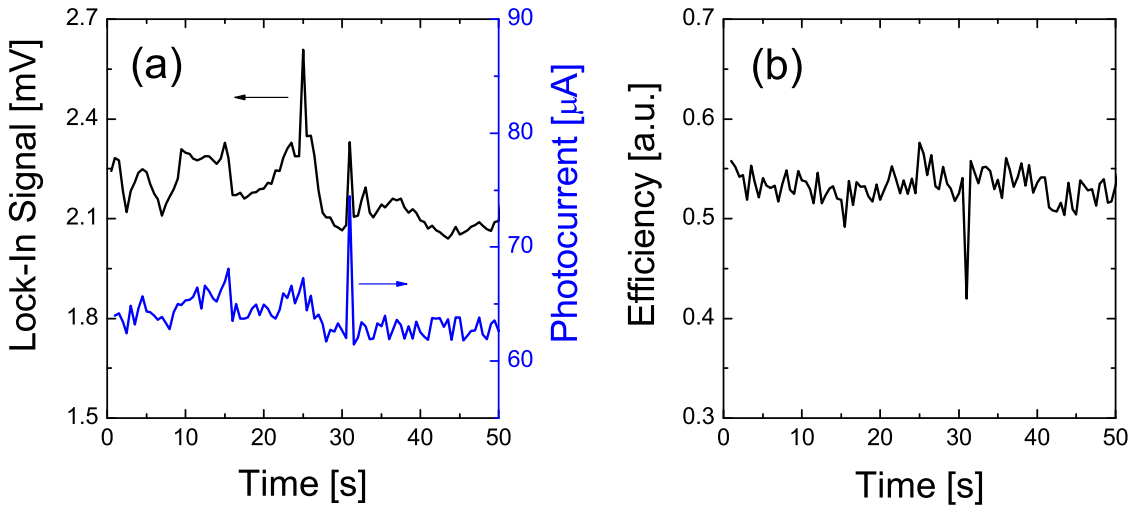

Fig. 3.12: (a) THz power and antenna photocurrent measured in a time interval of 50 s. The difference frequency of the two laser modes is 583 GHz. (b) Corresponding efficiency of the generation of THz radiation in the same time interval.

GaAs substrate, which have a lifetime of a few nanoseconds, and the contribution of these photocarriers to the photocurrent [102]. The optical light which is not completely absorbed in the LT-GaAs layer generates photocarriers in the adjacent GaAs-substrate. These carriers can then be collected at high bias, which in turn results in an increase in the photocurrent. Because of their long lifetime, the carriers cannot be modulated at the THz beat frequency and contribute to the photocurrent without generation of THz radiation. At present, the mechanisms contributing to these phenomena have not been clearly identified yet and are still a research issue.

3.3.2 Temporal Behavior of the Generated THz Radiation

The temporal stability of the generated THz radiation is an important factor for applications such as imaging and spectroscopy. To investigate the temporal behavior of the THz radiation, the dual-mode laser light with a difference frequency of 583 GHz and a total output power of 28 mW is chopped and focussed on the photomixer biased at 15 V. The photocurrent of the antenna and the THz radiation power are detected in a time interval of 50 s since the start of the dual-mode operation of the SL and consequently generation of THz radiation.

Fig. 3.12(a) displays the time development of the THz radiation and the antenna photocurrent measured for 50 s. THz radiation and the photocurrent exhibit a non-stable temporal behavior with fluctuations in the first 31 s which lie within 4 % and 2 % of

the average values, respectively. After 31 s, THz radiation and the photocurrent are stabilized within 2 % and 1 % of the average values for THz radiation and the photocurrent, respectively. Figure 3.12(a) shows the stability of the THz radiation and the photocurrent on a time scale of tens of seconds after 31 s. Fluctuations of THz radiation follow quadratically those of the photocurrent, which in turn result from optical power fluctuations. Thus, the stability of the optical source is crucial for the generation of the stable THz radiation. The result obtained here indicates that generated THz radiation can be temporally stable. It is worthy noting two peaks in the THz radiation at 25 s and 31 s and a peak in the photocurrent at 31 s. The first peak in THz radiation at 25 s is 17 % higher than that of the average value, whereas the photocurrent does not exhibit such a high peak at the corresponding time and has the same level as the neighboring points. The second peak in the THz radiation at 30 s is accompanied by a peak in the photocurrent at the corresponding time. However, the peak in THz radiation shows the same power level as that of points below 31 s, whereas the peak in the photocurrent reveals 19 % higher peak than that of the average value. To clarify these points, it is necessary to examine the generation efficiency of THz radiation.

According to the photomixing theory and the result obtained in the previous section, the power of the generated THz radiation is proportional to the square of the antenna photocurrent. This means that fluctuations of the optical power in time influence the THz radiation power. As discussed in section 3.1.2, THz radiation power can be normalized to the square of the photocurrent to cancel this effect. For an accurate interpretation of the behavior, the THz radiation power should also be normalized by the normalization factor N_f. N_f is here assumed to be constant because the relative power of the two laser modes is constant for most of the detection time. The normalized THz radiation power then gives a generation efficiency of THz radiation. The generation efficiency calculated from the measured data is displayed as a function of time in Fig. 3.12(b). The efficiency is relatively constant in time and the deviation lies within 3 % of the average value.

Comparing the temporal behavior of the generation efficiency with those of THz radiation and the photocurrent, the generation efficiency at 25 s which corresponds to the first peak of the THz radiation is 8 % higher than the average value, though the photocurrent does not exhibit such a clear increase. This increase in THz radiation power can be attributed to a sudden decrease in power difference of the two laser modes. As discussed in section 3.1.2, the decrease in the power difference of the two laser modes at a constant total output power increases the modulation of the photocurrent. This results in an increase in THz radiation power and the corresponding efficiency. In contrast to that, the photocurrent and the corresponding THz radiation power both exhibit increases at 31 s. However, the generation efficiency shows a dip at 31 s. This

decrease in the efficiency in spite of the increase in the THz radiation power can be attributed to a sudden increase in total output power of the laser accompanying an increase in the power difference of the two laser modes. As shown in section 3.1.2, the increase in total output power due to a power increase only in one mode also gives rise to an increase in the THz radiation power. However, in this case, an increase in the DC component of the photocurrent is larger than an increase in the AC component. Since the DC component does not contribute to the generation of THz radiation, the generation efficiency expressed by normalization of the THz radiation power to the square of the DC photocurrent is low in this case. Therefore, the efficiency at 31 s is clearly lower than the average value.

In conclusion, the stability of the generated THz radiation follows the stability of the optical source. Although the temporal behavior of the generated THz radiation is shown for the time interval of 50 s, the temporally stable THz emission over several ten times longer time scales can be realized in the present work. This enables long-term investigation of the generated THz radiation such as polarization characterization and spectral characterization using the FTS. These investigations will be discussed in the following sections.

3.3.3 Influence of Optical Polarization on THz Generation

In the previous sections, the generation of THz radiation and its temporal behavior have been studied. In this section, the influence of the polarization orientation of the optical light on the THz generation will be investigated. The interdigitated electrode finger structure of the photomixer on the semiconductor material constitutes a grating because its size is comparable to the optical wavelength. Therefore, it is expected that the THz generation depends on the polarization direction of the optical light due to the grating effects [103, 104, 105].

In the present section, the effect of the optical polarization on generation of THz radiation is investigated. A linearly polarized CW dual-mode beam which is emitted from the 2λ-ECSL with a difference frequency of 263 GHz at a center wavelength λ_c of 785 nm is incident on the antenna, and is focussed on the active area of $10 \times 11\,\mu\text{m}^2$ of the photomixer. Since each of six interdigitated electrodes with a thickness of 1 μm is separated by a gap of 1 μm, an electrode period $\Lambda = d_e + d_g$ amounts to 2 μm. This results in a ratio of the electrode period to the center wavelength of $\Lambda/\lambda_c = 2.5$. The optical power is held constant at 27 mW and the antenna is biased constantly at 15 V. The rotation of the polarization direction of the incident light is performed by using a $\lambda/2$-plate with a rotation interval of 10° from 0° to 360°. The polarization direction is defined as 0° with respect to the direction of the electrode fingers if the

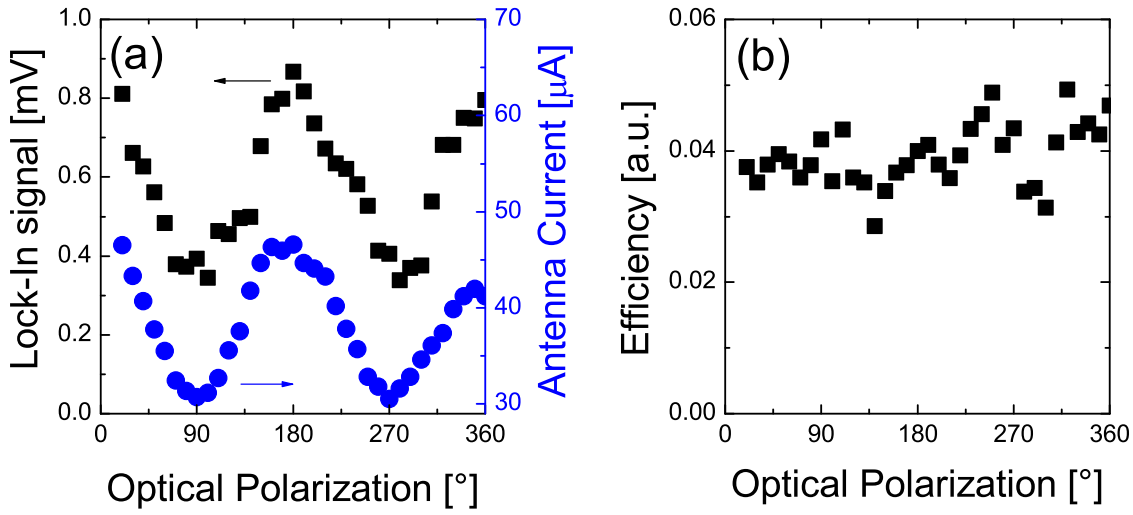

Fig. 3.13: The generated THz signal and antenna current (a) and THz generation efficiency (b) as a function of the polarization of the incident optical light. Optical polarization of 0° is defined by the direction perpendicular to that of the interdigitated electrodes of the log-periodic antenna.

electric field vector of the laser light is perpendicular to the direction of the fingers. The 0°-direction is displayed in Fig. 3.8(b). The polarization direction is confirmed by a following polarizer. The THz power and the antenna photocurrent are measured as a function of the polarization direction of the incident laser light.

Fig. 3.13(a) shows the measured THz power and the antenna photocurrent as a function of the optical polarization direction. The THz power and the antenna current both show approximately sinusoidal behaviors with a maximum at 180° (or 0°) and a minimum at 90° (or 270°). This result shows that the generation of THz radiation and the antenna photocurrent, which determines external quantum efficiency η_e of the photomixer, both are dependent on the direction of the optical polarization. The maximum values of the THz power and the antenna current are achieved if the optical polarization is oriented perpendicular ($\perp$) to the direction of the electrode fingers. The minimum occurs when the optical polarization is oriented parallel ($\parallel$) to the finger direction. The ratio between photocurrents excited by light with the perpendicular and the parallel polarization can be extracted from the measured data. If $I_\perp$ and $I_\parallel$ are defined as the photocurrents generated by perpendicularly and parallel polarized light, respectively, then the measurements show that $I_\perp/I_\parallel = 1.5$. This value is in good agreement with the value of 1.3 reported in Ref. [105] for a value of $\Lambda/\lambda_c = 1.5$. The calculation of the ratio between the THz powers $P_\perp$ and $P_\parallel$ generated by the perpendicularly and parallel polarized light from Fig. 3.13(a) results in a THz power

ratio of $P_\perp/P_\parallel = 2.6$, which is in agreement with the squared value of the photocurrent ratio giving $I_\perp^2/I_\parallel^2 = 2.3$. Since the generated THz power should be proportional to the square of the antenna photocurrent according to the photomixing theory, the efficiency of THz generation attributed to the photocurrent can be obtained by dividing the THz radiation power by the square of the photocurrent. This efficiency should show a constant value independent of the optical polarization direction of the incident light, because photomixing itself contains no parameters which could be dependent on the optical polarization as long as both laser modes have the same polarization. Fig. 3.13(b) displays this calculated efficiency of the THz generation as a function of the polarization direction. The efficiency exhibits a nearly constant behavior independent of the polarization direction. This result indicates that the efficiency of THz generation is independent of the polarization direction of the incident light and is only determined by the photocurrent. Therefore, the increase in THz radiation power is influenced by the increase in the photocurrent, which is attributed to change in the optical coupling efficiency η_{op} induced by the grating effect of the interdigitated electrodes.

Since the geometrical size of the fingers and the gap between them is larger than the laser wavelength, the polarization effect is not large, compared to the case of finger structures smaller than the optical wavelength [105]. Moreover, the polarization dependence in the photocurrent is also observed when the antenna is illuminated with single-mode laser light. Because the photomixer acts as a detector, there should be no difference between dual-mode and single-mode light incidence on the photomixer. This is confirmed by the result that the illumination with a single-mode laser beam also gives a ratio of $I_\perp/I_\parallel = 1.6$. Since the LT-GaAs substrate has no contribution to the polarization effects, the above polarization dependence is thus caused by the optical coupling difference due to the micrometer-size interdigitated electrode structure. It has been reported that the THz generation is dependent on the polarization direction of the exciting optical pulse, but the generated photocurrent is independent of the polarization direction [106]. This polarization sensitivity has been proposed to be due to the polarization dependence of the overlap between the high electric-field region and the photocarrier distribution. The maximum THz generation was thereby achieved at the polarization direction perpendicular to the edge of the electrodes with a gap of $50\,\mu m$ and $\sqrt{P_\perp}/\sqrt{P_\parallel}$ was varied up to a factor of 4. However, this phenomenon could not be confirmed in the present investigation. The results obtained in the context of the present section indicate that the optical polarization dependence of the THz generation is rather attributed to the grating effect.

Therefore, it is important to control the polarization of the incident light to maximize the optical coupling to the photomixer, which results in maximum THz generation. To maximize the THz generation, all investigations in the present work are performed

under incident laser light, whose polarization direction is oriented perpendicular to the finger direction.

3.3.4 Fast Fourier Transform Spectra

The spectral characteristics of the generated THz radiation depend on the spectral characteristics of the participating laser modes. In order to characterize the THz radiation, spectroscopic investigations of the generated THz radiation are performed using a FTS. Simultaneously, the optical spectra are analyzed by an OSA and a scanning Fabry-Perot interferometer. The laser is driven at a constant injection current of 187 mA. The input power of the laser light incident on the photomixer is 12 mW due to chopping. The antenna is biased at a voltage of 15 V.

Fig. 3.14(a) shows an optical spectrum of the laser emission in which two spectrally filtered laser modes and a weak four-wave mixing (FWM) sideband are oscillating. The wavelengths of the modes are 784.14 nm and 785.98 nm, respectively. This gives a difference wavelength of 1.84 nm which corresponds to a difference frequency of 896 GHz. The simultaneous spectral scan by a Fabry-Perot interferometer with FSR = 10 GHz monitors the spectral purity of the dual-mode operation with higher resolution. As shown in Fig. 3.14(b), the laser emits only two external cavity modes which appear as clear peaks with comparable intensity ratio of 1:0.7 in the Fabry-Perot scan. The linewidth of each mode is measured to be 60 MHz. Since the external cavity modes have a mode spacing of 880 MHz, the Fabry-Perot scan should reveal any possible additional external cavity modes. As discussed in chapter 2, this optical spectrum shows the coherent dual-mode lasing regime in which each of the two main lasing frequencies contains only a single external cavity mode [47]. At the same time, the generated THz radiation is spectrally characterized by FTS measurement. The recorded FTS interference signal of the generated THz radiation is shown in Fig. 3.14(c) as a function of the optical path difference up to 4.6 cm achieved in the FTS. The signal shows more or less constant modulation of the intensity with increasing optical path difference. It is worthy noting that the maximum intensity varies slowly with an increase in the optical path difference, whereas the minimum stays at an intensity level of 0 independent of the path difference. The variation of the maximum intensities results from the variation of the relative power of the laser modes in time. The decrease (increase) in optical intensity modulation due to the increase (decrease) in the optical power difference between both laser modes results in the decrease (increase) in the generated THz power. Fig. 3.14(d) shows a Fast Fourier Transform (FFT) of the interferogram in Fig. 3.14(c). The FFT shows THz radiation at a single frequency of 896 GHz, which is the same as the difference frequency of the two laser modes recorded with the OSA. The emission

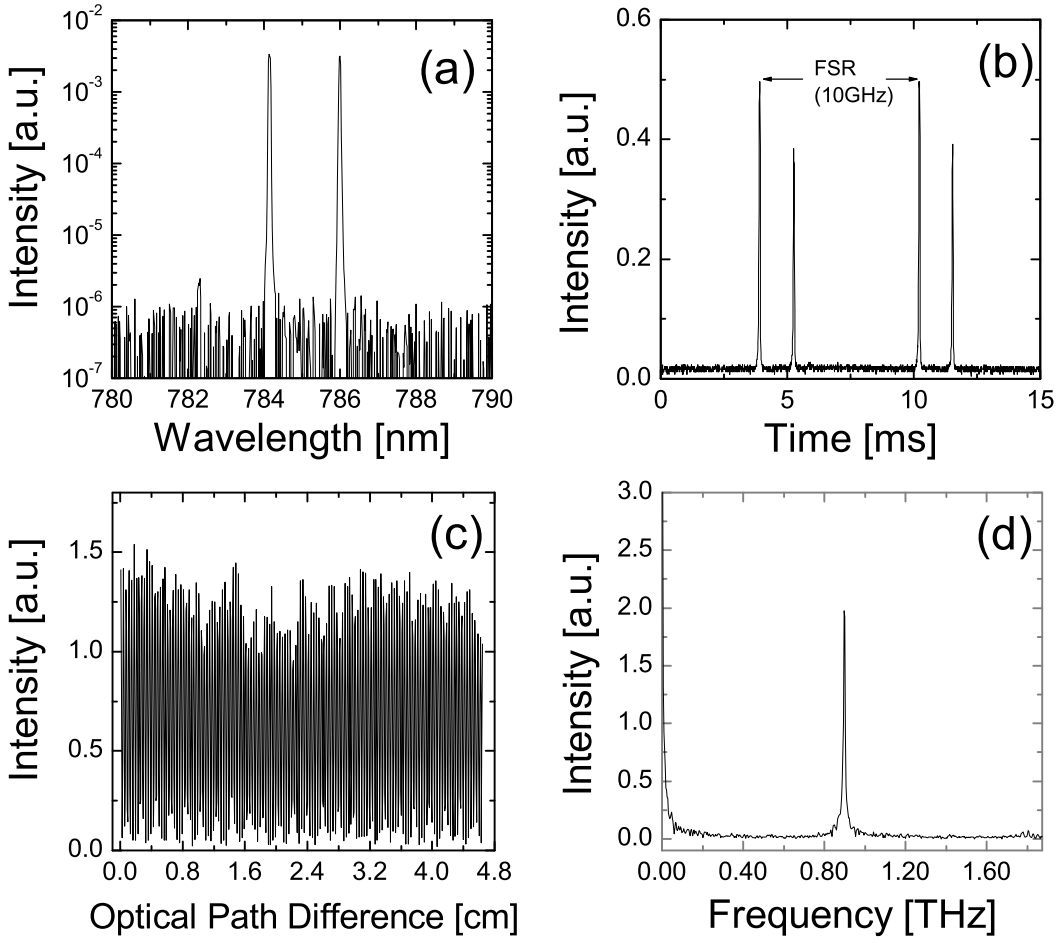

Fig. 3.14: Optical spectra of dual-mode emission with $\Delta\lambda = 1.84\,\text{nm}$ and FFT of correspondingly generated THz radiation. (a) optical spectrum recorded by OSA, (b) Fabry-Perot-Interferometer scan, (c) interferogram of the generated THz radiation measured with FTS, (d) FFT of the interferogram.

of THz radiation with the same frequency as the beat frequency of the laser modes indicates that the THz radiation is generated by the antenna whose photocurrent is modulated at the beat frequency of the laser modes. The linewidth of the THz radiation is measured to be approximately 7 GHz, which is limited by a spectral resolution of 6.5 GHz corresponding to the achieved maximum path difference of 4.6 cm. Therefore, the linewidth of the detected THz radiation cannot be resolved directly.

In comparison, a FFT spectrum of THz radiation generated by another type of dual-mode lasing regime is depicted in Fig. 3.15. An optical spectrum recorded by the OSA shown in Fig. 3.15(a) displays two spectrally filtered laser modes and a weak FWM sideband, as for the case of Fig. 3.14(a). The difference wavelength of the modes amounts to

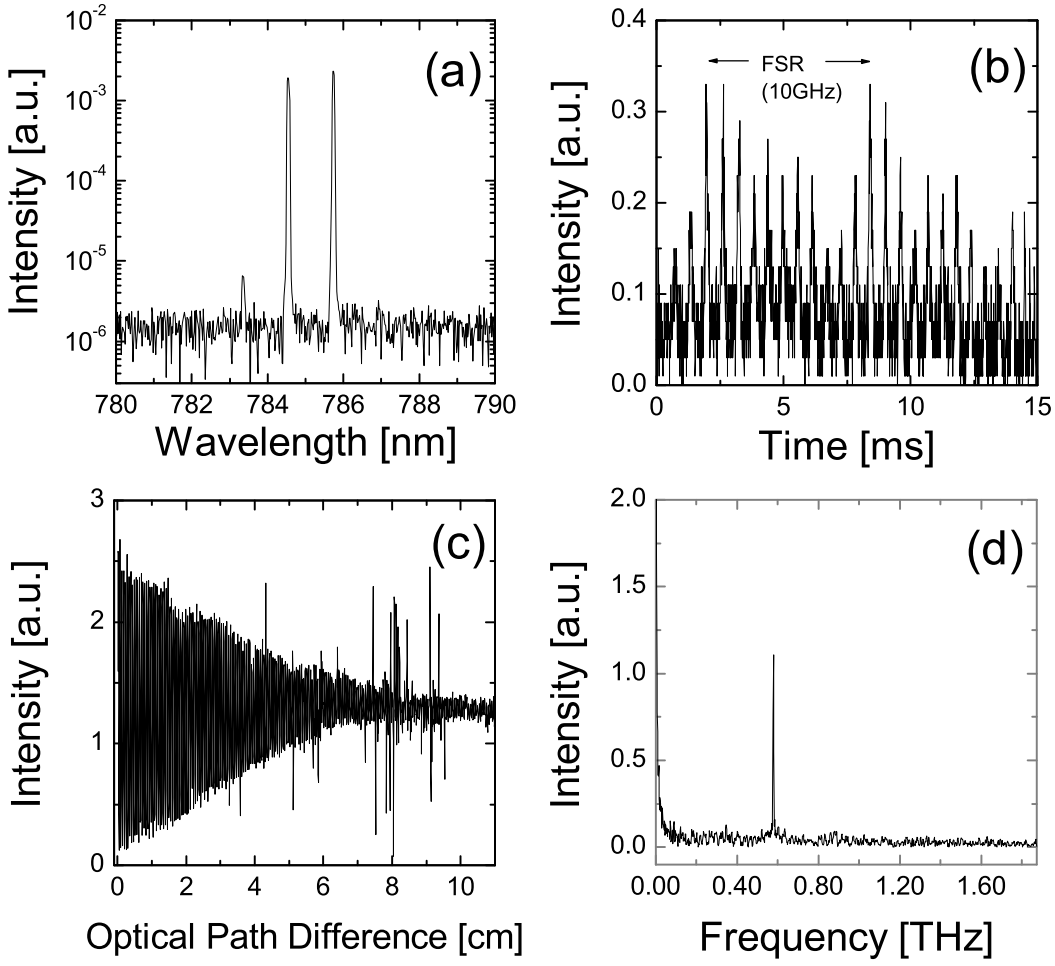

Fig. 3.15: Optical spectra of dual-mode emission with $\Delta\lambda = 1.2\,\text{nm}$ and FFT of correspondingly generated THz radiation. (a) optical spectrum recorded by OSA, (b) Fabry-Perot-Interferometer scan, (c) interferogram of the generated THz radiation measured with FTS, (d) FFT of the interferogram.

1.2 nm which corresponds to the difference frequency of 584 GHz. From the OSA spectrum, it could be supposed that the laser oscillates in the coherent dual-mode regime. However, a high-resolution spectrum recorded simultaneously by the Fabry-Perot interferometer shown in Fig. 3.15(b) exhibits that these spectral peaks in reality contain several external cavity longitudinal modes with a mode spacing of 880 MHz. This optical spectrum shows the semicoherent dual-mode lasing regime in which each of the two main lasing frequencies comprises several external cavity modes[47]. The linewidth of each external cavity mode amounts to 60 MHz. The width of each group of external cavity modes amounts to about 3.4 GHz. FTS measurement shows an interferogram of the generated THz radiation in Fig. 3.15(c). The intensity modulation decreases

symmetrically about an average intensity with increasing optical path difference and approaches the average intensity. The maximum path difference here investigated is up to 11 cm and corresponds to a spectral resolution of 2.7 GHz. The decreasing behavior of the intensity modulation is expected from the fact that the spectral broadening of the THz radiation due to the multiple external cavity modes reduces the coherence length of the radiation. This results in the rapid decrease in the intensity modulation, compared with that in Fig. 3.14(c). The FFT spectrum that is computed from this interferogram shows THz radiation at a single frequency of 578 GHz in Fig. 3.15(d). The THz radiation frequency is in good agreement with the beat frequency of the two main laser modes. The measured linewidth of the radiation amounts to approximately 4 GHz, which can be resolved by the FTS measurement. Furthermore, it is expected that the generated THz radiation should contain several peaks with a frequency spacing of 880 MHz. However, these could not be resolved in the FFT spectrum due to the limited spectral resolution of the FTS.

Although in principle the minimum spectral resolution of the employed FTS is limited to 1.5 GHz by a maximum achievable path difference of 20 cm between the positions of the two interferometer mirrors, the achieved path difference in reality in the present experiment is limited by the mechanical and electrical stabilities of the movable mirror employed in the FTS. Since the linewidth of the FFT-spectrum at 896 GHz is the same as the spectral resolution of the FTS, the linewidth of the detected THz radiation cannot be measured directly. However, the linewidth can be estimated from the obtained interferogram [107]. The coherence length of the radiation can be estimated from the decay of the interferometric intensity of the radiation with an increase in the path difference of the interferometer. The intensity variation as a function of the path difference can be fitted by a damping cosinusoidal function which is described by

$$I(l) = \frac{1}{2} I_0 \left(1 + e^{-(\frac{l}{l_c})} \cos\left(\frac{2\pi}{\lambda} \cdot l\right)\right), \tag{3.14}$$

where l is the path difference of the interferometer, l_c is the coherence length of the radiation, λ is the free-space wavelength of the radiation, and I_0 is the intensity of the interferogram at $l = 0$. The exponential decay term in Eq. (3.14) expresses the decay of the visibility V_{vis} of the interferogram, which is defined as

$$V_{vis}(l) = \frac{I_{max}(l) - I_{min}(l)}{I_{max}(l) + I_{min}(l)}, \tag{3.15}$$

where $I_{max}(l)$ and $I_{min}(l)$ represent the maximum and minimum intensities of the interferogram located nearest at a path difference of l, respectively. By fitting the visibility of the interferogram, the coherence length can be estimated. The obtained

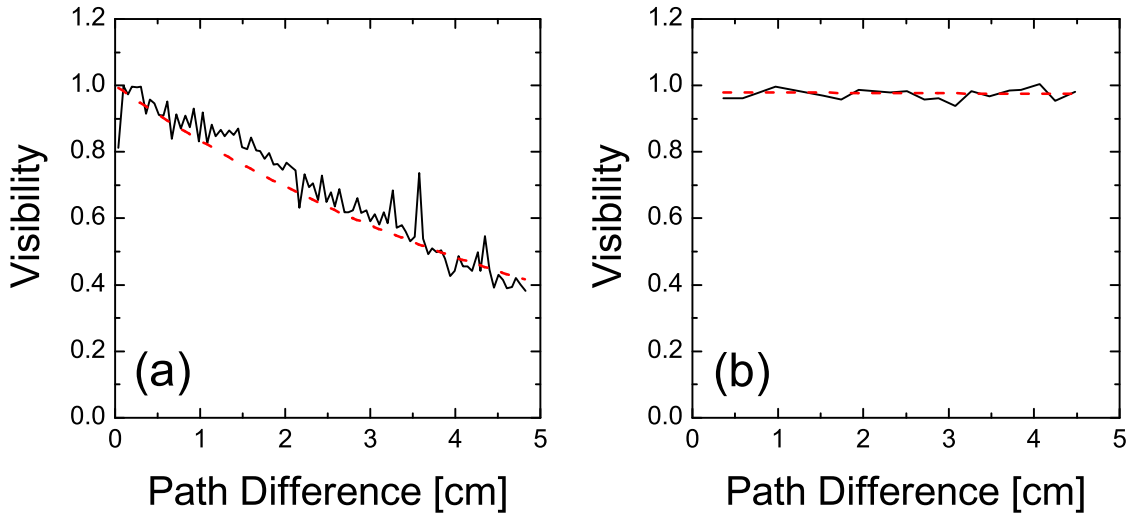

Fig. 3.16: Visibility of the interferograms (a) for 584 GHz and (b) for 896 GHz. The solid lines represent the visibility obtained from the interferogram. The dashed lines represent fits, assuming an exponential decay.

l_c is then related to the coherence time τ_c by $l_c = c\tau_c$, where c is the light velocity in free space. Therefore, the linewidth $\Delta\nu$ of the radiation can be estimated according to $\Delta\nu \simeq \tau_c^{-1}$.

For the radiation at 584 GHz, the coherence length estimated by fitting the visibility of the interferogram in Fig. 3.16(a) amounts to about 5.5 cm. Therefore, the linewidth is about 5.5 GHz, which is in good agreement with the linewidth obtained experimentally. Since each group of the external cavity modes has a width of 3.4 GHz, this indicates that the linewidth of the beat frequency of the two mode groups is smaller than the sum of linewidth of the individual mode group. For the radiation at 896 GHz, the interferogram does not show symmetric variation of the interferometric intensity about an average intensity with increasing path difference. As mentioned above, the maximum interferometric intensity can vary due to the variation of the generated THz radiation power, which results from the variation of the relative optical power of both laser modes. However, it does not affect the coherence length of the generated radiation so that the minimum interferometric intensity stays at the level of 0. Because the interferogram does not show obvious variation of visibility with increasing path difference, the linewidth of the radiation of 896 GHz cannot be definitely determined by Eq. (3.14). However, by fitting the visibility of the interferogram in Fig. 3.16(b), the coherence length of the radiation can be roughly estimated to be larger than about 800 cm. This corresponds to a linewidth of 38 MHz, which is much narrower than that of the laser mode. This result indicates that the linewidth of the generated THz

radiation is narrower that that of each laser mode. Since the linewidth of the THz radiation generated by photomixing is almost the same as the linewidth of the beat frequency of the two laser modes, this result indicates that the linewidth of the beat frequency is also narrower than that of the individual laser modes. The narrowing of the beat frequency is attributed to the common-mode rejection effect for the two laser modes oscillating in the same cavity. A significant part of the frequency fluctuations of the two laser modes is canceled out because the two modes share the same cavity and undergo the same fluctuations. The generated THz radiation is therefore stabler than each laser mode. This is the reason for the generation of THz radiation using a dual-mode SL as an optical source.

Though the photomixing of two optical mode groups which comprise several external cavity modes generates THz radiation with a linewidth of the order of GHz, the generation efficiency of THz radiation is not as high as compared to that in the case of pure dual-mode laser source. For the same injection current, the optical power of the multimode operation is measured to be about 60 % of that of the dual-mode operation. Furthermore, at a constant optical power for both cases, the power of the generated THz radiation for the multimode operation reaches at maximum 20 % of that for the dual-mode operation. Therefore, total generation efficiency of THz radiation for the multimode case is only about 12 % of that for the dual-mode case at a constant injection current of SL. The reduction of the generation efficiency may be induced by an intensity interference among several external cavity modes, which in turn modulates the intensity behavior deviating from a simple harmonic modulation for the dual-mode superposition. Therefore, the time averaged total intensity modulation for the multimode operation is lower than that of the dual-mode operation, so is the power of the generated THz radiation. As a result, the pure dual-mode laser source is desirable for the efficient generation of THz radiation. However, the multimode laser source can also be employed for less stringent generation of THz radiation which may well be used for many applications such as THz imaging.

3.3.5 Frequency Dependence of the Generation of THz Radiation

The antenna converts the current wave oscillating with THz frequency in the photomixer into an electromagnetic wave that propagates in free space with the same frequency. Therefore, the generated THz radiation exhibits characteristics of the antenna. The achievable frequency range of the THz radiation is determined by the bandwidth of the antenna which is the range of frequencies with acceptable antenna performance. In this section, the frequency dependence of the generated THz radia-

tion is investigated at a constant optical power of 21 mW and a constant bias voltage of 18 V. The average optical power incident on the photomixer amounts to 10.5 mW due to the chopping. The difference frequency of the two laser modes is varied from 126 GHz to 1.8 THz. The upper detuning frequency is restricted to 1.8 THz because the solitary laser modes start to oscillate at further detuning. Investigation at still larger frequency range will be shown in section 3.3.7.

Since fluctuations in the optical power and in the power difference between the two laser modes cause fluctuations of the generated THz radiation power, the detected radiation power should be normalized not only to the square of the photocurrent, but also to the normalization factor N_f, in order to avoid effects which cannot be attributed to characteristics of the photomixer and the antenna. However, in the context of this section, the detected THz radiation power is normalized only to the square of the photocurrent. Instead, the theoretical efficiency has been calculated according to Eq. (3.3) including the experimentally determined $N_f = 4P_1P_2/(P_1 + P_2)^2$. This method allows to identify mechanisms responsible for distinguishable behavior of THz radiation as a function of frequency more clearly, which will be discussed later in this section.

The experimentally obtained efficiency and the theoretical data fit are displayed in Fig. 3.17 as a function of the difference frequency of the laser modes. The experimental data (open squares in Fig. 3.17) show a dip at 204 GHz and increase with increasing frequency up to 457 GHz. Thereafter, they decrease at a rate of −6 dB/octave (solid line in Fig. 3.17) with increasing frequency up to about 800 GHz. At higher frequencies greater than 1 THz, the data decreases at a rate approaching −12 dB/octave (dashed line in Fig. 3.17) with increasing frequency, except the values marked by arrows. The theoretically expected values (open circles in Fig. 3.17 according to Eq. (3.3)) depicted for comparison show a behavior decreasing slowly with increasing frequency up to about 400 GHz and thereafter the same decreasing behavior as that of the measured data. The measured data agree well with the theoretically expected values. The decrease in radiation power with increasing frequency is attributed to the photoexcited carrier lifetime and the capacitance of the photomixer. The finite lifetime required for the excited carriers in the photoconductive material to recombine significantly limits the performance of the device as the frequency increases. In addition, the region of the interdigitated electrode fingers possesses a capacitance. Since the photomixer can be described as a device having a modulating conductance with a shunt capacitance due to the interdigitated fingers, the capacitance affects the behavior of the photomixer at the THz frequency range and causes the antenna impedance to short-cut at high frequencies.

From the theoretical fit of the measured data, the carrier lifetime in the LT-GaAs

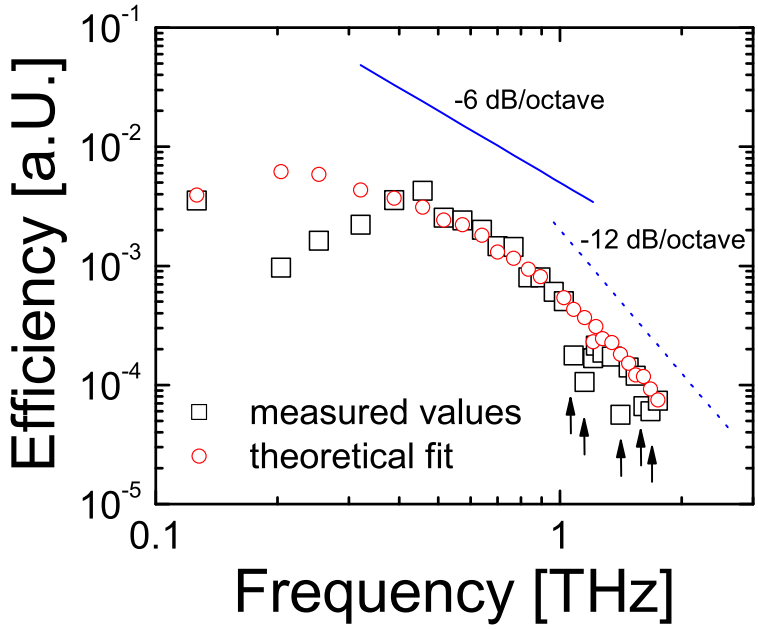

Fig. 3.17: Efficieny of the THz generation depending on THz frequency. Open squares represent measured values and open circles represent values expected by theoretical calculations. The arrows represent absorption lines of water vapor. The solid and dashed lines show the theoretically predicted roll-offs of $-6\,\mathrm{dB/octave}$ and $-12\,\mathrm{dB/octave}$, respectively.

material can be estimated by Eq. (3.3). The resulting carrier lifetime is 350 fs. This value is in good agreement with a value of 430 fs which has been determined by a pump-and-probe measurement [108]. The roll-off in the frequency performance with a rate of $-6\,\mathrm{dB/octave}$ in Fig. 3.17 is due to the carrier lifetime of 350 fs. An additional $\mathrm{R_AC}$ time constant of 195 fs, which is given by $\mathrm{R}_A = 65\,\Omega$ and $\mathrm{C} = 3\,\mathrm{fF}$, limits the frequency performance with a roll-off rate of $-6\,\mathrm{dB/octave}$. Thus, the high-frequency roll-off with the rate of $-12\,\mathrm{dB/octave}$ in Fig. 3.17 is due to the combination of the carrier lifetime and the $\mathrm{R_AC}$ time constant. The theoretical 3 dB roll-off frequencies due to the carrier lifetime of 350 fs and the $\mathrm{R_AC}$ time constant of 195 fs are calculated to be 455 GHz, and 816 GHz, respectively. These values are in good agreement with the values of 457 GHz and 835 GHz which are estimated by comparing the measured data with the displayed roll-off curves in Fig. 3.17.

It is noteworthy that the different frequency behavior of the measured values compared to the theoretically expected behavior can be caused by several mechanisms. Four different mechanisms can be identified. Firstly, the difference of the behavior shown at frequencies below 400 GHz may be induced by the antenna characteristics. Since

the log-periodic toothed antenna shows periodic resonance behavior, there are low and high radiation efficiencies depending on the THz frequency. On the contrary, the theory does not contain such periodic characteristics. Therefore, the radiation power in the periodic resonant range is expected to deviate from the theoretical values. Secondly, the difference at the frequency of 457 GHz comes probably from the effect caused by the used Si lens attached to the backside of the antenna chip. A measurement using another lens with a different diameter did not show the same effect [87]. Since the lens acts as an aperture, diffraction of higher frequencies at a given aperture size is smaller than of lower frequencies. Smaller diffraction at the frequency of 457 GHz induces more effective coupling of the radiation into the detector by parabolic mirrors than larger diffraction. This higher coupling gives rise to more detected power. The third mechanism is responsible for the clear differences indicated by arrows at frequencies 1.08, 1.148, 1.41, 1.606, and 1.674 THz. They are identified as absorption lines of water vapor in the atmosphere [95]. The measured values at 1.206, 1.226 and 1.274 THz show smaller values than the theoretical values. They belong to the absorption lines of water vapor. The absorption by water molecules will be reconsidered in the spectroscopic investigations in section 4.2. The last mechanism is induced by a power difference of the incident optical modes onto the antenna. This can be easily identified from the theoretical curve in Fig. 3.17 where the values for the efficiency at 126 GHz and 1.206 THz are clearly lower than adjacent values. For the discussion of the measured value, the values around 126 GHz are not considered due to the resonance character of the antenna. The value at 1.206 THz shows also a lower value than two adjacent values, except for the absorption lines. Therefore, interpreting the measured values alone has to be performed with care. A joint effort of experiment and modelling is necessary.

3.3.6 THz Polarization Properties by Emission from Log-Periodic Toothed Antenna

One of the parameters which characterize an electromagnetic wave is the polarization of the wave. The THz radiation emerging from the antenna can thus be characterized by its polarization, which also describes the antenna characteristics. The polarization of the generated THz radiation is related to the geometry of the used antenna. This is due to the fact that the antenna geometry determines the directions of the current oscillation which in turn determines the polarization of the generated THz radiation field. As shown in section 3.1.4.2, the log-periodic toothed antenna has periodic teeth-geometry, which in turn depends on the desired operation frequency. It is expected from this periodicity that the generated THz radiation should reveal polarization behavior corresponding to the resonant tooth. Therefore, the polarization behavior of the THz

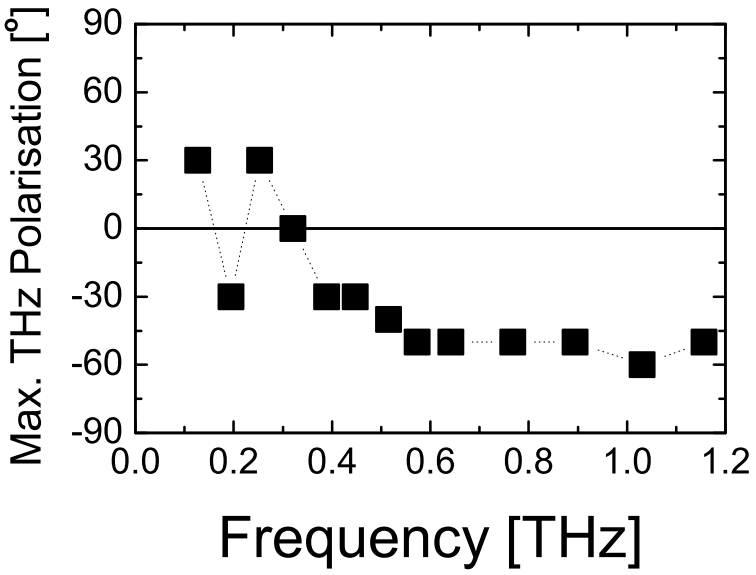

Fig. 3.18: Direction of the maximum polarization of the generated THz radiation as a function of the THz frequency. The reference polarization of 0° was chosen as the direction perpendicular to the fingers. The positive (negative) values represent the clockwise (counterclockwise) rotation about 0°. The dotted line is a guide to the eye.

radiation depending on the THz frequency will be investigated in this section.

In order to measure the polarization of THz radiation experimentally, a wire-grid THz polarizer with wire thickness of 5 μm and wire separation of 12.5 μm was inserted in the THz beam path and placed directly in front of the bolometer. Since the bolometer is insensitive to polarization of incident radiation, the influence of the bolometer on polarization analysis can be ruled out. In order to give a reference direction of the polarization, the polarization perpendicular to the finger (i.e., interdigitated electrodes) direction of the photomixer was defined as the zero degree (0°) polarization, as shown in Fig. 3.8(b). In addition, the rotation of the polarization clockwise (or counterclockwise) about 0° was defined as positive (or negative) polarization angles. The THz power transmitted through the polarizer was measured as a function of the polarizer angle with respect to the direction of the finger of the photomixer. The measurement was performed under constant optical power of 21 mW across the frequency range between 100 GHz and 1.2 THz.

In Fig. 3.18, the maximum polarization direction of THz radiation emitting from the log-periodic toothed antenna is depicted as a function of the THz frequency. The measured maximum THz polarization direction shows an alternating behavior between

+30° and −30° in the frequency range below 390 GHz. Above 390 GHz, the polarization approaches −50° with increasing frequency and remains nearly constant at about −50° above 570 GHz. In the range below 390 GHz, the resonant antenna teeth are responsible for the generation of the corresponding THz radiation. The change in the polarization direction with frequency below 390 GHz is attributed to the antenna geometry in which the THz radiation is emitted from the portion of the antenna teeth resonant to the frequency. As explained in section 3.1.4.2, the log-periodic toothed antenna exhibits a bow-tie type geometry with teeth alternating their direction periodically. The directions of the teeth are symmetrical about the centerline of the bow-tie structure. The current flowing along the resonant tooth contributes to the emission of radiation so that the polarization of the generated radiation is directed along the corresponding tooth edge. Since the resonant portion of the antenna geometry depends on the frequency, the emitted radiation shows corresponding changes in the polarization behavior as the radiation frequency changes. The maximum polarization directions below 400 GHz depicted in Fig. 3.18 correspond to the frequencies of 127, 195, 253, 321 and 389 GHz. The theoretically expected resonant THz frequencies for this antenna, which are listed in table 3.1, are 114, 164, 228 and 367 GHz with alternating polarization approximately between +25° for 114 GHz and −25° for 367 GHz. The largest resonance frequency is 367 GHz corresponding to the smallest antenna tooth. The comparison of the measured values (except 321 GHz) with the theoretical values reveals that the measured values lie near the resonant frequencies and exhibit the corresponding polarization direction. For the frequency of 321 GHz, which lies between two neighboring resonant frequencies, the polarization is perpendicular (0°) to the finger direction. The 0° polarization for this frequency is also expected from the geometrical structure of the antenna. This frequency lies between two theoretical resonant frequencies of 228 GHz and 367 GHz. Since both neighboring antenna teeth are contributing to the generation of radiation at 321 GHz and they are geometrically located at symmetrical angular position about the perpendicular line to the finger direction, the total contribution gives rise to the resultant polarization pointing to the direction of 0°. Above 390 GHz, the contribution of the smallest antenna tooth which is responsible for the THz radiation with the largest resonance frequency decreases with increasing frequency. The THz emission is gradually generated by the innermost portion of the antenna structure which behaves as a bow-tie antenna. The bow-tie antenna emits radiation of constant polarization in the direction which is determined by the bow-tie angle [61]. Therefore, as the frequency increases above 350 GHz, the polarization direction increases from −30° dominated by the smallest tooth to that of the bow-tie that has a constant direction of approximately −50°.

In addition to the measured THz polarization which shows the theoretically expected directions depending on the difference frequency, the polarization state can be fully

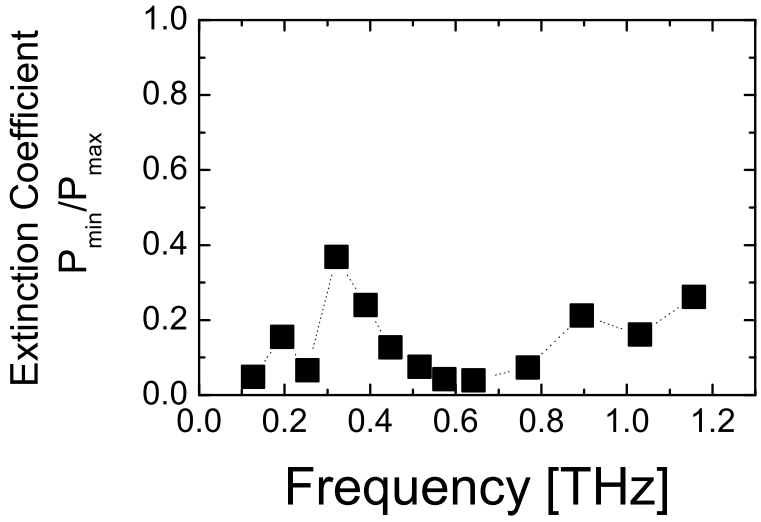

Fig. 3.19: Extinction coefficient P_{min}/P_{max} of polarization of the generated THz radiation as a function of the THz frequency. A value of 0 corresponds to a perfect linear polarization state and a value of 1 corresponds to a perfect circular polarization state. The dotted line is for visual aid.

determined in detail by calculating the ratio of electric field intensities between minimum and maximum polarization direction. This information can be extracted by the extinction coefficient defined as the ratio between the minimum and maximum powers transmitted through the polarizer under orthogonal orientations. Fig. 3.19 shows the investigated extinction coefficient P_{min}/P_{max} of polarization of the generated THz radiation as a function of the THz frequency. A value of 0 corresponds to a perfect linear polarization state and a value of 1 corresponds to a perfect circular polarization or unpolarized state[1]. The log-periodic antenna emits linearly polarized radiation at the resonant frequencies with an extinction coefficient of about 0.05. This can easily be seen in Fig. 3.19 for 127 GHz and 253 GHz. This is expected because most of the current flows on the corresponding tooth at resonance so that the emitted radiation is linearly polarized parallel to the tooth edge. For 195, 321, and 389 GHz, the polarizations are elliptical. If the frequency deviates from one resonance frequency, the next resonant portion of the antenna also contributes to the generation of the radiation with different polarization direction and phase. The emitted THz radiation then exhibits elliptical polarization. The more the contribution of the neighboring portion increases, the more the radiation becomes elliptical. This is apparent at 321 GHz with an ex-

[1]From the optics point-of-view, it should be noted that a complete analysis of a polarization state requires a combination of a $\lambda/4$-plate and a linear polarizer. With respect to antenna and emitted radiation, we refer to Ref. [89] and discuss only linear and elliptical polarization states.

tinction coefficient of 0.37. These extinction coefficients are in good agreement with the results reported in Ref. [89]. Beyond the largest resonance frequency, the contribution of the bow-tie structure to the generation of radiation becomes dominant with increasing frequency. Since the radiation generated by the bow-tie antenna is in general linearly polarized, the THz radiation becomes more linearly polarized. This explains the behavior of the polarization state around 600 GHz where the extinction coefficient reaches about 0.04. At frequencies above 895 GHz, the radiation becomes elliptically polarized again with an extinction coefficient of about 0.2. This indicates that another portion of the antenna contributes to the generation of the radiation. This may be attributed to the contribution of the finger structure of the photomixer. The radiation is directly generated by the current transients in the LT-GaAs material between the fingers in a direction perpendicular to the finger direction. This causes an additional polarization perpendicular to the finger direction and the extinction coefficient rises with increasing frequency.

As summarized in Figs. 3.18 and 3.19, the THz radiation emitted by the log-periodic toothed antenna used in the present experiment shows an alternating linear polarization state at resonance frequencies and elliptical polarization during the transition of the resonance. Above the largest resonance frequency, the radiation is linearly polarized in a constant direction due to the influence of the bow-tie structure. With further increasing frequency, the polarization becomes elliptical maintaining the maximum polarization direction. In addition, it should be noted that the alternating behavior of the polarization direction depending on the frequency is caused by mechanisms which differ from those causing the alternating power in the previous section. The former is caused by the geometrically alternating direction of the resonant teeth depending on frequency, whereas the latter is caused by an alternating impedance of the antenna depending on frequency. As a remark, these polarization characteristics of the antenna are also important for the measurement of the THz radiation using a photoconductive method in which an antenna is used as a detector of the radiation. In this detection method, the polarization of the incoming radiation must match the polarization of the detecting antenna [109]. Otherwise, the detection efficiency decreases with increasing polarization mismatch.

3.3.7 THz Generation Using Double-Littrow-Configuration

As shown in the previous sections, the achievable detuning frequency of the dual-mode emission of the laser was restricted to about 1.8 THz. This restriction was not caused by the geometry of the used configuration, but rather by the residual reflectivity of the laser facet. If the difference frequency of the two modes selected by the external mirrors

increases towards the edge of the spectral gain, the laser's own resonant modes cannot be sufficiently suppressed so that, besides the external modes, the laser's own modes oscillate simultaneously. These unwanted laser modes can be effectively suppressed by applying an antireflection coating on one of the laser facets. It is shown in section 2.2.4 that the detuning frequency can be extended up to 10 THz using a laser with antireflection coating in a Double-Littrow-Configuration.

In this section, a tunable dual-mode SL using the Double-Littrow-Configuration will be employed to generate THz radiation. Because the characteristics of the employed log-periodic toothed antenna has been investigated in detail in the previous sections, the investigation in the present section is concentrated on generating THz radiation and extending the frequency range of THz emission. The investigation will be performed using the 2λ-ECSL with the Double-Littrow-Configuration as an optical light source instead of the 2λ-ECSL with the Double-Littman-Configuration of Fig. 3.7. The laser with a central wavelength of 825 nm was driven by a constant injection current of 175 mA ($3.5\mathrm{I_{th}}$) at room temperature. The external cavity has a length of about 2.5 cm. It corresponds to a longitudinal mode spacing of 6 GHz. In order to align the optical polarization to be perpendicular to the direction of the finger of the photomixer, a $\lambda/2$-plate and a polarizer are placed in the beam. The total optical power of 15 mW is chosen to prevent possible burnout of the antenna at higher applied bias voltages. The laser beam is then chopped with the frequency of 135 Hz for detection using a lock-in method and focused on the photomixer. Hence, the average optical power incident on the photomixer is 7.5 mW due to chopping. The generated THz radiation is coupled into free space via a hyperhemispherical Si lens. The THz radiation is then collimated by an off-axis parabolic mirror with a focal length of 4.6 cm and focused by an off-axis parabolic mirror with a focal length of 10 cm into a Si bolometer cooled at 4.2 K. The optical dual-mode operation of the SL is monitored by an OSA and a Fabry-Perot interferometer. The bolometer signal is recorded via a lock-in amplifier.

First, in order to confirm the THz generation by photomixing, the generated THz power is investigated as a function of applied bias voltages. The detuning frequency of the laser dual-mode with a constant optical power of 15 mW is held at 372 GHz. The bias voltage is varied from 0 to 20 V. The THz output power is again specified by the detected lock-in signal. The result is shown in Fig. 3.20(a). The THz power (i.e., lock-in signal) increases quadratically with increasing bias voltage up to 5 V and superquadratically at higher bias. This feature of the THz radiation power as a function of bias was already shown in section 3.3.1. The solid and dashed line in Fig. 3.20(a) represent the quadratic and superquadratic fit of the measured values, respectively. At 20 V, the antenna exhibits a slight saturation behavior.

Secondly, the THz output power is investigated as a function of the detuning frequency

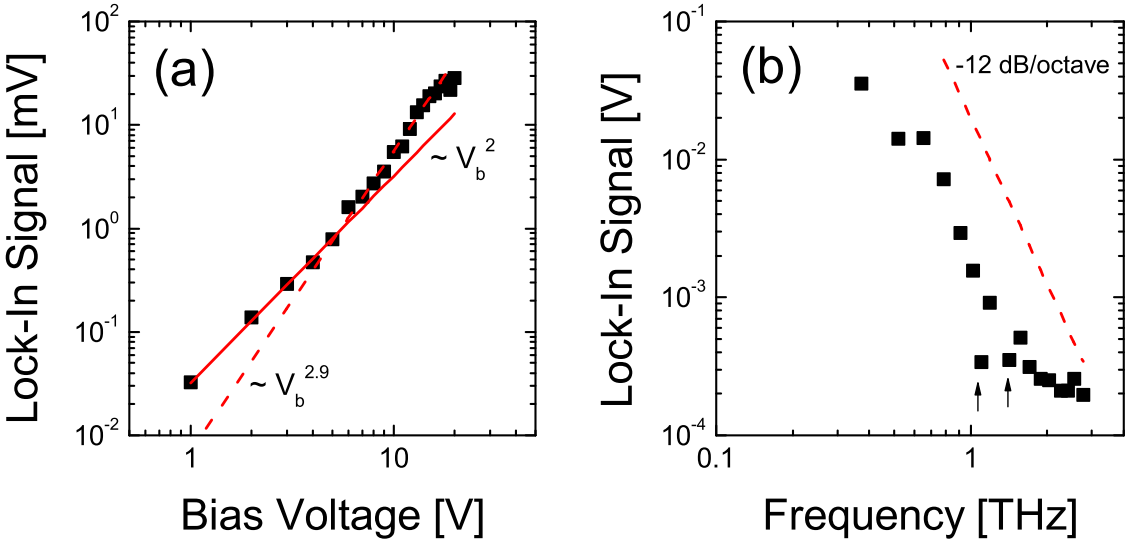

Fig. 3.20: Lock-In signal (a) as a function of applied bias voltage and (b) as a function of the difference frequency of the dual-mode laser. The solid line and the dashed line in (a) represent the quadratic and superquadratic fit of the measured values respectively. The dashed line in (b) represents a $-12\,\mathrm{dB/octave}$ roll-off of THz power. The arrows represent absorption lines of water vapor.

of the two modes at a constant optical power of 15 mW. The applied bias voltage is held constant at 20 V. The detuning frequency of the two laser modes was varied from 372 GHz to 2.77 THz. The THz power is plotted in Fig. 3.20(b) as a function of the detuning frequency of the two laser modes. As already shown in section 3.3.5, the THz power decreases with increasing frequency and shows a roll-off of $-12\,\mathrm{dB}$ per octave at high frequencies up to 1.8 THz. For visual aid, the $-12\,\mathrm{dB/octave}$ roll-off of THz power is represented by a dashed line in Fig. 3.20(b). However, contrary to the behavior below 1.8 THz, the THz power decreases only gradually above 1.8 THz and approaches the noise level at frequencies above 2.77 THz. The signal-to-noise ratio at 2.77 THz amounts to 1.5:1. The relatively low THz powers at frequencies of 1.1 THz and 1.4 THz are again due to the absorption by water vapor in the atmosphere.

The maximum lock-in signal obtained in these investigations amounts to about 35 mV at a frequency of 372 GHz with a signal-to-noise ratio of 271:1. Because this signal is amplified 200-fold by a preamplifier included in the bolometer, the signal before amplication amounts to 175 μV. Assuming a bolometer sensitivity of $2.39 \times 10^5\,\mathrm{VW^{-1}}$ for the conversion of the lock-in signal to the THz output power, the THz power amounts to about 0.73 nW. Consequently, the conversion efficiency of the incident optical power (i.e., 7.5 mW) to the generated THz radiation power at the given bias voltage is 1×10^{-7}.

This conversion efficiency is in the order of magnitude 3 smaller than the expected value of about 10^{-4} which would be the ratio for the expected THz radiation power of about $1\,\mu$W calculated by inserting the measured photocurrent into Eq.(3.4). This deviation of the conversion efficiency can arise from several reasons. The main reason is the impedance mismatch between the photomixer and the antenna. While the impedance of the antenna amounts to $65\,\Omega$, the photomixer exhibits an impedance of $114\,\mathrm{k}\Omega$ at a bias voltage of 20 V and for an optical incident power of 7.5 mW which induces a photocurrent of $176\,\mu$A. Due to the impedance difference, the current wave is reflected at the boundary between the photomixer and the antenna with a reflection coefficient $R_{P,A}$ given by $R_{P,A} = (Z_P - Z_A)/(Z_P + Z_A)$, where Z_P and Z_A denote impedances of the photomixer and the antenna, respectively. Therefore, only a small part of the available power generated in the photomixer can be transmitted to the antenna. The ratio R_T of the transmitted power to the available power can be obtained by $R_T = (1 - R_{P,A}^2)$ and the resulting R_T amounts to 0.002. If this R_T is taken into account, the expected conversion efficiency reduces from 10^{-4} to 2×10^{-7}. This value is in good agreement with the achieved value. As further possible reasons for low conversion efficiency, following factors can be considered. As discussed in section 3.3.1, the photocurrent at the given bias voltage may have a DC component due to the increase in carrier lifetime and the generation of carriers with long lifetime in the substrate. These carriers do not contribute to the generation of the THz wave. Therefore, the measured value can be lower than the calculated value. Another reducing factor might be the emission characteristics of the antenna. As shown in Fig. 3.17, the generation efficiency below 390 GHz is lower than the theoretically expected values. Though the discussed frequency of 372 GHz lies near 390 GHz such that the generation efficiency difference between 372 and 390 GHz might not be significantly large, the investigated frequency lies in the range of the lower generation efficiency. Therefore, the effect of the generation characteristics of the antenna must be taken into consideration for the explanation of the low conversion efficiency. Furthermore, either the absorption of the radiation by free carriers generated in the GaAs substrate, by the substrate itself, and by the employed Si lens, or the reflection of the radiation at the boundary between the Si lens and air also lowers the radiation coupling out of the antenna chip. Furthermore, the measured lower power can also arise due to a low coupling efficiency of the generated THz radiation to the bolometer, which is sensitive to misalignment of the guiding conditions such as parabolic mirrors and Si lens. In addition, reductions may be induced by a power difference between the laser modes, which in turn causes a lower generation of the THz radiation. Finally, the device-lifetime of the antenna may play a significant role. With increasing exposure time with laser light, the antenna performance has gradually degraded on a long term time scale resulting in lower generation efficiency. Nevertheless, the THz radiation power achieved in the context of the present work is

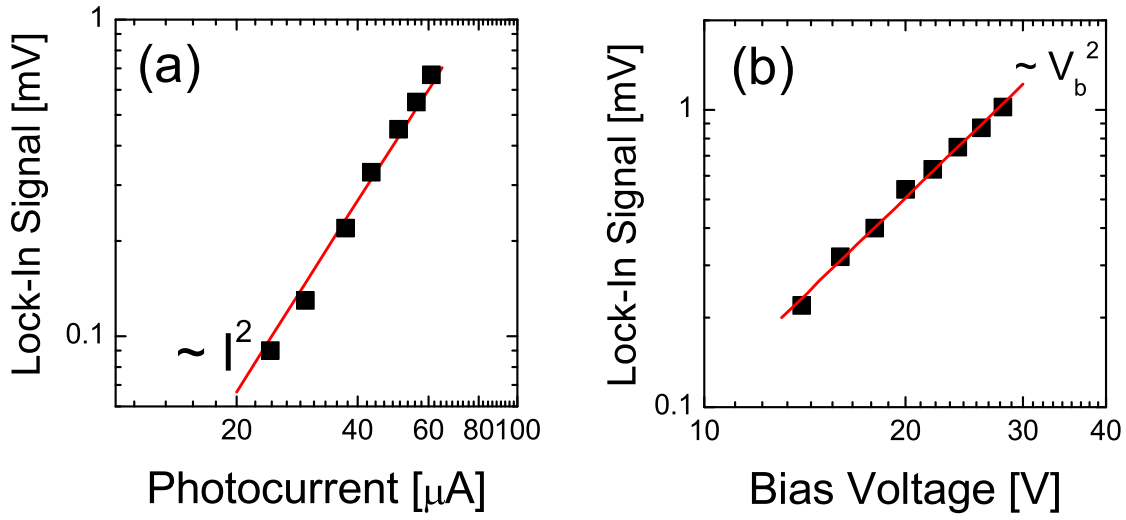

Fig. 3.21: The generated THz radiation with a frequency of 564 GHz as (a) a function of photocurrent and (b) a function of the bias voltage. The solid lines represent quadratic fit.

high enough to be applied for spectroscopic investigation or THz imaging.

3.3.8 THz Radiation from the Dipole Antenna

Broadband antennas such as spiral, bow-tie or log-periodic antennas are designed to emit radiation over a large frequency range. However, for applications which do not require broad bandwidth, it may be advantageous to employ resonant antennas such as dipole antennas. This class of antennas enhances the output power due to higher radiation resistance than frequency-independent antennas. In this section, the radiation characteristics of an H-shaped dipole antenna (H-dipole antenna) has been investigated. The HL7851G SL in the Double-Littman-configuration is driven at a constant injection current of 185 mA in the whole investigation. The output power amounts to about 34 mW. The Si lens is not employed in these measurements, therefore, the signal detected by the bolometer is weaker than in the previous investigations. Thus, the bolometer signal is amplified by the preamplifier with a gain of 1000 instead of 200.

First, the dual-mode laser light with a difference frequency of 564 GHz is chopped with a frequency of 74 Hz and focussed on the gap of the H-dipole antenna. The bias voltage is varied while the incident optical power is kept constant. The detected THz radiation power is depicted in Fig. 3.21 as a function of photocurrent and applied bias voltage. As shown in Fig. 3.21(a), the THz radiation power increases quadratically with the

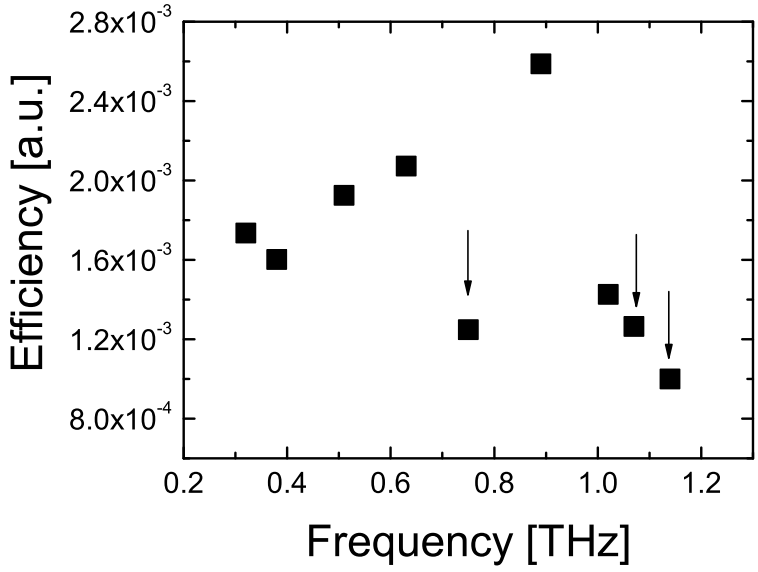

Fig. 3.22: Efficiency of the THz generation of a H-dipole antenna depending on THz frequency. The arrows represent regimes of absorption lines of water vapor.

photocurrent over the whole photocurrent range. The relation between the generated radiation power and the bias voltage also shows a quadratic relation. This is shown in Fig. 3.21(b). The solid lines in Fig. 3.21 represent quadratic fits of the experimental points considered. These quadratic relations are expected by the photomixing theory. Thus, it is verified that the detected radiation is generated by photomixing of the two laser modes at the photomixer. It is interesting to note that the generation characteristics in this dipole antenna shows quadratic features between the THz radiation power and the bias over the entire bias voltage, which is not the case for the log-periodic antenna, where the relation shows a superquadratic feature at high bias voltage (see Fig. 3.11). This may be due to the smaller electric field in the gap of the H-dipole antenna than in the log-periodic antenna at applied bias voltages. The superquadratic relation in Fig. 3.11 begins above a bias of 6 V, which corresponds to an electric field of approximately $6 \times 10^4\,\mathrm{Vcm}^{-1}$ in a 1 μm gap. Since the gap size of the H-dipole antenna amounts to 5 μm, the electric field in the gap amounts to approximately $6 \times 10^4\,\mathrm{Vcm}^{-1}$ only at a bias of 30 V. This field strength lies in the region of the investigated voltages. Therefore, the relation between the THz radiation power and the bias for the H-dipole may show the quadratic feature over the whole investigated bias range up to 30 V. The signal-to-noise ratio amounts to about 8:1. The low signal-to-noise ratio is mainly due to the weak coupling of the THz radiation into free space and into the bolometer.

In order to characterize the frequency dependence of the generated THz radiation, the difference frequency of the two laser modes is varied in the range between 300 GHz and

1.2 THz. The antenna is biased at 28 V. To filter out the influence of optical power fluctuations, the detected signal is normalized to the square of the photocurrent, which gives the generation efficiency of THz radiation depending on the difference frequency of the two laser modes. Fig. 3.22 displays the efficiency as a function of frequency. The efficiency increases with the frequency up to 890 GHz. At higher frequencies, the efficiency decreases with the frequency. The low efficiencies at 0.75, 1.07 and 1.14 THz marked by arrows are due to the absorption of the radiation by water vapor. The emission characteristics show a resonant behavior with a maximum efficiency at 890 GHz. Since the dipole length of the antenna amounts to 70 μm, the resonance frequency calculated analytically from the geometrical length of the half-wavelength dipole lies at 810 GHz. This is in good agreement with the frequency of the maximum efficiency shown in Fig. 3.22. An ideal dipole antenna would have a narrow bandwidth. However, the experimental data shows a relatively broad frequency feature below the maximum frequency and a steep decrease above the maximum. The broad feature may be explained by two possible reasons. One reason may be the finite dipole-strip width of about 4 μm. The dipole antenna with the thicker strip line has a wider bandwidth than the antenna with the thinner strip line [61]. Another possibility is that the broad bandwidth can be interpreted as a low quality factor (Q value) of the antenna induced by the ohmic loss in the antenna [110]. The strong decrease above 890 GHz may be attributed to the roll-off due to the carrier lifetime as well as additional absorption by water vapor.

Further experimental characterization such as FTS measurement or polarization of THz radiation generated from the dipole antenna could not be performed in the present investigation due to degradation of the photomixer caused by thermal failure.

3.4 Summary

In this chapter, a technique to generate frequency-tunable CW THz radiation has been presented. This was based on photomixing (optical heterodyne conversion) of two frequency-tunable, infrared laser modes on photoconductive antennas. Frequency-tunable 2λ-ECSLs which have been developed in chapter 2 are employed as optical laser sources. The tunability of the THz radiation frequency can be achieved by tuning the difference frequency of the two laser modes. The generated THz radiation is detected using a Si bolometer operating at liquid helium temperature.

Investigations of the THz generation using log-periodic toothed antenna confirm quadratic dependence of the THz radiation on optical powers, which is predicted by photomixing theory. In addition, photomixing theory also predicts quadratic dependence

of THz radiation on applied bias voltages. The experimental results shows that the THz radiation depends on the bias voltages quadratically at low bias and superquadratically at high bias. The superquadratic dependence is due to a superlinear increase in photocurrents at high bias, which is attributed to an increase in carrier lifetime. However, the THz radiation does not exhibit quadratic dependence on photocurrents at high bias because the DC component increases in photocurrents at high bias. It is supposed that this is attributed to an increase in carrier lifetime and a contribution of photocarriers with a long lifetime of nanoseconds generated in the GaAs substrate. The generated THz radiation is temporally stable over several tens of minutes and the stability of the THz radiation depends on the stability of the optical source. This temporal stability allows spectral characterization of the generated THz radiation by FTS measurements. The FTS results confirm stable THz radiation with a frequency corresponding to the difference frequency of the two incident laser modes. The estimated linewidth of the THz radiation at a frequency of 896 GHz is about 38 MHz and is narrower than that of the optical modes due to the common-mode rejection effect of the laser modes in dual resonator cavities. The THz radiation exhibits broadband performance, which is characterized by characteristics of the employed antenna. The operating bandwidth is limited to about 3 THz by the carrier lifetime and capacitance of the photoconductive antenna. The polarization of THz radiation in dependence on the difference frequency follows characteristics of the log-periodic toothed antenna and exhibits nearly linear polarization whose orientation depends on the frequency. The achieved maximum THz output power at an incident optical power of 7.5 mW amounts to about 0.7 nW with a conversion efficiency of 10^{-7}. This low conversion efficiency is mainly attributed to the low quantum efficiency of the photomixer and the impedance mismatch between photomixer and antenna. THz radiation generated by the H-dipole antenna also shows predicted quadratic dependence on optical power and bias voltages. Furthermore, it exhibits a resonance behavior, whose resonance frequency is given by the geometric dimension of the dipole. The results achieved in the present chapter reveal that the THz radiation source realized in the context of the present work is a promising source for THz application. In the next chapter, the realized THz radiation source will be used in spectroscopic applications comprising THz transmission studies of several materials and absorption spectra of HCl and H_2O molecules.

Chapter 4

Spectroscopic Application of THz Radiation

Potential applications of the THz radiation lie in nondestructive detection of concealed materials, chemical elements, and imaging of biological systems. These applications are based on interactions of THz radiation with material. Many materials have characteristic THz spectra which can be used as fingerprints of the materials. Spectroscopic examination of such materials with THz radiation enables their identification. Moreover, THz radiation is transmitted through most non-metallic and non-polar materials which are used as packaging and containing mediums. Therefore, THz radiation has potential to be applied for security screening.

In this chapter, the frequency-tunable CW THz radiation source developed in the context of the present work has been applied to study the spectral transmission of THz radiation through various materials which are opaque to visible light and, in addition, to identify absorption spectra of hydrochloric acid (HCl) and water (H_2O) molecules.

4.1 Transmission of THz Radiation

For spectroscopic transmission studies of THz radiation through various test samples, a THz radiation source developed in chapter 3 has been employed in the experiment. A schematic of the transmission measurement is displayed in Fig. 4.1. THz radiation is generated by photomixing of two laser modes emitted from the 2λ-ECSL with the Double-Littman-configuration. The laser (HL7851G) is driven at a constant current of 180 mA. The optical output power at dual-mode operation amounts to about 24 mW. The log-periodic antenna is employed as a THz wave emitter, which is biased at 15 V. The generated THz radiation is coupled out through a Si lens into free space and collimated by a parabolic mirror. After a propagation distance of 14 cm, the collimated THz radiation is then focused by another parabolic mirror into a bolometer. Test samples are positioned in the path of THz radiation between the two parabolic mirrors.

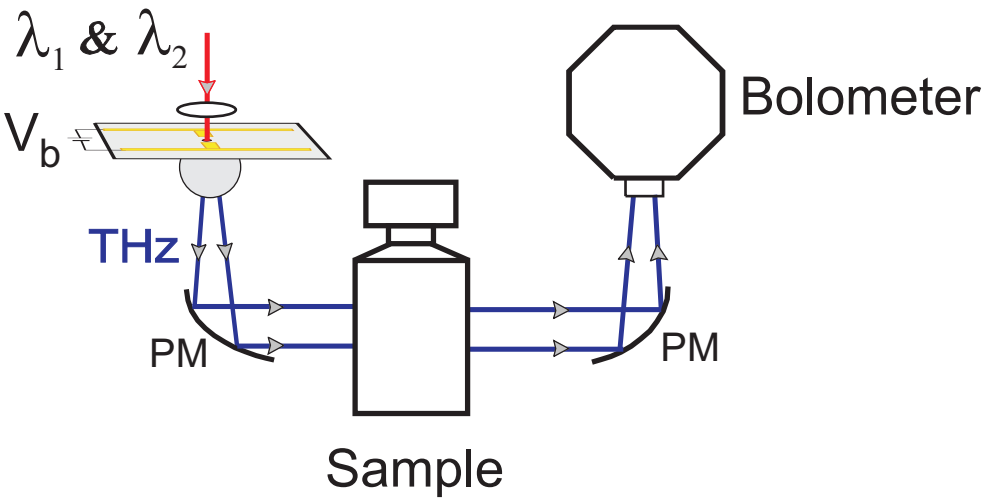

Fig. 4.1: Schematic of the measurement for the transmission of the THz radiation through a sample. A test material or a plastic bottle containing a gas sample is placed between two parabolic mirrors (PM) in the path of the THz radiation. In the top left corner the THz generating antenna is depicted.

material	PE	Teflon	PP	paper	cotton	wood	glass
thickness [mm]	2	1	2.1	0.1	0.5	2.9	0.8

Tab. 4.1: Materials investigated for THz transmission.

First, transmissions of THz radiation through various materials with different thickness have been investigated as a function of frequency between 200 GHz and 1 THz. The investigated materials with individual thickness are listed in table 4.1. These materials are generally used as concealing barriers such as packages, clothes, or containers for chemicals. Thus, the investigation of the transmission properties of THz radiation through various materials reveals the applicability of the THz radiation for screening substances such as chemicals and drugs concealed with such materials.

The materials are inserted in the path of the THz radiation and positioned between two parabolic mirrors as shown in Fig. 4.1. As a reference signal, the THz radiation power propagating through free space along the same path by removing material is measured immediately after each measurement of radiation transmitted through materials. The transmitted radiation power is normalized to that of the free space propagation. The transmission is defined by $P_m(\nu)/P_{fs}(\nu)$ where $P_m(\nu)$ and $P_{fs}(\nu)$ are measured THz radiation powers propagated through materials and free space at a frequency of ν, respectively. This ratio gives the attenuation of the THz radiation through the ma-

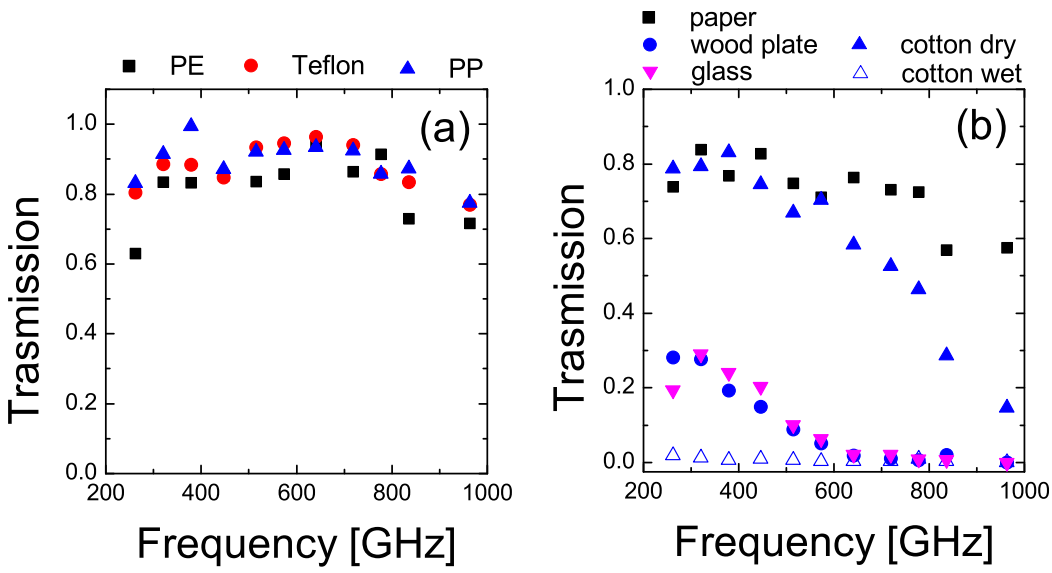

Fig. 4.2: Transmission of THz radiation through various material as a function of frequency. The transmitted THz radiation power is normalized to THz radiation power transmitted through free space. Tested materials are (a): PE (2 mm), Teflon (1 mm), PP (2 mm), (b): paper (0.1 mm), cotton dry (0.5 mm), cotton wet (0.5 mm), wood plate (2.9 mm), and glass (0.8 mm).

terials. The value 1 and 0 of the transmission represent complete transmission and attenuation, respectively. This normalization eliminates influences such as absorption by elements/molecules existing in free space and frequency-dependent THz generation efficiencies of the employed antenna. The immediate measurement of the reference signal minimizes the influence of temporal fluctuations of THz radiation power which may be caused by temporal fluctuations of the optical power. The transmission spectra of the THz radiation through polyethylene (PE, 2 mm thick), polytetrafluoroethylene (Teflon, 1 mm thick), and polypropylene (PP, 2.1 mm thick) plates are depicted in Fig. 4.2(a). Below 800 GHz, the THz radiation is nearly transmitted through the investigated plastic materials with a transmission of about 0.8-0.9. At higher frequencies, the transmission slightly decreases with increasing frequency. The same measurement procedures have been performed for paper, clothing sample made of cotton (dry and wet), a wood plate, and a glass plate which transmits visible light. The resulting transmission spectra are displayed in Fig. 4.2(b). As the frequency increases, all materials display a decrease in transmission, which in turn indicates a frequency-dependent transmission of THz radiation through the materials. The THz radiation is nearly completely transmitted through a sheet of paper with a thickness of 0.1 mm, with a constant transmission of about 0.8 at frequencies below 500 GHz and a decrease at

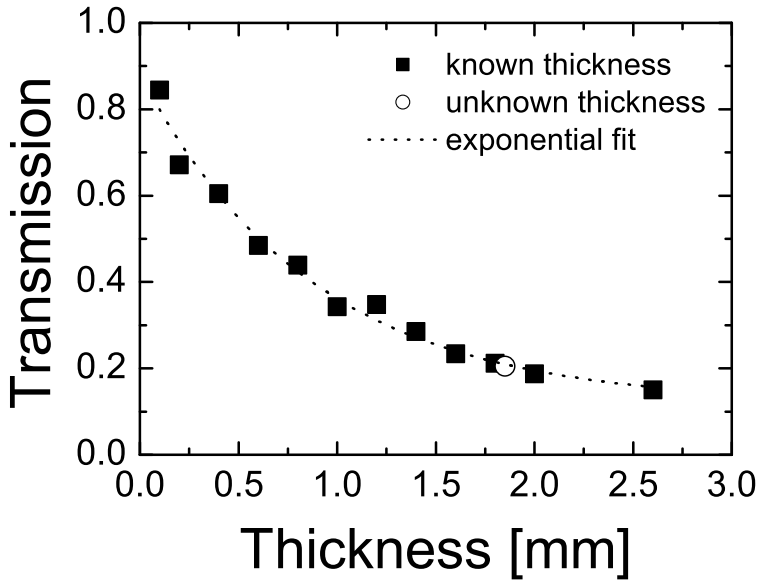

Fig. 4.3: Transmission of THz radiation at 379 GHz through a paper-stack as a function of thickness. The full squares represent the transmission of known thickness and the dotted line is a fit with an exponential decay. The open circle represents the position on the fit-curve corresponding to the measured transmission of the paper-stack with an unknown thickness.

higher frequencies at a relatively small rate compared to the other materials. The dry cotton sample with a thickness of 0.5 mm exhibits a high transmission of about 0.8 below 400 GHz and a strong decrease in the transmission at higher frequencies, approaching a transmission of 0.2 at about 900 GHz. For comparison, wet cotton material (same sample) has been studied for the transmission in the same frequency range. The result shows a complete attenuation of the THz radiation over the whole frequency range. This results from a high attenuation of the radiation by water contained in the wet clothing sample. Furthermore, it is interesting to note in Fig. 4.2(b) that the visibly transparent glass plate with a thickness of 0.8 mm permits propagation of THz radiation with the same transmission as a 2.9 mm thick wood plate. The wood plate was dried for 48 hours before measurement to extract moisture which might exist inside the plate. The glass and wood plates both show a transmission of 0.3 at 300 GHz and partly transmit THz radiation below 600 GHz. They block THz radiation completely at higher frequencies. This result shows an opacity of glass for THz radiation in contrast to visible light. The strong attenuation of THz radiation through the wood plate employed in the present experiment may be due to its larger thickness than of other samples.

While above measurement has been performed for several materials with various thick-

nesses, a transmission measurement has been performed for paper-stacks with various thicknesses at a fixed frequency of 379 GHz to investigate the transmission behavior of THz radiation as a function of thickness. The paper-stack consists of several sheets of identical paper with a thickness of 0.1 mm each. The thickness of the paper-stack is varied by varying the number of paper-sheets. The measured transmission of THz radiation through paper-stacks with different thickness is shown in Fig. 4.3. The transmission (full squares in Fig. 4.3) shows an exponential decrease with increasing thickness. The attenuation is described by the Beer-Lambert law [111]

$$T = e^{-\alpha(\nu)t}, \tag{4.1}$$

where T, $\alpha(\nu)$, and t represent transmission, frequency-dependent attenuation coefficient, and thickness of the sample, respectively. α can be determined by fitting an exponential decay to the measured data. The dotted line in Fig. 4.3 represents such a fit-curve according to Eq. (4.1). The measured data are in good agreement with the fit-curve. From the curve, the attenuation coefficient α at the frequency of 379 GHz is determined to be about $0.87\,\mathrm{mm}^{-1}$. With this value of α, the thickness of the paper-stacks can be determined by measuring the transmission of THz radiation. The open circle in Fig. 4.3 represents the position on the fit-curve corresponding to the measured transmission of 0.2 of a paper-stack with an unknown thickness. This transmission corresponds to a thickness of 1.85 mm, which is in good agreement with the geometrically measured value of 1.9 mm using a micrometer-measurement device. This result shows a potential application of the THz system for the quality control of the bulk non-metallic materials.

4.2 Absorption of THz Radiation

Another principal application of the THz system can be found in the spectral analysis of fundamental molecules. In particular, various polar molecules exhibit their absorption spectra arising from pure rotational transition in the THz frequency region. Therefore, many gases and gas mixtures can be monitored by sensing and identifying their absorption spectra by THz spectroscopy. Recently, many spectroscopic studies have been performed using THz time-domain spectroscopy or CW THz systems to sense such molecules or liquids [112, 113, 114, 115, 116]. In this section, the CW THz radiation source realized in the present work is tested for the capability of spectroscopic gas sensing. The transmission of THz radiation through gases is investigated as a function of frequency.

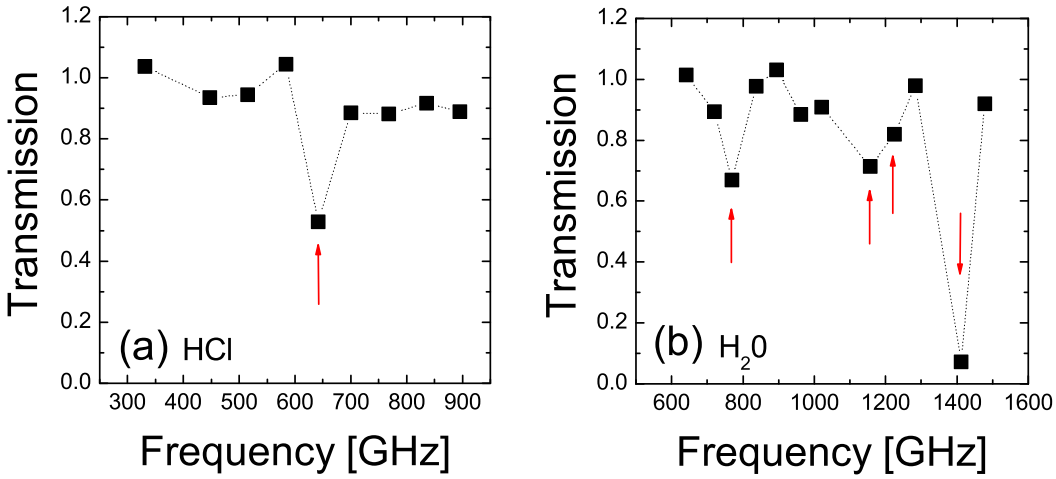

Fig. 4.4: Transmission of THz radiation depending on the frequency through (a) HCl in gas phase and (b) water vapor. The THz radiation power transmitted through the PE-bottles containing HCl and H_2O molecules is normalized to THz radiation power transmitted through the identical PE-bottle containing N_2. The arrows represent absorption lines. The dotted lines are for visual aid.

HCl and H_2O gases are employed as test samples in the investigations because they are polar molecules with well-known spectral lines in the THz frequency range [95, 113, 117]. Commercial plastic square bottles made of PE with a thickness of about 1 mm are used as a container for the gases. As shown in the previous section, PE is transparent for THz radiation. The width of the bottle is 8 cm. The bottles are first filled with N_2 gas to eliminate moisture contained in them and then, with a small amount of either liquid HCl or water at the bottom of the bottle. As a reference gas, N_2 gas is filled in an identical bottle. All gases in the bottles are at atmospheric pressure. For measurement, the bottles containing the samples are placed in the path of the THz radiation between two parabolic mirrors separated at a distance of about 14 cm, as shown in Fig. 4.1. The collimated THz radiation with a diameter of about 5 cm illuminates the section of the bottle above the liquid level, which contains gaseous species only. The transmitted radiation is detected by the bolometer. Every measurement of a sample is immediately followed by a reference measurement. The measured power of the THz radiation transmitted through HCl and H_2O gases is normalized to the reference value, which results in the normalized transmission through the gases. Consequently, the influence of the bottle on the transmission can be compensated. Furthermore, a propagation distance of 8 cm corresponding to the width of the bottle is ensured to be free from absorptions due to other atmospheric molecules in the path of the THz wave. This is particulary important for the measurement of H_2O absorption lines because of

the permanent existence of atmospheric water vapor in the remaining path of the THz wave.

The resulting transmissions for HCl molecules are depicted as a function of frequency in Fig. 4.4(a). The measured data show a complete transmission of THz radiation through HCl gas in the frequency range between 300 and 900 GHz, except a dip at 642 GHz (marked with an arrow in the figure) with a transmission of about 0.5. According to the manufacturer (Merck), the studied liquid HCl sample contains $^{1}H^{35}Cl$, whose rotational absorption line lies at a frequency of 626 GHz [117]. The determination of the difference frequency of the mixing laser modes has been limited to about 24 GHz at a wavelength of 785 nm due to the resolution of the OSA. Therefore, the measured spectral line corresponds to that of $^{1}H^{35}Cl$ within an error of $\pm 2.5\%$. The same uncertainty will also be seen in the following measurement of the H_2O spectral lines.

As another sample, the absorption lines of H_2O molecules are investigated in the frequency range between 600 GHz and 1.5 THz. The measured transmission spectra of H_2O are displayed in Fig. 4.4(b). The measured data show relatively low transmission at frequencies of 768 GHz, 1.157, 1.225 and 1.412 THz (marked with arrows in the figure), compared to data at other frequencies which show complete transmission. The frequencies with low transmission agree well with the rotational transition spectra of H_2O molecules at 752 GHz, 1.163, 1.229 and 1.411 THz, which are theoretically predicted and experimentally measured in the literature [95, 113, 118]. The measured spectral lines in the present investigation lie within an error of $\pm 2\%$ of the expected lines. Although there are rotational transitions at 1.153 and 1.158 THz, the measured line at 1.157 THz may rather correspond to 1.163 THz because the absorption strengths at 1.153 and 1.158 THz are much weaker than the absorption at 1.229 THz (cf. Fig 4.4(b)). The strongest absorption among the measured values occurs at 1.412 THz and the weakest at 1.225 THz. The behavior of relative absorption strength of the transitions also shows the theoretically predicted features well [118].

4.3 Summary

In this chapter, the frequency-tunable CW THz radiation source developed in the previous chapter has been employed for the spectral transmission studies of THz radiation through various materials and gaseous species. The application of the THz radiation to the investigation of transmission of non-metallic and non-polar materials such as plastics shows that such materials are transparent for THz radiation. Furthermore, absorption lines of HCl and H_2O molecules can be identified by THz spectroscopy. In particular, this is the first successful demonstration in THz technology of the spectro-

scopic application of CW THz radiation generated using a dual-mode SL for identification of chemical elements. The results achieved in the present chapter reveal that the THz radiation source realized in the context of the present work is a promising source for THz applications.

Chapter 5

Dual-Mode Operation of Broad Area Lasers and THz Generation

In the previous chapters, successful generation of THz radiation was demonstrated via photomixing of the two laser modes emitted by narrow stripe 2λ-ECSLs. The generated THz radiation had an output power of about 1 nW. It has also been demonstrated that this THz radiation power is sufficient for spectroscopic applications such as identification of molecules contained in an optically opaque plastic container. However, it is desirable to have higher power THz radiation sources, because they then shorten detection times with high signal-to-noise ratios. Theoretical and experimental studies have shown that the generated THz radiation power can be increased by an increase in applied bias voltage on the antenna and an increase in incident optical power. Since bias voltages cannot be infinitely increased due to possible electrical break-down of photoconductive materials, increasing the incident optical power is crucial to generate high power THz radiation. It must be kept in mind that, though an increase in the THz radiation power by increasing incident optical power is not limited by physical principles, this method is in practice allowed only below a power limit given by possible thermal damage to the photomixer due to Joule heating at high antenna current.

Recently, narrow stripe SLs with a power of about 150 mW are commercially produced, but higher achievable output power is limited due to catastrophic optical damage (COD) of the laser output facet. High power SLs overcoming this limitation can be achieved by increasing the width of the active stripe of SLs up to about 200 μm. Such SLs are called broad area semiconductor lasers (BALs) and emit output powers of up to several watt. Therefore, BALs are very attractive, potential optical sources to generate high power THz radiation. However, the broadening of the stripe results in a substantial deterioration of the beam quality [119]. Improving the beam quality of BALs in addition to their high output power is thus of importance for efficient THz generation.

In this chapter, the generation of the THz radiation will be demonstrated using a dual-mode BAL as an optical excitation source for photomixing. First, an overview

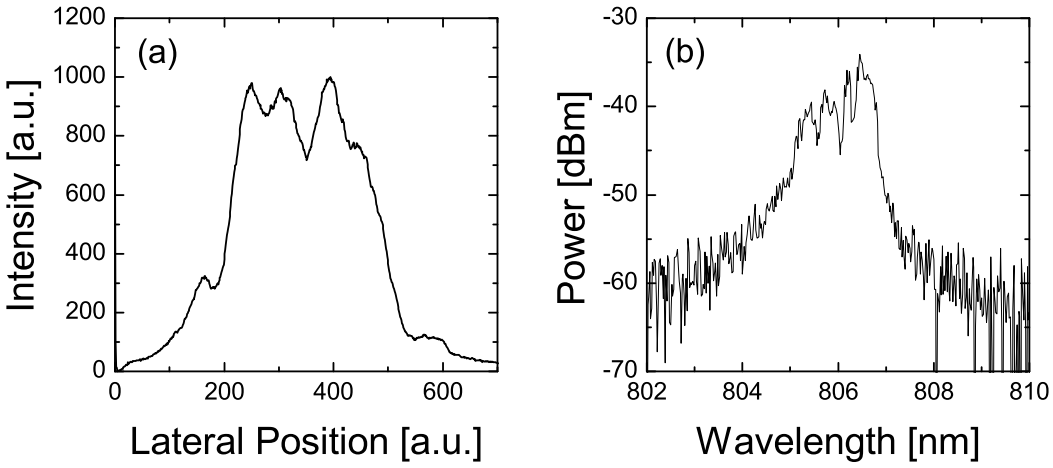

Fig. 5.1: Intensity distribution on the laser output facet along the lateral direction (a) and its optical spectrum (b) of a free running BAL at an injection current of $2I_{th}$.

of the basic properties of a BAL will be given. Subsequently, the generation of the THz radiation and its spectral characteristics will be discussed. Furthermore, intensity modulation of the dual-mode beam of a BAL will be characterized. Finally, temporally integrated spatial intensity profiles of the dual-mode BAL will be investigated. Thereby, a scheme for controlling the spatial beam profile and its results will be discussed.

5.1 Characteristics of Broad Area Lasers

Broad area lasers are edge-emitting SLs with an active stripe width (i.e., lateral dimension of the active zone) of about 50 - 200 μm, in contrast to narrow stripe SLs having a width typically less than 5 μm. While broadening the active width of the SLs, on the one hand, enables to enhance optical output powers up to several watts without causing COD, it, on the other hand, allows many lateral modes to oscillate simultaneously. BALs typically exhibit spatially modulated intensity distributions in the near-field and far-field, which are induced by the nonlinear interaction of the intense optical field with the SL medium and the emission of lateral multimodes. Nonlinear mechanisms such as spatial hole burning and self-focussing result in a static (i.e., temporally averaged) intensity modulation with several maxima - filaments - along the lateral direction in the near field of the BAL [119, 120]. This spatial intensity modulation is well-known as static filamentation. Figure 5.1(a) shows a temporally averaged intensity distribution along the lateral direction of the output facet of a 50 μm wide BAL (Coherent

S-81-500C-50-C), driven with an injection current of $2I_{th}$ ($I_{th} = 150\,\mathrm{mA}$). The intensity profile exhibits a modulation with approximately three maxima along the lateral direction. Furthermore, BALs exhibit complex spatiotemporal emission dynamics on picosecond time-scales [121, 122, 123, 124, 125, 126, 127] such as lateral migration of filaments across the laser facet, which is known as dynamic filamentation, and fast pulsations of light with a period of the round-trip time in the laser-cavity. Responsible mechanisms for such spatiotemporal dynamics are the interplay of self-focussing, spatial hole burning, spatial carrier diffusion and diffraction [121] associated with lateral and longitudinal mode-coupling [128].

Moreover, BALs generally exhibit longitudinally multimode emission. An optical spectrum of the free running BAL corresponding to Fig. 5.1(a) is displayed in Fig. 5.1(b). The spectrum exhibits a broad spectral range of about 2 nm (920 GHz) with a longitudinal mode separation of about 0.12 nm (55 GHz). Each of these longitudinal modes contains many lateral modes of several orders, which constitute a so-called longitudinal mode-family. Since these lateral modes have a mode separation of ten times smaller than the longitudinal modes, they have not been resolved in Fig. 5.1(b). Spectrally resolved near-field profiles of the BAL enable to unveil the oscillation of several lateral modes in each longitudinal mode-family. Figure 5.2 shows a section of a spatially resolved optical near-field spectra of the BAL (Coherent S-81-600C-50-C). The horizontal and vertical coordinates represent the wavelength and the lateral position of the laser facet, respectively. Fig. 5.2 shows lateral modes of up to third orders oscillating in each of the 8 longitudinal mode-families, where higher order modes have shorter wavelengths. The lateral and longitudinal mode separations amount to about 0.02 nm (9.2 GHz) and 0.12 nm (55 GHz), respectively. It is interesting to observe that lateral modes of different order can dominate in different longitudinal mode-families.

Due to static and dynamic filamentation, BALs exhibit poor beam quality with a so-called M^2 of 20-100, compared to the diffraction-limited laser beam having M^2 in the order 1. Here, M^2 is a parameter describing beam quality [129]. Therefore, a trade-off between the high beam quality with low order lateral mode operation and high output power must be made for applications such as spectroscopy and photomixing. Recently, it has been experimentally demonstrated that the emission characteristics of BALs can be controlled and stabilized by spatially filtered feedback in an external cavity configuration [126, 127], revealing improved beam quality. This demonstration gives hope to realize dual-mode emission of BALs with high output power and high beam quality. The application of the same principle reported in Ref. [126] to dual-mode emission of BALs will be discussed in a later section.

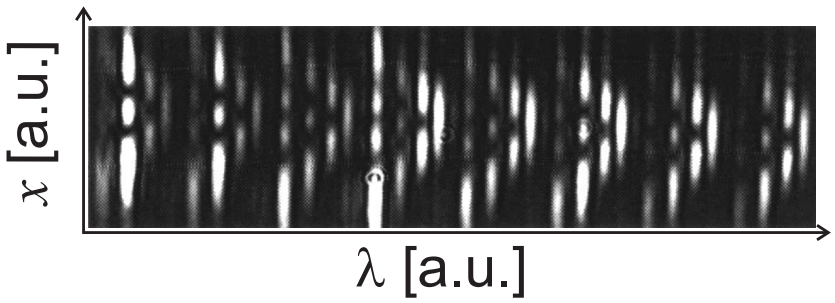

Fig. 5.2: Spectrally resolved near-field profiles of the solitary BAL (Coherent) with a stripe width of 50 μm at a injection current of $I = 2I_{th}$. The horizontal axis and vertical axis denote the wavelength (λ) and the lateral position (x) on the laser facet, respectively. The longitudinal and averaged lateral mode separations are of 0.12 nm and 0.02 nm, respectively. Courtesy of T. Burkhard [125].

5.2 THz Wave Generation using Dual-Mode Broad Area Laser

In the present section, the generation of THz radiation will be performed via photomixing using a frequency-tunable dual-mode BAL as an optical excitation source[1]. Furthermore, the generated THz radiation has been spectrally characterized with a FTS. The investigation for the dual-mode emission of BALs will be discussed in section 5.3.

5.2.1 Experimental Setup

A frequency-tunable dual-mode BAL has been realized by employing a BAL (Coherent S-81-600C-50-C) as the laser source in the Double-Littman-external-cavity-configuration (2λ-ECBAL). The employed solitary BAL emits TM-polarized, multiple longitudinal modes with a central wavelength of about 803 nm, a longitudinal mode separation of 0.08 nm (37.2 GHz), and a maximum output power of 600 mW. The BAL has a reflectivity of 95 % for the rear facet and 5 % for the front facet. Its threshold current I_{th} amounts to 190 mA. The experimental setup for the 2λ-ECBAL and the subsequent generation and detection of THz radiation is depicted in Fig. 5.3. The configuration is the same as that for the 2λ-ECSL employing a narrow stripe SL, except, now, a cylindrical lens is employed. Due to astigmatism, the laser beam can be

[1]The measurements have been performed by S. Bakić in the context of the present work. See Ref. [96]

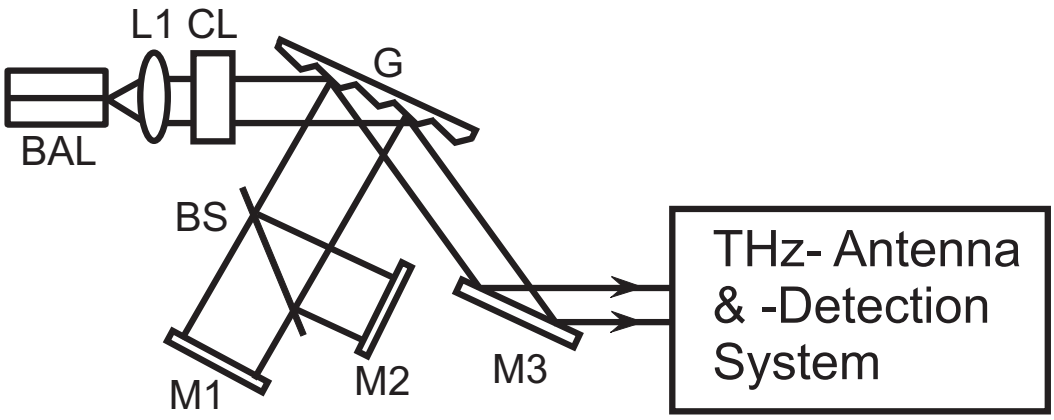

Fig. 5.3: Schematic diagram for 2λ-ECBAL and THz wave generation and detection. The THz-antenna and -detection system is the same as the experimental configuration depicted in Fig. 3.7 in chapter 3, except the Si lens which has not been employed in the present configuration. Here, CL denotes a cylindrical lens employed to collimate the slow axis beam.

collimated either with two cylindrical lenses or, alternatively, with a combination of an aspheric lens and a cylindrical lens. In the present experiment, the latter method has been used with a focal length of 4.5 mm (NA0.55) for the aspheric lens (L1) and 15 mm for the cylindrical lens (CL). The fast axis beam (highly divergent beam in the transversal direction) is first collimated with L1. Collimation of the slow axis beam (low divergent beam in the lateral direction) is ensured by inserting the CL. The collimated beam is then incident on the grating (G, 1200 grooves/mm). The first order beam of the grating is coupled to the external cavities for the spectral selection, and the zeroth order beam is coupled out for the generation and detection system of the THz radiation. The generation and detection system for the THz radiation comprises the same configuration depicted in Fig. 3.7 in chapter 3. The laser is driven at a constant injection current of 300 mA ($1.6I_{th}$) at room temperature. The total optical output power of the 2λ-ECBAL amounts to 46.2 mW. This output power only amounts to a small part of the achievable maximum, but, in the conducted experiments, the safety range of the input power of the antenna was taken into consideration. The laser beam is then chopped with a frequency of 237 Hz for a lock-in detection. Due to chopping with a duty cycle of 50 %, the time-averaged optical power incident on the antenna is 23.1 mW. The incident optical power is varied using a variable beam attenuator placed in the laser beam. The optical spectrum is monitored using an OSA with a resolution of 0.1 nm. The same type of log-periodic antenna as that employed in chapter 3 has been used to generate THz radiation. The antenna is biased at a voltage of 20 V. The generated THz radiation is detected using a bolometer and is spectrally characterized

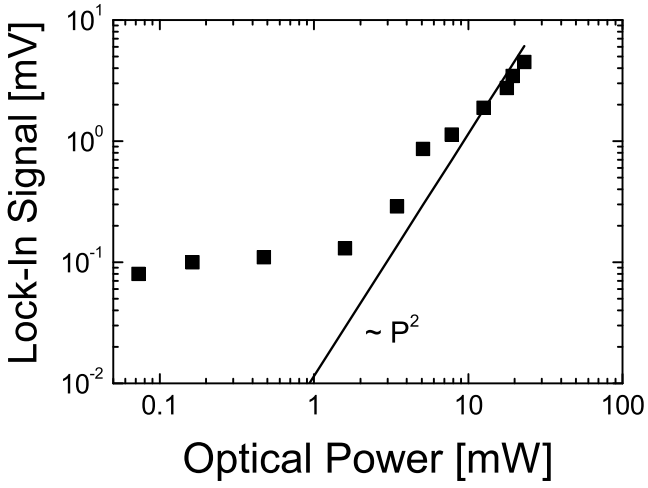

Fig. 5.4: Generated THz radiation power as a function of incident optical power. The full squares denote experimentally obtained data in Ref. [96]. The solid line represents a quadratical relation between THz radiation power and the optical power.

with a FTS. However, in the present experiment, the Si lens has not been employed, which results in a low coupling efficiency of the THz radiation into free space and into the bolometer. Therefore, the bolometer signal is amplified by a preamplifier with a gain of 1000 to attain appreciable bolometer signals.

5.2.2 Results and Discussion

First, the generated THz radiation power has been studied as a function of the incident optical power. The difference frequency of the two modes is kept constant at 465 GHz. Figure 5.4 displays the generated THz radiation power (full squares), which is proportional to the lock-in signal, as a function of the incident optical power. The theoretically expected quadratic relation between the THz radiation power and optical power is also depicted as a solid line in Fig. 5.4. At optical powers below 2 mW, the THz radiation power exhibits only a slight increase with the optical power and deviates from the expected quadratic behavior. Above 2 mW, the measured THz radiation power increases strongly with increasing optical power and approaches the theoretically expected quadratic relation. The deviation below 2 mW might be due to background noise in the measurement which, however, could not be identified. The quadratic increase in the THz radiation power with respect to the optical power confirms that the

detected signal is indeed the THz radiation generated in the antenna via photomixing. The achieved maximum lock-in signal in Fig. 5.4 amounts to 4.52 mV at an optical power of 23.1 mW with a SNR of 5.7:1. Thereby, the antenna current amounts to 419.8 μA. This lock-in signal corresponds to a THz radiation power of 19 pW. Therefore, the achieved conversion efficiency of the optical to the THz radiation power is 8.2×10^{-10}. The theoretically expected THz radiation power at the given antenna current should be 5.4 μW according to Eq. 3.4. If the effect of the impedance mismatch between the antenna and the photomixer on the THz generation is taken into account, the achievable THz radiation power amounts to 10.8 nW. This THz radiation power corresponds to a conversion efficiency of 4.7×10^{-7}. In contrast to the result obtained in section 3.3.7, the detected THz radiation power in the present section is of the order of 3 smaller than the theoretically achievable value. One reason might be the low coupling efficiency of the THz radiation from the antenna into free space and subsequently into the bolometer due to the lack of the Si lens in the measuring equipment (see section 3.2). Another reason might be the power difference between the two optical modes. The achievable THz radiation power is calculated under the assumption that the two laser modes exhibit equal power, which gives a maximum THz radiation power at a given total optical power. The power difference between the two optical modes causes a lower generation of THz radiation. Further reason might be the lower THz radiation power generated when the laser emission consists of many modes compared to the THz radiation power generated for dual-mode operation containing only two modes (see section 3.3.4). The spectral characteristics of the generated THz radiation obtained by a FTS measurement will be discussed later in the present section. Finally, the intensity of the laser beam might not be perfectly modulated with the difference frequency, which might be caused by possible imperfect spatial overlap of the two modes in the BAL's broad active width. The intensity modulation of 2λ-ECBAL will be studied in a later section. It should be noted here that, in contrast to the case in section 3.3.7, the antenna's frequency-characteristics play no role for the lowered THz power generation, because the investigated THz frequency in the present section lies in the frequency region where the generated THz radiation exhibits the theoretically expected behavior (see Fig. 3.17).

In general, BALs emit laterally and longitudinally multimode. Although the spectra monitored with the OSA exhibit only two peaks indicating dual-mode operation, several longitudinal mode-families consisting of lateral modes might oscillate in each of the two peaks. Because the employed OSA (Anritsu) has a spectral resolution of 0.1 nm, neither neighboring longitudinal modes nor lateral modes can be resolved in the optical spectra. However, a FTS measurement of the generated THz radiation can conform spectral purity of the generated THz radiation within the resolution limit of about 2 GHz. Figure 5.5(a) shows an optical spectrum recorded with the OSA for

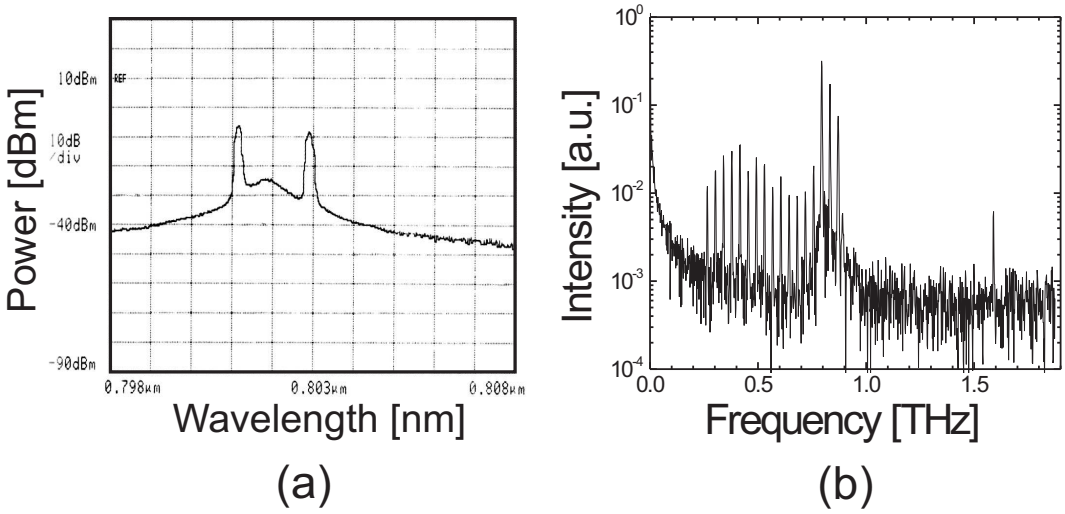

Fig. 5.5: (a) An optical spectrum of dual-mode operation of 2λ-ECBAL with a difference frequency of 792 GHz and (b) FFT-spectrum obtained as a result of FTS measurement of the generated THz radiation. Courtesy of S. Bakić [96].

dual-mode operation of 2λ-ECBAL with a difference frequency of 792 GHz. The OSA-spectrum exhibits two peaks at 801.2 nm and 802.9 nm without any other considerable oscillating modes. Photomixing of this laser beam has generated THz radiation for which a FTS measurement has been performed. A FFT-spectrum of the resulting FTS-interferogram is displayed in Fig. 5.5(b). The FFT-spectrum exhibits many THz peaks below 1 THz with three high peaks near 800 GHz and a peak at 1.59 THz. The frequency difference of the peaks amounts to about 37.5 GHz, which corresponds to the longitudinal mode separation of the solitary BAL. The highest peak lies at a frequency of 794 GHz. This frequency agrees well with the difference frequency of the two laser peaks in Fig. 5.5(a). The identification of further THz waves near 794 GHz with high intensities and a frequency difference of 37.5 GHz indicates that each laser peak in Fig. 5.5(a) contains more than one longitudinal mode with comparable intensities. These modes could not be resolved by the employed OSA due to its limited resolution. Measurements using an OSA with a higher resolution or a Fabry-Perot interferometer, however, have confirmed that each of the spectral laser peaks consists of several longitudinal modes. Furthermore, they might also contain several lateral modes. However, a clear identification of lateral modes would be achieved by a investigation of spectrally resolved optical near-field profiles of the 2λ-ECBAL. THz waves at frequencies below 700 GHz are generated via photomixing of the two laser peaks with the modes which lie between the two laser peaks in Fig. 5.5(a). The laser modes between the two peaks in Fig. 5.5(a) are longitudinal mode-families of the solitary BAL, which cannot

be effectively suppressed at a large detuning frequency of the selected dual-mode operation and therefore have enough gain to oscillate simultaneously with the two modes. Their intensities are about 20 dB larger than the noise level and photomixing between these modes and the main laser peaks contributes to the generation of THz radiation with corresponding difference frequencies and noticeable power. Therefore, suppression of numerous solitary laser-modes must be accomplished to achieve THz radiation with a desired single frequency. The suppression of solitary laser-modes at large difference frequency can be achieved by lowering the facet-reflectivity using an antireflection coating.

Furthermore, it is worthy noting that an additional THz wave can be identified at a frequency of 1.59 THz in Fig. 5.5(b). This frequency is twice the frequency of the highest peak at 794 GHz in the FFT spectrum. Because no optical waves at the corresponding difference frequency of 1.59 THz can be identified in Fig. 5.5(a), the THz wave at 1.59 THz cannot result from photomixing of laser modes. This THz wave might rather be attributed to second harmonic generation (SHG) of the THz wave at 794 GHz in the photoconductive material. Second and higher order harmonic generation of THz radiation in the photoconductive antenna device has also been reported in Ref. [107, 130]. However, nonlinear interactions of THz waves with the semiconductor materials have not yet been extensively studied. The study of nonlinear light-matter interactions in the THz frequency range still remains of great interest.

5.3 2λ-ECBAL with spatially filtered feedback

Dual-mode emission of a BAL and its successful application to generation of the THz radiation have been presented in the previous section. The FFT-spectrum of the THz radiation, however, has exhibited that, in addition to the desired frequency, many other THz waves have also been generated. These additional THz waves have been attributed to photomixing of many laser modes which have not been completely suppressed. Due to lateral and longitudinal multimode emission of BALs, mode-selection must be performed not only longitudinally, but also laterally for the realization of spectrally narrow dual-mode emission of the BAL. Lateral mode-selection is of significance for the efficient generation of the THz radiation, because oscillations of several lateral modes limit the focusable optical power. Recent studies have demonstrated that the emission dynamics of BALs can be controlled and stabilized by spatially filtered feedback [126, 131]. The principle of spatially filtered feedback is structured feedback of the beam by using a curved external mirror [131]. The curved mirror reflects only paraxial beam into the laser so that the fundamental lateral mode is preferred. Therefore,

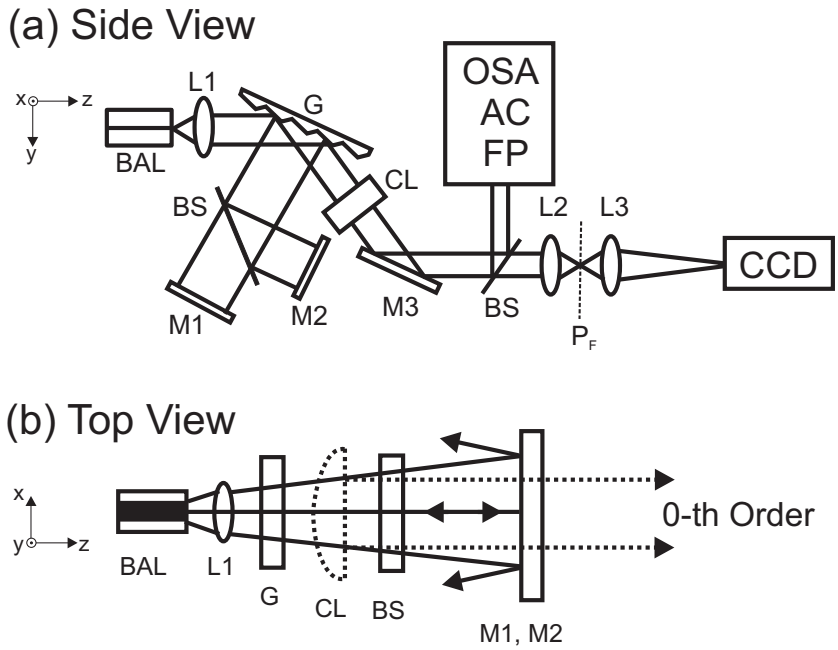

Fig. 5.6: Schematic of the experimental setup for characterization and control of dual-mode emission of 2λ-ECBAL with spatially filtered feedback. (a) shows a side view (fast axis) of the BAL. P_F represents a focal plane of the lens L2. (b) shows a top view (slow axis) of the BAL. The solid lines represent the first order beam of the grating in the external cavities. The dashed lines and the dashed cylindrical lens (CL) represent the zeroth order output beam of the grating and a cylindrical lens placed in the zeroth order beam, respectively.

the beam quality can be improved and the emission can be stabilized. In the following sections, 2λ-ECBAL employing the principle of spatially filtered feedback will be introduced, followed by spectral and spatial characterizations of dual-mode emission of the realized 2λ-ECBAL. Here, 50 μm wide BALs are used because the number of possible lateral modes of the 50 μm-BAL are smaller than of wider BALs. Hence, the control of the lateral modes might be easier.

5.3.1 Experimental Setup

The experimental setup for 2λ-ECBAL employing the principle of spatially filtered feedback is shown in Fig. 5.6. The configuration depicted in Fig. 5.6(a) (side view of the BAL) is the same as the configuration depicted in Fig. 5.3, except for the position of the cylindrical lens (CL). The BAL (Coherent S-81-500C-50-C) is the same type as the BAL used for the generation of the THz radiation in Fig. 5.3. In the present

configuration, the laser beam of the fast axis is collimated by an aspheric lens L1 with a focal length of 4.5 mm. Due to astigmatism, the slow axis beam, having passed L1, diverges further but with a smaller divergence angle than before passing L1. The beam is then incident on the grating (G) with 1200 grooves/mm. In the zeroth order of the grating the slow axis beam is collimated by a cylindrical lens with a focal length of 300 mm. The zeroth order beam, which is then collimated in both slow and fast axis directions, is then coupled out as output. The beam collimation of the zeroth order is shown in Fig. 5.6(a) and with a combination of dashed lines in Fig. 5.6(b). The first order beam of the grating is directed into the external double-cavity configuration for the spectral selection of the two longitudinal modes. The length of each external cavity is 40 cm. By rotation of the mirrors about the x-axis as shown in Fig. 5.6(a), two desired external longitudinal modes are selected in the gain range of the laser. In addition, spatially filtered feedback is also performed in the external cavities, which is shown in Fig. 5.6(b). Here, the divergence of the slow axis is used for the spatial filtering of the beam. The paraxial part of the divergent slow axis beam is reflected back into the laser at two external plane mirrors (M1 and M2) and the divergent part is reflected away from the external cavity. In the present configuration, plane mirrors are used for spatially filtered feedback instead of curved mirrors. Employing plane mirrors enables easier handling for the optimum feedback of the laterally fundamental mode. The optimum feedback using the curved mirror is more critical than the plane mirror, although the curved mirror may give better control of lateral modes when the lateral mode-spacing is narrow. The optimum feedback depends on the lateral position of the mirror with respect to the beam axis. The center of curvature of the mirror must be located on the beam axis. Otherwise, higher order mode can be reflected back into the laser instead of the fundamental mode. The optimum feedback position of a plane mirror is not determined by its lateral position but by its tilt angle.

The optical spectra of the BAL are recorded with an OSA and a Fabry-Perot interferometer (FP) with FSR = 10 GHz. The simultaneous oscillation of two laser modes of 2λ-ECBAL is monitored with a collinear autocorrelator (AC). Moreover, the static intensity distribution on the laser output facet is recorded by a CCD-camera. The collimated beam is focussed onto a virtual plane denoted by P_F with an aspheric lens (L2) with a focal length of 5 mm. The image at P_F is then projected on the CCD-camera chip with an aspheric lens (L3) with a focal length of 6.2 mm. The image of the focal point at P_F is the image of the laser facet and consequently the image projected on the photomixer.

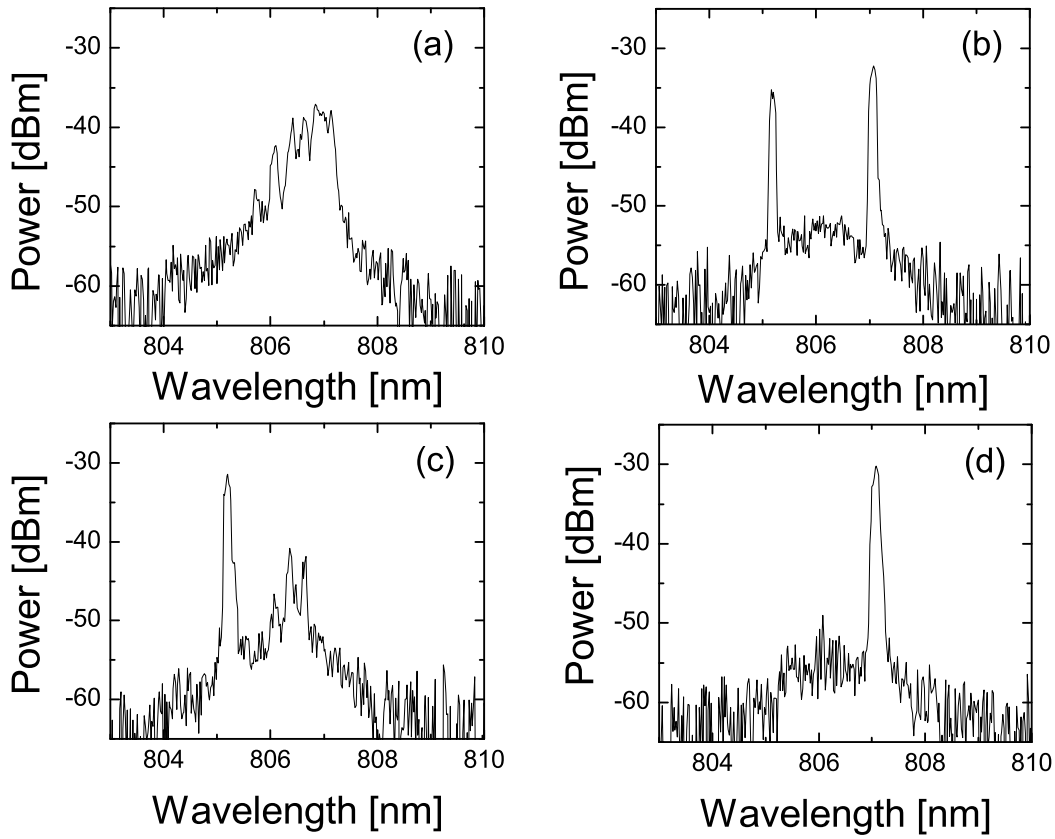

Fig. 5.7: Optical spectra of BAL: (a) free running emission, (b) dual-mode emission of 2λ-ECBAL, (c) and (d) feedback either by the external mirror M1 or M2, respectively.

5.3.2 Optical Spectra of Dual-Mode Emission of 2λ-ECBAL

Using the configuration depicted in Fig. 5.6, frequency-tunable dual-mode emission of the BAL has been investigated. Optical spectra of the BAL are displayed in Fig. 5.7 with and without spatially and spectrally filtered feedback. The BAL is driven at an injection current of $I_{inj} = 1.6I_{th}$ (corresponding to an output power of 55 mW). For comparison, a spectrum of the free running BAL (i.e., without feedback) is shown in Fig. 5.7(a). At this injection current, the free running BAL emits longitudinally multimode with a spectral range of 2 nm at about 806.6 nm. The maximum peak lies at a wavelength of 806.8 nm. The individual lateral modes are not resolved in the spectrum. The dual-mode emission of the BAL can be realized with the spectrally filtered feedback from the two external cavities. Figure 5.7(b) shows a spectrum of dual-mode emission whose modes are selected by the two external cavities. The two longitudinal modes oscillate at wavelengths of 805.2 and 807.08 nm. The difference wavelength is 1.88 nm and corresponds to a difference frequency of 868 GHz. With feedback from

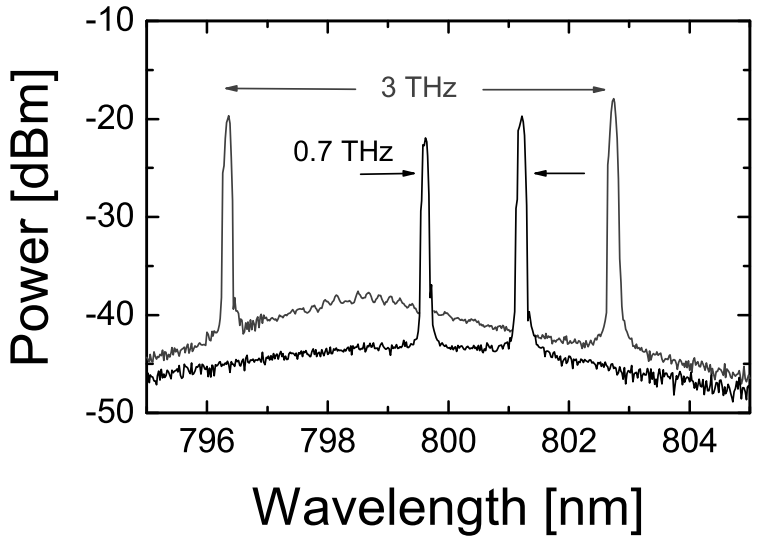

Fig. 5.8: Optical spectral of BAL for difference frequencies of 0.7 THz (dark gray) and 3.1 THz (black). The output power amounts to about 120 mW at $I_{inj} = 1.5I_{th}$.

the external cavities, the solitary laser modes are completely suppressed and only two external cavity-modes oscillate in the laser. The simultaneous oscillation of the two modes has been proved by the intensity autocorrelation measurement which exhibits an autocorrelation trace with a period corresponding to the difference frequency of the two external modes. The intensity autocorrelation measurements will be discussed in the next section. In contrast to the dual-mode emission, feedback from only one external cavity cannot completely suppress the solitary laser modes. The optical spectra for the feedback either by mirror M1 or M2 are shown in Fig. 5.7(c) and (d), respectively. When the external modes are selected near the edges of the gain spectrum, the solitary laser modes oscillate in addition to the external mode. Fig. 5.7(c) shows an external cavity-mode at 805.2 nm and several solitary laser modes between 806 and 807 nm. This multimode emission results from the fact that the solitary laser modes near the gain maximum acquire enough gain due to the residual reflectivity of the laser facet of 5 % to compete with the external mode. Feedback of the external mode lying near the gain maximum of the laser effectively suppresses the solitary laser modes so that almost single external mode oscillation is achieved in the laser as shown in Fig. 5.7(d). However, the solitary modes are not completely suppressed due to the facet-reflectivity. These solitary laser modes can be seen as small peaks near 806 nm in Fig. 5.7(d).

In the present study, the tunable dual-mode emission has been realized in the difference frequency range between 100 GHz and 1 THz with the maximum output power of 220 mW at $I_{th} = 3I_{th}$. At injection currents below $2I_{th}$, the linewidth of the ex-

ternally selected modes could not be resolved by the OSA due to its resolution limit of 0.1 nm. Above $2I_{th}$, broadening of the linewidths with increasing injection current can be clearly observed. This broadening of the modes indicates that each external peak contains more than one longitudinal mode. Even though two external modes can be tuned with larger difference frequencies, dual-mode emission cannot be achieved due to excitation of the solitary laser modes. An extension of the detuning frequency can be achieved by lowering the reflectivity of the laser facet using an antireflection coating. By using a 100 μm wide BAL (GaAsP) with a antireflection coating on the output facet, the extension of the detuning frequency has been shifted to about 3 THz at $I_{inj} = 1.5I_{th}$ ($I_{th} = 600$ mA with an antireflection coating and a central wavelength of 807 nm). However, due to the oscillation of the solitary laser modes at high injection currents, the output power of the above mentioned case of 220 mW could not be achieved. The achieved output power amounts to about 120 mW. The spectra for the dual-mode emission of the 100 μm BAL are shown in Fig. 5.8 for the difference frequencies of 0.7 and 3.1 THz.

5.3.3 Spectrally and Spatially Controlled Dual-Mode Emission of BAL

The beam filamentation and spatiotemporal instabilities of BALs limit their application as high power laser in many fields. In particular, their low focusable beam quality limits the efficiency of photomixing for the THz wave generation at a given total optical power. Therefore, control of the emission properties of the BAL is of considerable interest for its application as a high-power laser source for effective, high-power THz wave generation via photomixing. Recently, various concepts have been studied to control the emission properties of the BAL. They include schemes such as injection-locking [132] and spatially or spectrally filtered feedback in an external-cavity-system [126, 127, 131, 133, 134, 135]. In particular, the successful demonstration of the control and stabilization of BAL's emission using an external cavity with a spatially filtered feedback [126, 127] indicates that the same principle employed in Fig. 5.6 can also improve the emission characteristics of the 2λ-ECBAL.

Therefore, in this section, the effect of spatially filtered feedback has been investigated by recording temporally integrated images of the spatial intensity distribution focused at the plane P_F in Fig. 5.6. This spatial intensity distribution corresponds to the intensity distribution along the output facet of the BAL. Figure 5.9 displays temporally integrated images of the spatial intensity distribution of 2λ-ECBAL beams at the plane P_F. The upper images display images of the BAL's facet acquired with a CCD-camera. Their corresponding intensity profiles along the lateral direction (x-axis) are displayed

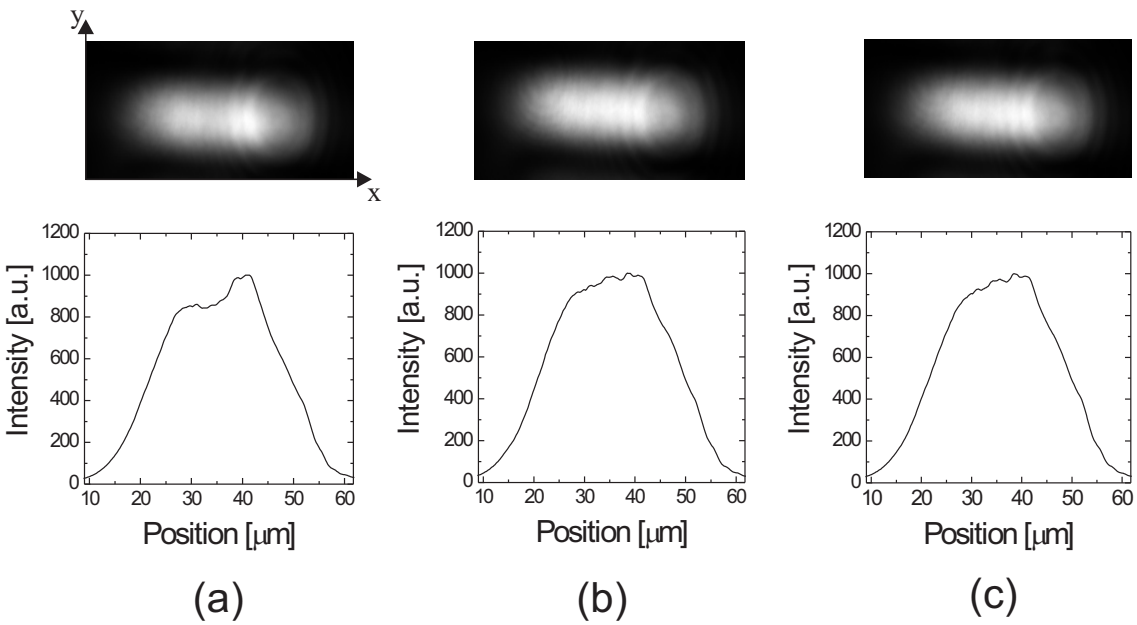

Fig. 5.9: Temporally integrated images of spatial intensity distribution of 2λ-ECBAL beams at P_F pictured with a CCD-camera (top) and its corresponding intensity profiles along the lateral direction of BAL (bottom) for (a) a free running BAL (no feedback), (b) dual-mode operation (feedback from two external mirrors) with a difference frequency of 527 GHz, and (c) feedback from only one external mirror. x and y represent the lateral and transverse spatial-directions of BAL, respectively.

in the lower diagrams of Fig. 5.9. The laser is driven with an injection current of 223 mA ($1.5I_{th}$). For dual-mode operation, two external modes are selected at wavelengthes of 804.9 and 806.04 nm, which corresponds to a difference frequency of 527 GHz. As a comparison, an image of the intensity profile of the free running BAL (i.e., both external cavities are blocked) is depicted in Fig. 5.9(a). The intensity profile of the free running BAL exhibits two maxima: high intensity at the right side and a relatively weak intensity at the left side. Compared with the free running BAL, the intensity profile during dual-mode operation of the 2λ-ECBAL with spatially filtered feedback from both external cavities exhibits a single peak with a Gaussian-like distribution, which is displayed in Fig. 5.9(b). Furthermore, the intensity profile of the BAL with feedback from only one cavity (i.e., the other cavity is blocked) exhibits the same feature as the intensity profile during dual-mode operation. The occurrence of interference fringes in the CCD-images is due to dust particles on the entrance window of the CCD-camera. The Gaussian-like intensity profile indicates the improved beam profile of the BAL with the spatially filtered feedback, and the fact that the BAL with spatially filtered feedback can probably emit a single, low-order lateral mode, as has been reported

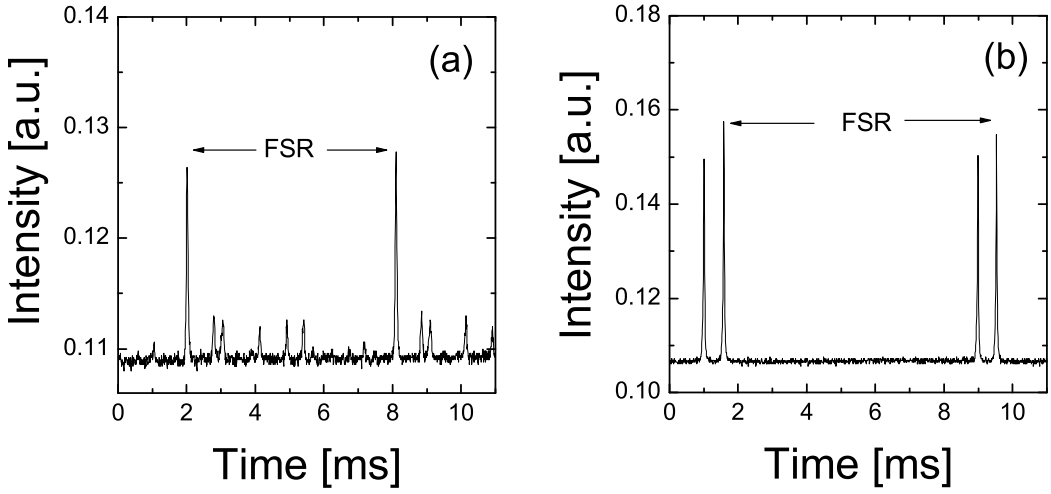

Fig. 5.10: Fabry-Perot interferogram of (a) free running BAL (with no feedback) and (b) dual-mode operation of 2λ-ECBAL (with feedback) with a difference frequency of 342 GHz. The laser is driven with an injection current of 228 mA. FSR = 10 GHz.

in Ref. [126]. The control of lateral modes, however, is sensitive to the alignment of the external mirrors. Optimum feedback is achieved when the external mirror is aligned perpendicular to the optical axis of the laser beam so that low-order lateral modes, which have a low divergence angle, are reflected back into the active layer of the BAL [126]. Deviations from the optimum feedback due to slight tilt of external mirrors result in feedback of laterally higher-order modes and consequently oscillation of higher-order lateral modes. The intensity profile at P_F in Fig. 5.6 then exhibits no longer the Gaussian-like profile. In similar investigations it has been observed that tilt of any of the two external mirrors from the optimum feedback position destroys the Gaussian-like intensity profiles of dual-mode operation. Therefore, since the configuration for 2λ-ECBAL contains two external mirrors, both mirrors should guarantee the optimum feedback to achieve fundamental lateral mode emission.

In addition, under the same condition, optical spectra have been monitored with an OSA and a scanning Fabry-Perot interferometer. The OSA-spectra have exhibited multiple longitudinal modes emitted by the free running BAL and two narrow longitudinal modes during dual-mode operation. However, due to the limited resolution, lateral modes are not resolved in the OSA-spectra. The oscillation of multiple lateral modes can be monitored with a Fabry-Perot interferometer with a FSR of 10 GHz. The spectra of free running and dual-mode operation of 2λ-ECBAL are depicted in Fig. 5.10(a) and (b), respectively. The spectrum of the free running BAL displayed in Fig. 5.10(a) exhibits several peaks which can be associated with several longitudinal and lateral

modes. Comparison to Fig. 5.10(a), the spectrum of dual-mode operation displayed in Fig. 5.10(b) exhibits only two externally selected longitudinal modes. Since each of the two longitudinal modes can contain lateral modes of different order, it cannot be clearly distinguished from the Fabry-Perot spectrum alone whether the two external modes oscillate in the lateral mode of fundamental order. However, the image of the Gaussian-like intensity profile in Fig. 5.9 and the Fabry-Perot spectrum in Fig. 5.10(b) together indicate that the 2λ-ECBAL with spatially filtered feedback emits a single, fundamental-order lateral mode. Using the method of spectrally and spatially filtered feedback, spectrally and spatially controlled dual-mode operation of the 2λ-ECBAL can be achieved with a difference frequency of up to 827 GHz and with an injection current of up to $2I_{th}$. The achieved output power amounts to about 90 mW. At larger difference frequencies and higher injection currents, solitary laser modes and higher-order lateral modes begin to oscillate gradually. Hence, Fabry-Perot spectra and intensity profiles exhibit multimode-emission and structured intensity profiles with weak filamentation, respectively. This degradation of the intensity profile at high injection currents is supposed to be attributed to thermal lensing [126], filamentation and higher-order lateral modes whose modal profiles depend on the gain defined by the carrier-injection profile [127]. However, the intensity profiles with spatially controlled feedback still show weaker filamentation than the intensity profile for the free running BAL, which indicates that the fundamental mode is preferred due to the spatially filtered feedback [126].

The results achieved in the present section show that the dual-mode emission of 2λ-ECBAL can be controlled through spatially and spectrally filtered feedback so that longitudinal and lateral single-mode emission is achieved. Furthermore, the beam quality of the BAL is improved to form a Gaussian-like intensity profile, which gives better focusable beam quality. Further improvement of the emission characteristics of 2λ-ECBALs at high injection currents and the generation of THz radiation using spectrally and spatially controlled 2λ-ECBALs are still tasks to be performed.

5.3.4 Intensity Modulation of Dual-Mode Emission

As mentioned in section 5.1, BALs generally emit multiple longitudinal and lateral modes. In particular, intensity distribution among the lateral modes within a longitudinal mode-family may temporally vary [125]. Moreover, the two selected longitudinal modes of 2λ-ECBAL can contain lateral modes of different orders. Since two lateral modes of different orders have spatially different intensity distributions, the spatial overlap of the two lateral modes will not be perfect. Furthermore, due to a wide stripe width of BALs, it is possible that each of the two selected longitudinal modes can

be partially amplified in laterally different parts of the laser medium. The emission of the two laser modes from laterally different parts of the laser facet, particularly, results in incomplete spatial overlap of the two modes. Consequently, the degree of total intensity modulation of the laser output beam is reduced, which results in lower photocurrent modulation and, subsequently, lower THz radiation power at a given laser intensity compared with a perfect spatial overlap of the laser modes. In the theoretical description of photomixing, the influence of the spatial overlap of the two laser modes on the generation of the THz radiation is taken into account by a factor 'm' in Eq. (3.3). Therefore, it is of importance to study how much the output intensity is modulated for the dual-mode operation of the BAL. In chapter 2, intensity autocorrelation measurements have been performed to prove the simultaneous oscillation of the two externally selected modes. In the present section, the degree of intensity modulation of the 2λ-ECBAL beam will be studied using an intensity autocorrelation method. The intensity modulation will be analyzed as a function of injection current of the laser and difference frequency of the two laser modes. It must be noted, however, that the investigations using an autocorrelator give only a rough estimate for intensity modulation because the device is difficult to align and the intensity autocorrelation is sensitive to alignment of the device.

The antenna-photocurrents rapidly modulated with the THz frequency cannot be measured by electronic methods. Hence, the AC component of the photocurrents which is responsible for the generation of the THz radiation cannot be determined electrically. However, since the relation between the DC photocurrent of the antennas and the time-averaged incident optical power onto the antenna is linear, the degree of the photocurrent modulation can be estimated by investigating the intensity modulation of the laser beam. As discussed in chapter 2, a method to study the intensity modulation is the measurement of the intensity autocorrelation $A(\tau)$ between a beam with an intensity $I(t)$ at time t and a time-delayed beam with an intensity $I(t-\tau)$ at time $t-\tau$. The intensity autocorrelation measurement then monitors the autocorrelation trace which exhibits a signal $A(\tau)$ as a function of the time-delay τ. For a collinear (i.e., two beams are completely overlapping) autocorrelator which is used for the present investigation, the detected signal $A(\tau)$ can be expressed as [136]

$$A(\tau) = 2\int I^2 dt + 4\int I(t)I(t-\tau)dt, \tag{5.1}$$

where both beams are assumed to have equal intensity. The first term on the right-hand side of Eq. (5.1) gives the averaged intensity independent of the time-delay τ, which has not been considered in Eq. (2.9). This term constitutes the background. The second term on the right-hand side of Eq. (5.1) gives the required intensity autocorrelation

function. The measurement resulting in $A(\tau)$ of Eq. (5.1) is generally referred to as the intensity autocorrelation with background [136].

When the intensity $I(t) = I_1 + I_2 + 2\sqrt{I_1 I_2}\cos\omega t$ for the dual-mode emission modulated with a beat frequency of ω is inserted in Eq. (5.1), the signal $A(\tau)$ can be expressed in terms of I_1, I_2 and τ as

$$A(\tau) = 6(I_1 + I_2)^2 + 4I_1 I_2(1 + 2\cos\omega\tau). \tag{5.2}$$

From the autocorrelation measurement, the maximum signal $A(\tau = 2\pi n/\omega)$ and minimum signal $A(\tau = (2n+1)\pi/\omega)$ can be determined, where n is an integer. Then, the quantities $I_1 + I_2$ and $2\sqrt{I_1 I_2}$ can be calculated from Eq. (5.2). As a consequence, the maximum intensity $I_{max} = I_1 + I_2 + 2\sqrt{I_1 I_2}$ and the minimum intensity $I_{min} = I_1 + I_2 - 2\sqrt{I_1 I_2}$ can be obtained from the autocorrelation measurements.

From I_{max} and I_{min}, two quantities can be determined to describe the intensity modulation of the dual-mode emission: modulation depth and contrast. The ratio of the modulated intensity to the maximum intensity is described by a modulation depth M_d defined as

$$M_d = \frac{I_{max} - I_{min}}{I_{max}}. \tag{5.3}$$

This ratio gives the actual fraction of the intensity modulation to the given maximum intensity. Hence, M_d indicates the fraction of the optical intensity that actually generates the AC component of the photocurrents. For a perfect intensity modulation, M_d is equal to 1. In comparison to M_d, the contrast C_I of the intensity modulation is defined as

$$C_I = \frac{I_{max} - I_{min}}{I_{max} + I_{min}}. \tag{5.4}$$

C_I gives eventually the degree of the interference of the two laser modes. C_I indicates the ratio of the achieved intensity modulation to the ideally achievable case, for which the two laser modes have equal power and the total intensity is perfectly modulated with a value of $C_I = 1$.

Figure 5.11 shows an intensity autocorrelation trace of the dual-mode emission of the BAL as a function of the time-delay τ. The difference frequency of the two laser modes is 226 GHz. The autocorrelation trace exhibits a sinusoidal behavior with a period of 4.6 ps. This period is in good agreement with the period of 4.4 ps corresponding to

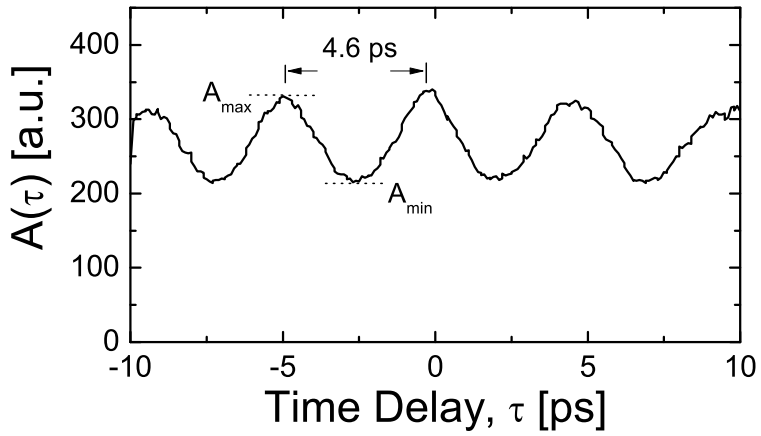

Fig. 5.11: Intensity autocorrelation signal A_τ as a function of time-delay τ for the dual-mode emission with a difference frequency of 226 GHz. $A_{\max}$ and $A_{\min}$ are the maximum and minimum signals, respectively.

the difference frequency of the two laser modes. The slightly higher signal $A(\tau = 0)$ is due to the constructive interference of all noisy optical signals incident into the autocorrelator at a time-delay of zero.

With the intensity autocorrelation measurements, M_d and C_I have been investigated as a function of the injection current of the laser at a constant difference frequency of 388 GHz. The range of the injection current is chosen between 180 and 265 mA, where two longitudinal modes can be easily selected in the external cavities without additional oscillation of the solitary laser modes. Fig. 5.12(a) depicts the investigated M_d and C_I as a function of the injection current. M_d and C_I exhibit a nearly constant behavior over the studied current range. M_d is around or larger than 0.9. Therefore, the photocurrent of the photomixer has the same ratio between the AC component and the maximum photocurrent. C_I exhibits a value larger than approximately 85 % of the ideal case. These results indicate that the realized 2λ-ECBAL exhibits constant and high intensity modulation over wide injection currents. In particular, the constant performance of M_d and C_I with increasing injection current is an unexpected result because the number of lateral modes of BALs generally increases with increasing injection current [127] and the spatial overlap of the two externally selected modes would decrease.

In addition, the investigations of M_d and C_I as a function of the detuning frequency of the two laser modes give insight into the performance of 2λ-ECBAL with the detuning frequency. Therefore, M_d and C_I have been investigated as a function of difference frequency of the two laser modes between 100 and 800 GHz. Here, the laser is driven with a constant injection current of 218 mA ($1.45 I_{th}$). The resulting M_d and C_I are displayed in Fig. 5.12(b). At difference frequencies below 400 GHz, M_d and C_I exhibit

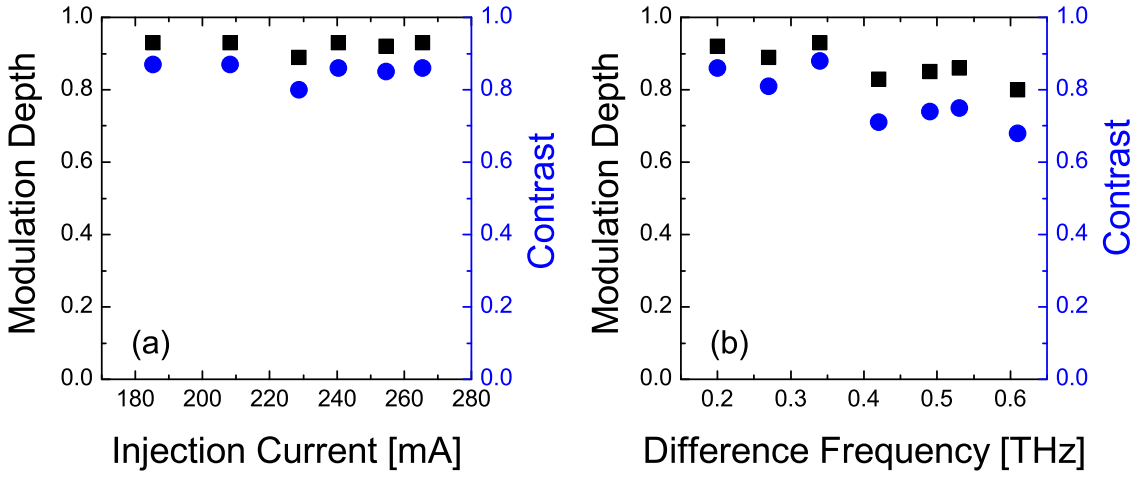

Fig. 5.12: Intensity modulation depth (full square) and contrast (full circle) as a function of injection current (a) at a constant difference frequency of 388 GHz and as a function of difference frequency of the two laser modes (b) at a constant injection current of 218 mA.

about 0.9 and 0.85, respectively. Above 400 GHz, M_d and C_I exhibit slightly lower values of about 0.85 and 0.75, respectively. This result indicates that the intensity modulation of dual-mode emission of the 2λ-ECBAL is almost constant with the detuning frequency of the laser modes at a constant injection current.

Hence, the results presented in this section show that the dual-mode emission of the 2λ-ECBAL exhibits constant and high intensity modulation over wide spectral and injection current ranges. Only the smaller C_I exhibiting about 75 % of the ideal case might be one reason for the lower conversion efficiency of the THz generation compared to the expectation discussed in section 5.2.2. However, still the achieved M_d and C_I for dual-mode operation of the 2λ-ECBAL over wide injection current and detuning frequency indicate that 2λ-ECBALs are promising high power laser sources for generation of high power THz radiation via photomixing.

5.4 Summary

In this chapter, frequency-tunable dual-mode emission has been realized using a BAL in an external Littman-double-cavity configuration. Methods for not only spectrally but also spatially filtered feedback have been employed in the configuration. Thereby, laterally and longitudinally single-mode emission of each of the two laser modes has been realized at an output power of 90 mW. The difference frequency of the two modes

can be varied between 0.1 and 1 THz. At high injection currents, the output power could be achieved up to 220 mW. However, at such high powers several longitudinal and lateral modes oscillate in each of the two externally excited peaks. The limitation of the detuning frequency to 1 THz is due to the simultaneous oscillation of solitary laser modes induced by the residual facet-reflectivity of the used BAL. By using a BAL with an antireflection coated facet, detuning frequency of the dual-mode emission could be achieved to about 3 THz. Moreover, using the intensity autocorrelation measurements, the intensity modulation of the dual-mode beam of the BAL could be estimated. The intensity modulation depth and the intensity contrast exhibit a constant performance independent of the injection currents and the detuning frequency. The intensity modulation depth which gives the ratio of AC photocurrents to the total photocurrents amounts to more than 85 %. The contrast of the intensity modulation which gives the ratio of the real modulation to the ideally achievable modulation amounts to more than 75 %. Furthermore, the generation of the THz radiation has been performed using a 2λ-ECBAL which does not employ the principle of spatially filtered feedback. The detected THz radiation power amounts to about 19 pW at an optical power of about 23 mW. The power of the THz radiation could be increased by improving its coupling efficiency into free space using a Si lens. The high intensity modulation and the improved emission characteristics of the spectrally and spatially controlled 2λ-ECBAL indicate that these devices are promising laser sources for the generation of high-power THz radiation via photomixing.

Chapter 6

Highly Nondegenerate Four-Wave Mixing and Direct THz Emission

In the previous chapters experimental realization of dual-mode semiconductor lasers and its successful application for THz wave generation by subsequent photomixing on antenna structures has been reported. However, even semiconductor lasers themselves are characterized by ultrafast optical nonlinear processes that affect their spectral and dynamic properties. Therefore, the simultaneous dual-mode emission in semiconductor lasers also gives rise to nonlinear optical process, in particular intracavity nondegenerate four-wave mixing (NDFWM[1]). The NDFWM process, originating from the interaction of the optical field with the semiconductor medium, is relevant for potential application like the generation of phase conjugate waves or optical switching, wavelength conversion for wavelength division multiplexing [137] and fiber dispersion-compensation [138] in optical communication systems. It also provides the possibility for spectroscopic methods in the frequency-domain for the study of ultrafast carrier dynamics in active semiconductor devices, corresponding to the pump-and-probe method in time-domain [139]. Furthermore, the nonlinear optical processes in the semiconductor laser itself indicate a possibility of a direct generation of THz radiation in semiconductor lasers without any need of external mixing devices.

In the present chapter, highly nondegenerate four-wave mixing (HNDFWM) in a tunable dual-mode semiconductor laser (SL) is experimentally investigated in which the fundamental interacting waves are two lasing modes selected by an external double Littman-Metcalf cavity configuration. After a short introduction to nonlinear optical phenomena and mechanisms underlying NDFWM in SLs, the conversion efficiencies, which describe the NDFWM process, as a function of the optical power and the detuning frequencies are discussed. Finally, the direct THz emission from a dual-mode SL is investigated.

[1]In several publications, NDFWM is used to denote nearly degenerate four-wave mixing. In this work, NDFWM denotes nondegenerate four-wave mixing.

6.1 Highly Nondegenerate Four-Wave Mixing

6.1.1 Nonlinear Optical Phenomena and Four-Wave Mixing

Since the invention of the laser and the first experimental second-harmonic generation in 1961 [140], the field of nonlinear optics became a subject of great interest in modern science. Nonlinear optics deals with phenomena of nonlinear interaction of light with a medium which occur when the sufficiently intense light propagates though the medium. In the familiar linear optics, which deals with optical phenomena occurring at the relatively low light intensity, optical properties of the medium are independent of the propagating intensity of the light, and the different light waves propagate through the medium without interaction with each other. If the light intensity is sufficiently high, the medium responds nonlinearly to the light field and the optical properties of the medium depend on the light intensity. Furthermore, the light waves propagating through the medium can also interact with each other via the medium.

As known from the theory of electromagnetic waves in media, light interacts with a medium through which it propagates by inducing a polarization in the medium. Optical properties of the medium are then described by the relation between the electric field $\mathbf{E}(t)$ of the traveling optical waves and the induced polarization $\mathbf{P}(t)$. This relation is governed by the characteristics of the medium, and if this relation is nonlinear, optical properties of the medium are said to be nonlinear. For not too high intensities, the polarization $\mathbf{P}$ can be expanded into a power series with respect to the optical field strength $\mathbf{E}$ in the form

$$\mathbf{P} = \epsilon_0(\chi^{(1)}\mathbf{E} + \chi^{(2)}\mathbf{E}^2 + \chi^{(3)}\mathbf{E}^3 + \cdots) = \mathbf{P}_L + \mathbf{P}_{NL}, \tag{6.1}$$

where ϵ_0 is the electric permittivity of free space and $\chi^{(n)}$ denotes the nth-order optical susceptibility of the medium which depends on the frequencies of the traveling optical waves. The polarization can be written as the sum of a linear $\mathbf{P}_L \equiv \epsilon_0\chi^{(1)}\mathbf{E}$ and a nonlinear part $\mathbf{P}_{NL} \equiv \epsilon_0 \sum_{n\geq 2} \chi^{(n)}\mathbf{E}^n$. These linear and nonlinear susceptibilities characterize the optical properties of the medium. The first term $\mathbf{P}_L$ describes the familiar linear optical phenomena and the second term $\mathbf{P}_{NL}$ is responsible for the nonlinear response of the medium.

The propagation of an electromagnetic wave in a medium is governed by the wave equation which is derived from the Maxwell's equations:

$$\nabla^2\mathbf{E} - \frac{1}{c^2}\frac{\partial^2\mathbf{E}}{\partial t^2} = -\mu_0\frac{\partial^2\mathbf{P}_{NL}}{\partial t^2}, \tag{6.2}$$

where c denotes the wave velocity in the medium and μ_0 is the free space magnetic permeability. This equation shows that the time-varying nonlinear polarization acts as a source of the electromagnetic field. Because $\mathbf{P}_{NL}$ is a nonlinear function of $\mathbf{E}$, new components of the electromagnetic filed are created, which were not present in the original light field. Thus, the description of the nonlinear polarization via an expansion in $\mathbf{E}$ provides insight into the nonlinear optical phenomena. Some nonlinear optical effects are discussed at the following. The second-order nonlinear optical interaction $\mathbf{P}^{(2)} \equiv \epsilon_0 \chi^{(2)} \mathbf{E}^2$ can take place in noncentrosymmetric media, that is, media which do not display inversion symmetry, and gives rise to effects like optical rectification, second-harmonic generation, generation of sum and difference frequencies, Pockels effect, and parametric amplification. The third-order nonlinear optical interaction $\mathbf{P}^{(3)} \equiv \epsilon_0 \chi^{(3)} \mathbf{E}^3$ can occur in all media, with or without inversion symmetry. It gives rise to effects like third-harmonic generation, Kerr effect, self-focusing, self-phase modulation, phase conjugation, and four-wave mixing (FWM). Higher order nonlinear optical interactions give rise to higher harmonic generations. All these effects are caused by refractive index change of the medium depending on the intensity of the incident light. Because the present work is about FWM phenomena in SL, the following description deals, thus, only with the FWM process in SL. For the general treatment about various nonlinear phenomena it is referred to Ref. [141].

Four-wave mixing refers to the nonlinear optical process in which four optical waves interact with each other in the medium. It is governed by the third-order nonlinear susceptibility $\chi^{(3)}$. If the incident light can be expressed as a group of monochromatic plane waves $\mathbf{E}(t) = \sum_{l=1}^{3} \mathbf{E}(\omega_l) e^{-i\omega_l t}$ with angular frequency ω_l and the corresponding electric filed $\mathbf{E}(\omega_l)$, the induced nonlinear polarization contributing to the FWM process $\mathbf{P}^{FWM}$ can be expressed in the frequency-domain by the relation [141]

$$P_i^{FWM}(\omega_s) = \epsilon_0 \sum_{j,k,l} \chi_{ijkl}^{(3)}(\omega_s) E_j(\omega_p) E_k(\omega_q) E_l^*(\omega_r), \tag{6.3}$$

where the indices i, j, k, l denote the cartesian components of the fields and $\omega_s = \omega_p + \omega_q - \omega_r$ must be satisfied due to the energy conservation. A new wave $\mathbf{E}(\omega_s)$ is then generated with phase conjugate properties with respect to $\mathbf{E}(\omega_r)$. These four waves are coupled by the wave equation (6.2). Two cases of FWM are often distinguished: degenerate four-wave mixing (DFWM) and nondegenerate four-wave mixing (NDFWM). Whereas all waves have the same frequency for DFWM, which is a special case of NDFWM, at least one of the incident waves has a different frequency in the case of NDFWM.

The NDFWM process can be easily understood by the following physical interpretation. For conventional NDFWM investigations in SL, in general, two primary optical waves

at frequencies ω_p and ω_q co-propagating in the active semiconductor medium induce a variation of the intensity of the optical field at the difference frequency $\Delta\omega = \omega_p - \omega_q$ of the two waves. This results in a modulation of the gain and refractive index of the medium at $\Delta\omega$, which generates dynamic gain and index gratings. The primary waves are then scattered by the resulting dynamic gratings, and the new waves are generated at frequencies $\Delta\omega$ apart on either side of the primary frequencies. In other words, the modulation of the medium induces sidebands on the primary waves, which fall at $\omega_p \pm \Delta\omega$ and $\omega_q \pm \Delta\omega$. In the photon picture FWM can be described as that two photons of pump wave at the frequency of ω_p are annihilated to create two new photons at the frequencies of $\omega_p + \Delta\omega$ and $\omega_p - \Delta\omega$. Likewise, two photons of probe wave at the frequency of ω_q transfer to two photons at the frequencies of $\omega_q + \Delta\omega$ and $\omega_q - \Delta\omega$. The mechanisms which are responsible for the generation of gain and index grating in SL are described in the following section.

6.1.2 Mechanisms of NDFWM in Semiconductor Lasers

In the past decades, the nonlinear mechanisms contributing to the NDFWM in the SLs have been studied theoretically and experimentally by many groups [142, 143, 144, 145, 146, 147, 148, 149] and have been identified as carrier density pulsation, carrier heating, spectral hole burning, and supplementary in quantum well structures also carrier capture and escape. To describe NDFWM phenomena depending on detuning frequency, it is indispensable to introduce the underlying mechanisms which can be classified into interband and intraband dynamics in SLs.

For detuning frequencies below tens of Gigahertz, the carrier density is easily modulated at the beating frequency of two primary waves. This carrier density pulsation (CDP) causes pulsations of the refractive index and the gain. This process results in the generation of new waves. CDP is induced by stimulated electron-hole recombination. Such interband process takes place on a time scale determined by the recombination lifetime τ_s, which is on the order of typically several hundred picoseconds. At detuning frequencies much higher than τ_s^{-1}, exceeding several tens of Gigahertz, the carrier density is not able to respond to the modulation at beat frequencies of the primary waves. The refractive index and gain gratings resulting from CDP become then ineffective and the efficiency of NDFWM drops off rapidly with further increase of detuning frequency.

Instead, for detuning frequencies exceeding 100 GHz, intraband mechanisms such as carrier heating (CH) and spectral hole burning (SHB) begin to play a dominant role in contributing to NDFWM. Population pulsations caused by intraband dynamics do not correspond to actual modulation of the total carrier density but rather refer to

modulation of the carrier distribution within the band. Such intraband population pulsations also result in gain and index gratings and lead to efficient NDFWM.

Carrier heating [150] is the increase of carrier distributions above the lattice temperature arising mainly from stimulated recombination and free-carrier absorption. By stimulated recombination, cold carriers close to the band edge are removed from the band. Free-carrier absorption transfers carriers to higher energies in the band. Both processes increase the temperature of the carriers higher than the lattice temperature. The heated carrier distributions relax to the lattice temperature by carrier-LO phonon scattering with a lifetime of $\tau_{ch} \sim 0.5 - 1\,\mathrm{ps}$. Modulation of the carrier temperature by beating of primary waves results also in index and gain gratings.

Another intraband mechanism of population pulsations contributing to NDFWM for detuning frequencies exceeding several hundred GHz is spectral hole burning. SHB is a formation of a dip in the gain spectrum of the SL due to stimulated recombination [151]. An intense light field propagating in the SL reduces the occupation probability of carriers at the electronic state resonantly interacting with the propagating light field within a conduction band. This process thus gives rise to a reduction in the gain spectrum. The intraband process such as carrier-carrier scattering occurring at a time scale of $\tau_{hb} \sim 50 - 100\,\mathrm{fs}$, restores the perturbed distributions to quasi-Fermi distribution. The modulation of the dip in the gain spectrum by beating of the primary waves in turn creates the gain and index gratings. Since SHB is governed by the fast intraband relaxation process, it is expected to observe effective NDFWM for detuning frequencies even exceeding 1 THz.

Since intraband processes are faster than interband processes, the gain and index change related to them is also much smaller, and their contributions to NDFWM have a small efficiency. However, small intraband relaxation times imply that the bandwidth of intraband contributions will be very large, easily exceeding 1 THz. In general, both the interband and the intraband population pulsations should be considered to describe NDFWM accurately. All these mechanisms contribute to NDFWM via $\chi^{(3)}$, which can be thereby expressed as the sum of that of each mechanism as

$$\chi^{(3)} = \chi^{(3)}_{CDP} + \chi^{(3)}_{CH} + \chi^{(3)}_{SHB}, \tag{6.4}$$

where $\chi^{(3)}_{CDP}$, $\chi^{(3)}_{CH}$ and $\chi^{(3)}_{SHB}$ denote the 3rd-order susceptibilities associated with CDP, CH and SHB, respectively [147, 152]. However, depending on the range of detuning frequency, the analysis can be simplified to either interband effect or including intraband effects.

So far, most of the previous studies on NDFWM in semiconductor lasers and semiconductor optical amplifiers (SOAs) have been performed either by injecting an external

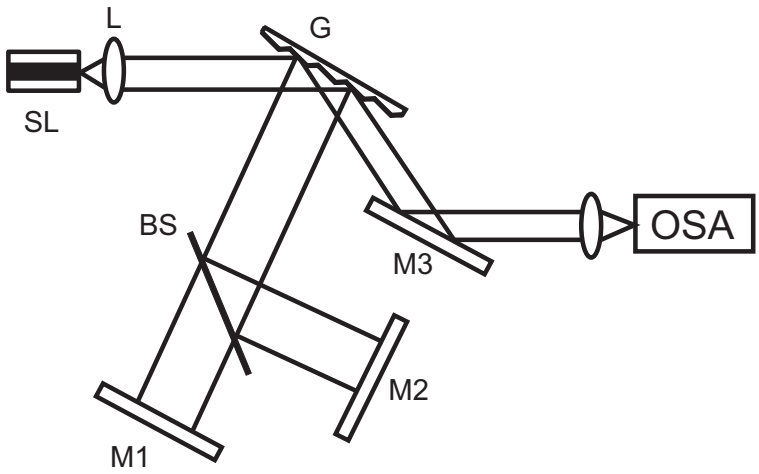

Fig. 6.1: Experimental setup. SL: laser diode; L: aspheric lens; G: grating; BS: beam splitter; M1, M2: external mirrors; M3: mirror for output coupling; OSA: optical spectrum analyzer.

pump and an external probe wave into the active layer of an amplifier structure or by using one inherent lasing mode inside the laser as the pump wave and injecting only one external probe wave into the cavity [144, 153, 154, 155]. NDFWM in a tunable dual-mode laser has not yet been studied systematically. The previous studies on NDFWM also have been performed by a strong pump wave and a weak probe wave. In the present study, most NDFWM has been performed with the condition that both pump and probe waves are of the same intensities.

6.1.3 Experimental Setup

In chapter 2, it has been demonstrated that dual-mode operation in SL induces FWM signals at detuning frequencies of two laser modes in the THz range. In order to gain a better understanding of the underlying mechanisms responsible for the FWM phenomenon, HNDFWM in SL will be investigated in this chapter.

HNDFWM [156] has been studied in a commercial MQW GaAlAs SL (Hitachi HL7851G) operating at 785 nm and providing a maximum output power of 50 mW. The laser has a high-reflective rear facet and a low-reflective front facet. The laser is driven at an injection current of $I_{inj} = 4I_{th}$ ($I_{th} = 43\,mA$) and the temperature is stabilized at room temperature. For clearness for FWM-experiments, figure 6.1 reviews the experimental setup shown in chapter 2 for the tunable dual-mode operation of the laser which is realized by spectrally filtered optical feedback from an external double-cavity configuration. The laser system consists of the SL, a collimating optics, a diffraction

grating (1200 grooves/mm), a 50/50 beam splitter and two external mirrors. The laser beam from the front facet is collimated by an antireflection-coated aspheric lens and is incident on the diffraction grating, which is used for spectral selection. The first-order diffraction beam of the grating is coupled into the external double-cavity with a length of 40 cm. The beam is divided into two beams by a beam splitter. Within each branch, the desired wavelength is selected via tilting the external mirror which also controls the feedback strength. Consequently, the compound cavity system consists of the semiconductor laser resonator of length $L_{solitary} \approx 670\,\mu m$ and the external resonator. Therefore, the compound mode structure consists of the comb of the external cavity modes modulated by the solitary laser modes. The two modes, which satisfy both resonator conditions, can be tuned independently but only discontinuously over the whole gain bandwidth. The zeroth-order beam of the grating is used as output and is characterized using an optical spectrum analyzer with a resolution of 0.1 nm.

For the study of the efficiency of HNDFWM as a function of the frequency detuning we kept the wavelength of one mode at 784.6 nm fixed close to the gain maximum and changed the wavelength of the other mode within the gain regime. The definition of pump and probe wave is arbitrary because this experiment was carried out with the condition of equal optical powers of the two modes. Each mode can therefore be considered either as pump or probe wave. For convenience, the pump wave at f_p $(= \omega_p/2\pi)$ is defined here as the wave whose frequency is kept fixed close to the gain maximum and the wavelength of the probe wave at f_q $(= \omega_q/2\pi)$ is thereby varied in the gain region.

6.1.4 Four-Wave Mixing Spectra

Figure 6.2 shows optical spectra of the SL emission at detuning frequencies of 189 GHz and 443 GHz measured with the experimental setup of Fig. 6.1. The two fundamental frequencies and a cascade of newly generated frequencies $f_i = \omega_i/2\pi$ with corresponding power P_i can be recognized. In the present experiment, the two linearly TE-polarized fundamental waves are generated by lasing action inside the laser, as opposed to conventional injection of waves by external pumping. First, it is verified by autocorrelation measurement that the two fundamental modes are indeed emitted simultaneously. The simultaneous dual-mode operation of the laser p and q at frequencies f_p and f_q with a detuning frequency of $\Delta f = f_p - f_q = 189$ GHz results in the generation of new waves denoted as $c1$ and $c2$ at frequencies $f_{c1} = f_p + \Delta f$ and $f_{c2} = f_q - \Delta f$, respectively. The laser output exhibits the new waves only when both beams from the double-cavity are present, which has been confirmed by blocking one of the two mirrors. There also oscillate additional waves denoted by $c3$ and $c4$ at frequencies $f_{c3} = f_p + 2\Delta f$ and

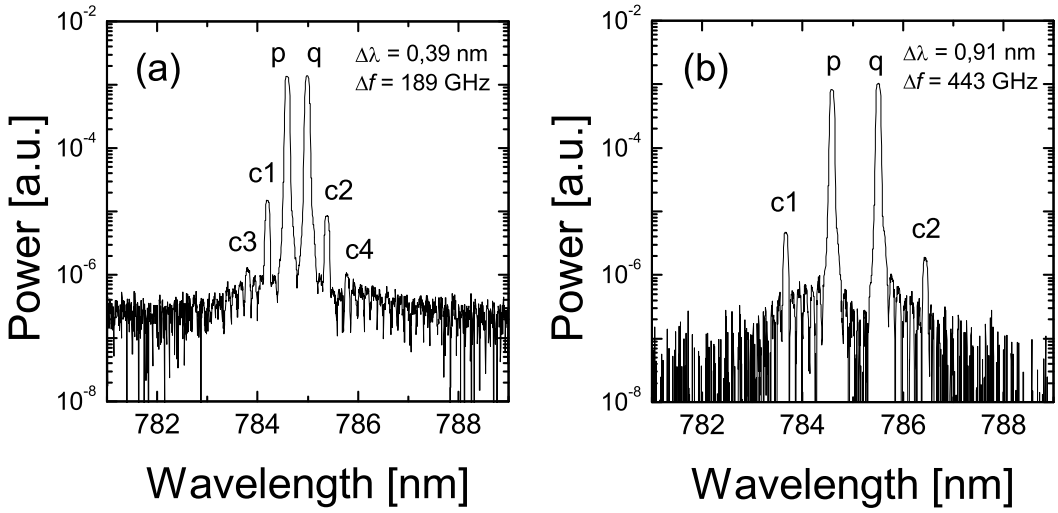

Fig. 6.2: Laser output spectra of FWM process at different detuning frequencies. A cascaded FWM process can be seen in diagram (a). p and q are the dual laser modes; $c1$, $c2$, $c3$ and $c4$ denote the newly generated waves.

$f_{c4} = f_q - 2\Delta f$. They can be explained by a cascaded FWM process [157] and result from the interaction of the newly generated waves at $f_p + \Delta f$ and $f_q - \Delta f$ with the primary waves at f_p and f_q, respectively. The newly generated frequencies are effectively amplified due to the fact that the high efficiency of the wave mixing process is within the gain bandwidth of the laser and are enhanced by the laser cavity resonance [153, 154, 155]. In general, for effective nonlinear optical processes, it is necessary to take into account phase-matching conditions. Due to dispersion, waves with different frequencies propagate with different velocities in the medium, which reduce the phase matching of the involved waves as a result. The efficiency of the NDFWM process at high detuning frequencies of pump and probe waves larger than 100 GHz is limited by the phase mismatch between the newly generated wave and the primary waves. For a given length L of the laser, the phase matching condition can be considered approximately fulfilled [147], if

$$\left|\frac{\partial n_g}{\partial \lambda}\right| \left(\frac{\Delta f}{f}\right)^2 L \ll 1, \tag{6.5}$$

where $\partial n_g/\partial\lambda = -\lambda\partial^2 n/\partial\lambda^2$ is the group index dispersion and λ is the wavelength of the waves in free-space. Using the value $\partial n_g/\partial\lambda \approx -3\,\mu m^{-1}$ [158], $L = 670\,\mu m$ and $\lambda = 785\,nm$ for the SL in this study, the restriction on the detuning frequency yields $\Delta f \ll 8.5\,\mathrm{THz}$. Thus, neglecting phase mismatching, which is justified in the present experiment, where the maximum detuning frequency is 1.2 THz, the FWM

performance can even be improved in the range of phase matching by increasing the interaction length due to reflection of the waves at the rear facet [159, 160].

6.1.5 Characteristics of HNDFWM depending on Detuning Frequencies

Studying HNDFWM at large detuning frequencies provides information on the characteristic mechanisms contributing to the nonlinear response of the medium to the optical field. One possibility to characterize the HNDFWM process is to determine the conversion efficiency extracted from the measured output power. From equation (6.3), the electric field $E(\omega_i)$ of the newly generated waves at frequencies $\omega_i \equiv 2\pi f_i$ is proportional to the induced medium polarization $P^{FWM}(\omega_i)$ at frequencies ω_i which is related by the third-order susceptibility $\chi^{(3)}(\omega_i)$ to the electric fields $E(\omega_j)$, $E(\omega_k)$, $E(\omega_l)$ according to

$$P^{FWM}(\omega_i) = \epsilon_0 \chi^{(3)}(\omega_i) E(\omega_j) E(\omega_k) E^*(\omega_l), \tag{6.6}$$

where the energy conservation $\omega_i = \omega_j + \omega_k - \omega_l$ has to be fulfilled. The subscripts denoting optical polarization direction are here omitted because all waves in the present investigation have the same optical polarization. The normalized conversion efficiency $\eta(\omega_i)$ is then defined by the relation [161]

$$P(\omega_i) = \eta(\omega_i) P(\omega_j) P(\omega_k) P(\omega_l), \tag{6.7}$$

where $P(\omega_i)$ is the output power of the newly generated wave, and $P(\omega_j), P(\omega_k), P(\omega_l)$ are output powers of the primary waves which can be directly determined from the experimentally measured output powers. The conversion efficiency $\eta(\omega_i)$ is proportional to the square of the susceptibility $\chi^{(3)}(\omega_i)$.

Figure 6.3 shows the normalized conversion efficiency of the FWM process obtained in the experiment depending on the detuning frequency $|\Delta f|$ from 100 GHz up to 1.2 THz for positive detuning ($\Delta f > 0$) and up to 890 GHz for negative detuning ($\Delta f < 0$). For even higher detuning frequencies the detectivity has been limited by noise. For positive detuning, η is nearly constant for detuning frequencies in the range of 150 GHz to about 500 GHz and decreases for further detuning. For negative detuning, η decreases up to about 400 GHz and increases again for higher detuning. It approaches a nearly constant value as the detuning frequency increases above 600 GHz. In Fig. 6.3(a) and Fig. 6.3(b), we observe a similar behavior of η for the newly generated

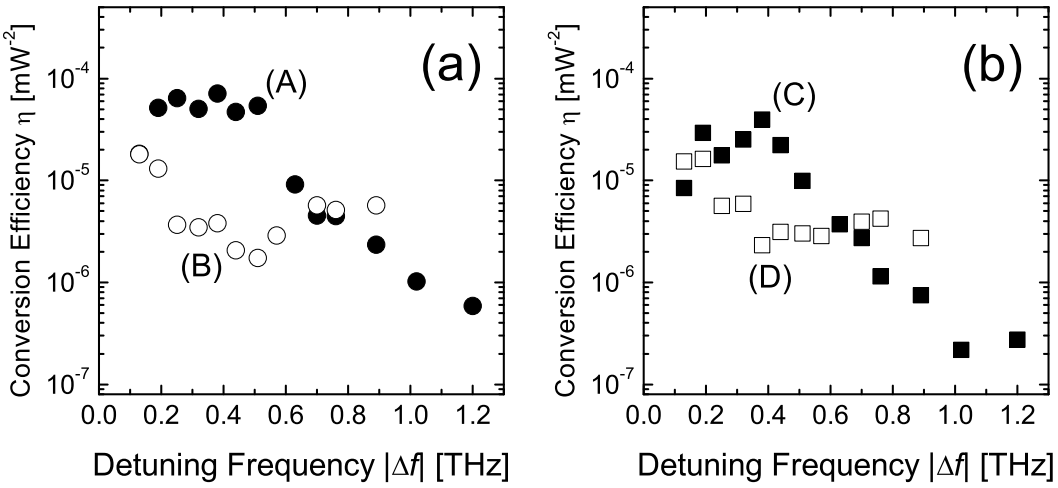

Fig. 6.3: Normalized conversion efficiency η depending on positive and negative detuning frequency. (a) $\eta_{c1} = P_{c1}/P_p^2 P_q$: (A) for positive detuning (full circle), (B) for negative detuning (open circle); (b) $\eta_{c2} = P_{c2}/P_p P_q^2$: (C) for positive detuning (full square), (D) for negative detuning (open square).

waves at frequencies $f_{c1} = f_p + \Delta f$ and $f_{c2} = f_q - \Delta f$, respectively. However, in both images, there is an asymmetry of η with respect to positive and negative detuning (i.e. (A) vs. (B) in Fig. 6.3(a), (C) vs. (D) in Fig. 6.3(b), respectively).

As mentioned in section 6.1.2, carrier density pulsations (CDP), exhibiting characteristic time scales of hundreds of picoseconds, are the dominant mechanism contributing to FWM at detuning frequencies below 100 GHz [147]. The generation of new waves at higher frequencies, where the carrier density can not be effectively modulated, implies other mechanisms that are able to respond to the high detuning frequency. In this regime, intraband processes such as carrier heating (CH) and spectral hole burning (SHB) are the dominant mechanisms, whose characteristic times are in the range of 100 fs - 1 ps. In particular, the observed asymmetry of the conversion efficiency between positive and negative detuning in Fig. 6.3 indicates that more than one mechanism is responsible for the behavior in this detuning range. We attribute this asymmetry to the interference of CDP, CH and SHB mechanisms [147, 162]. The interference between CDP and CH is almost symmetrical with respect to the sign of detuning, whereas CDP and CH interfere with SHB constructively for positive detuning and destructively for negative detuning. This interference between different mechanisms results in a less efficient conversion for negative detuning as compared to positive detuning as shown in Fig. 6.3(a).

It is worth noting from Fig. 6.3 that, although the two primary waves have almost

the same output power, the conversion efficiency of the lower frequency (C) is slightly smaller than that of the higher frequency (A) for positive detuning. In contrast, for negative detuning the two waves show nearly the same conversion efficiency ((B) and (D)), independent of frequency. This smaller conversion efficiency of the lower frequency (C) compared to (A) in the case of positive detuning can be explained as follows. On the one hand, the amplification of the new frequencies is different depending on their position within the gain curve. The frequency near to the gain maximum experiences more amplification than that further away from the maximum. On the other hand, depending on whether the pump wave lies in the vicinity of the gain peak or rather towards the band gap, either CH or SHB is dominant [163]. In the region of the band gap changes in carrier temperature hardly affect the carrier modulation, consequently the effect of CH is of less importance as the probe wave approaches lower frequencies. Here SHB is dominant. On the contrary, as the probe wave approaches higher frequencies, the effect of changes in carrier temperature is stronger and CH is present in addition to the SHB effect.

As the SL used in the present experiment has a MQW structure, even effects like carrier capture and escape have to be taken into account. However, a decisive identification of these effects is not possible from the present measurements, because all those mechanisms are simultaneously contributing to the FWM process.

6.1.6 Conversion Efficiency depending on Output Powers of Dual-Mode

In the dual-mode semiconductor laser, change of optical power of one mode is accompanied by changes of that of the other mode because they share the same gain medium. The optical power increase of one mode thus reduces the gain available for the other mode, which results in decreasing its optical power. However, it is not explicitly described in Eq. (6.7) whether the normalized conversion efficiency η of FWM depends on the total power and the relative power of the two primary modes with the condition of constant total power, respectively. It has been reported that FWM efficiency is dependent on the total power of the external source injected into the laser [143, 157]. Most of the previous studies on FWM efficiency have also been done under the conditions that the injection pump power has been varied keeping the probe power fixed [164], or both pump and probe powers have been varied keeping the ratio of the pump power to the probe power constant [159, 165]. In both cases, the total powers have been varied, which in turn resulted in the change of the conversion efficiency. However, there has not yet been reports on the behavior of conversion efficiency depending on the ratio of the pump power to the probe power keeping the total power constant. In the present

section the behaviors of conversion efficiency are investigated depending on relative power and total power of two primary lasing modes for dual-mode operation of a SL.

6.1.6.1 Relative Power Dependency of Conversion Efficiency

To study the influence of the relative power of the two primary modes on the normalized conversion efficiency, the same configuration as that of the previous section has been used. The injection current is held constant at 184 mA ($I_{inj} = 4.3I_{th}$). The measured total output power thereby amounts to 40 mW. As shown in the previous section, η is dependent on the difference frequency between both primary modes. To avoid the influence caused by frequency detuning on η, the spectral positions of both modes are fixed at a wavelength of 784.58 nm and 784.98 nm, respectively. The difference wavelength of $\Delta\lambda = 0.4$ nm is therefore kept fixed at a center wavelength of around 784.7 nm. This $\Delta\lambda$ corresponds to a difference frequency of $\Delta f = 195\,GHz$.

Relative power of both primary modes has been controlled via simultaneously controlling the feedback strength of the first-order diffraction beam of the grating within each branch of the external double-cavity via tilting the external mirrors. The zeroth order beam of the grating is coupled into an optical spectrum analyzer with a resolution of 0.1 nm to characterize the spectrum and a detector to control the constant total output power.

The primary waves have been chosen to lie in the range of gain maximum and the difference frequency is chosen in the region of the highest conversion efficiency obtained in the previous section. Because of efficient nonlinear optical processes and large amplification of newly generated waves under the chosen conditions, it makes the observation of FWM effective even at large power differencies of both primary waves.

Controlling the feedback strength of the primary waves via slightly tilting the external mirrors alters coupling efficiency of each wave into the laser. The relative power difference thus originates from the difference of coupling efficiency for each wave. If $f_{c1} > f_{c2}$ and the primary wave at the nearest frequency from the newly generated wave is defined as the pump wave, the wave at higher frequency f_p (i.e., shorter wavelength) is designated as the pump wave and the one at the lower f_q as the probe wave for the new wave at f_{c1}. In a similar way, for the new wave at f_{c2}, the primary waves at f_p and f_q are the probe and the pump waves, respectively.

Figure 6.4 depicts output power P_p of one primary wave as a function of output power P_q of the other primary wave measured by controlling the feedback strength of both waves. The increase of P_p accompanies a decrease of the same amount of P_q. The linear fit of the measured data shows the relation $P_p = 39\,mW - P_q$, which confirms

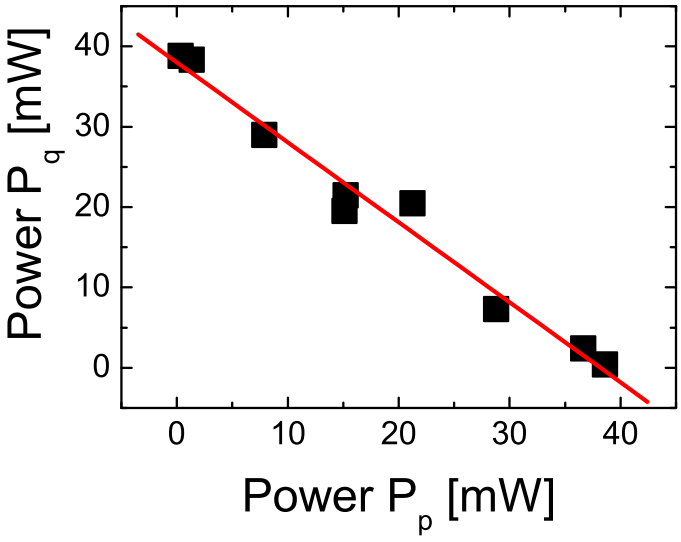

Fig. 6.4: Output power P_q of one primary wave as a function of output power P_p of the other primary wave: The full squares represent experimental data. The solid line is a linear fit to the data

constant total output power of both primary waves in the whole control regime. The small deviations of measured values may come from fluctuation of total output power originating from temperature fluctuations on long time scales, but lie within 7%.

The results of NDFWM depending on the power ratio $R_p = P_p/P_q$ of both primary waves are depicted in Figure 6.5. Fig. 6.5(a) shows output powers of the newly generated waves depending on the relative powers of the primary waves with the condition of constant total output power. Fig. 6.5(b) shows the corresponding conversion efficiency η obtained from the experimental data. The output powers of the FWM waves grow with increasing pump power relative to the probe power, approaching a maximum and then decrease with further increasing relative power. The maximum output powers P_{c1} and P_{c2} of the newly generated waves can be found at symmetrical points +6 dB and −6 dB away from $R_p = 1$, respectively. Furthermore P_{c2} is larger than P_{c1} over the whole R_p range. The behavior of conversion efficiency showing a maximum is expected from the equation (6.7). If η is independent of R_p and the same applies for both newly generated waves, the powers of new waves are the same and symmetrical about $R_p = 1$. Consequently, they should have their maximum located at +3 dB and −3 dB away from $R_p = 1$ for P_{c1} and P_{c2}, respectively. The difference between P_{c1} and P_{c2} in Fig. 6.5(a) might originate from the difference between the positions where the new waves are located in the gain spectrum. Although both primary waves at f_p and f_q are selected close to the gain maximum, the wave at f_q may still lie nearer to the gain

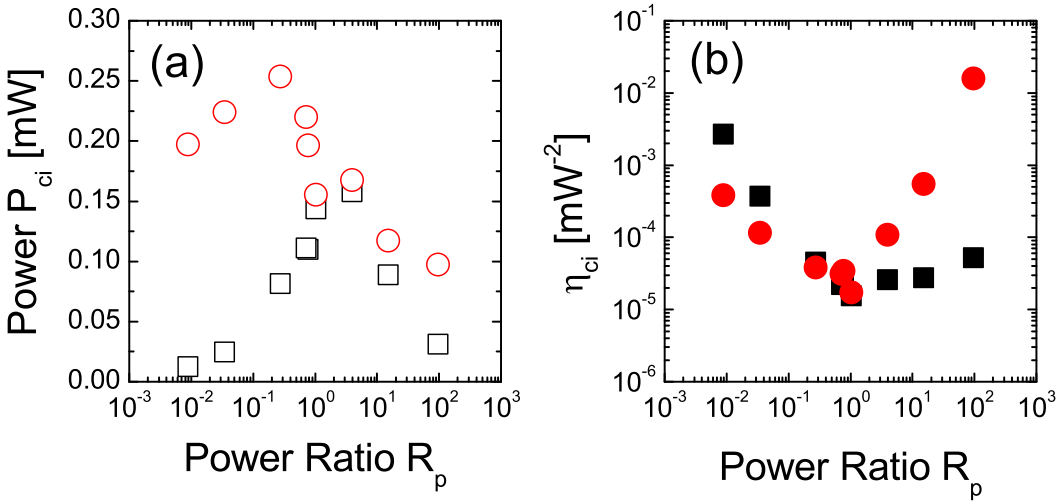

Fig. 6.5: (a) Power of newly generated waves: P_{c1} (open square) and P_{c2} (open circle); (b) Conversion efficiency depending on relative power of primary waves: $\eta_{c1} = P_{c1}/P_p^2 P_q$ (full square) and $\eta_{c2} = P_{c2}/P_p P_q^2$ (full circle)

maximum than the wave at f_p. A similar argument applies for the wave at f_{c2} and the wave at f_{c1}. Thus, the new wave at f_{c2} is amplified more than the new wave at f_{c1}.

Fig. 6.5(b) shows the behavior of η depending on the power ratio of the primary waves. With increasing R_p, i.e., increasing power P_p of the mode at f_p, which accompanies decreasing power P_q of the other mode at f_q, η_{c1} decreases for the wave at $f_{c1} = f_p - \Delta f$ steeply until the level of the same power of both primary waves and reaches a minimum. η_{c1} then increases slightly with further increase of R_p. The reverse behavior can be observed for the wave at $f_{c2} = f_p + \Delta f$, except that η_{c2} has more increasing tendency as R_p decreases in the range of $R_p < 1$ than η_{c1} as R_p increases in the range of $R_p > 1$. This more or less symmetrical behavior of the η's with respect to R_p is expected because the waves designated here by P_q and P_p are the pump and probe wave for the new wave at P_{c2}, respectively. However, it is noticeable that, contrary to symmetrical η's for both new waves where the pump power is smaller than the probe power, the η_{c1} and η_{c2} deviate from the symmetrical behavior for increasing pump power from $R_p = 1$ in each case. In the range of larger pump power than the probe ($P_p > P_q$), η_{c1} remains of the same order of magnitude; η_{c2}, on the contrary, increases strongly with increasing pump power relative to the probe ($P_p < P_q$) and is ten times larger than the minimum. This different behavior between η_{c1} and η_{c2} originates from the fact that the new wave at f_{c2} is stronger amplified than that at f_{c1}, as discussed above with respect to Fig. 6.5(a). It is also worth noting that there exists a minimum conversion efficiency for both new waves, which occurs at $R_p = 1$ and not at the minimum powers of the

new waves. Around this minimum the conversion efficiency remains of the same order of magnitude in the range of $|R_p| < 3\,\mathrm{dB}$.

The present investigations show that the power of the newly generated waves and the conversion efficiency are dependent on the relative power of the primary waves, given the condition that the total power remains constant. The new waves exhibit the maximum power at $R_p = \pm 6\,\mathrm{dB}$. The conversion efficiency shows a minimum when the pump power and the probe power are the same.

6.1.6.2 Total Power Dependence of Conversion Efficiency

Another interesting point is the dependence of η on total optical power of the pump and probe waves at constant wavelength difference. In the equation (6.7) η is assumed to be independent on the total optical power. However, it is even shown above that η is dependent on the relative power of both primary modes at constant injection current and has a minimum, provided that they have the same relative output power.

To examine the power dependence of η two methods can be used. It has been found in the investigation that the total optical power at the constant injection current depends on the positions of the modes in the gain spectrum of the laser. Changing the wavelength positions of the two oscillating modes within the gain range, while controlling the output power of both modes to be equal, leads to changes of the total output power. In this case the injected carrier density remains constant. Also, the total output power can be varied by varying the injection current into the laser such that the injected carrier density is changed. In order to examine the influence of total power on the conversion efficiency under constant injected carrier density, the former method has been chosen. The injection current is kept fixed at 184 mA. Keeping the difference wavelength fixed at $\Delta\lambda = \lambda_q - \lambda_p = 0.4\,\mathrm{nm}$, the pump ($\lambda_p$) and the prove ($\lambda_q$) wave are tuned from 784.56 nm to 787.36 nm.

The behavior of the total power of primary waves and η_{c1} and η_{c2} (with $f_{c1} > f_{c2}$) depending on the wavelength of oscillation is depicted in Fig. 6.6. While being tuned towards the longer wavelength region, the power of both modes increases up to 786.18 nm and remains more or less constant after that. In contrast, the η's for the newly generated waves both decrease and exhibit the same magnitude. It is obvious that η decreases with increasing total power of the primary waves. It is observed that as the primary waves are tuned to the longer wavelength, the new wave at f_{c2} which locates at the longest wavelength gets a smaller amplification due to the smaller gain. This causes smaller η_{c2} than η_{c1} in the longer wavelength range.

The decrease of η with increasing total power can be explained by considering the

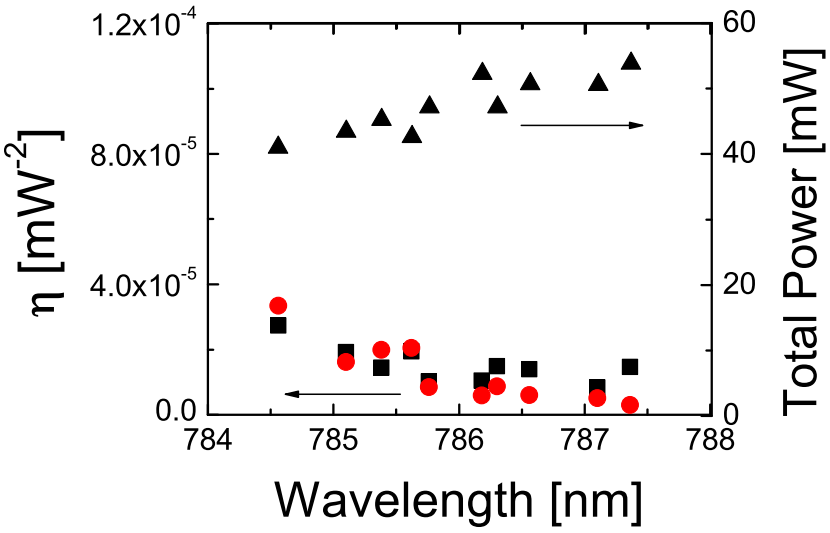

Fig. 6.6: Normalized conversion efficiency $\eta = P_{c1}/P_p^2 P_q$ (full square), $\eta = P_{c2}/P_p P_q^2$ (full circle) and total output (full triangle) of the dual laser modes depending on the wavelength of oscillation

mechanisms contributing to the NDFWM [157, 166]. The FWM process arises from the population pulsations and thus the efficiency of the nonlinear optical process depends on the static carrier density $(N-N_0)$ in the active layer of the laser [167], where N_0 is the carrier density for transparency. The static carrier density in the present experiment depends not only on injection current of the laser but also on the total intensity of the oscillating modes due to the stimulated recombination. Increasing total intensity at constant injection current reduces the free-carrier density in the active layer due to the stimulated recombination, which eventual results in reduction of the efficiency of FWM.

6.1.7 Summary

In the present chapter highly nondegenerate four-wave mixing in a tunable dual-mode semiconductor laser is presented which has been realized by spectrally filtered optical feedback from an external double-cavity configuration. The experiment has been performed using a multiple quantum well (MQW) GaAlAs laser. The simultaneous oscillation of two modes in the laser medium induces the cascaded generation of new waves. Both laser modes and the newly generated waves have been chosen resonant with the solitary laser cavity mode. The newly generated waves are thus enhanced due to cavity resonances of the solitary laser. By tuning the frequency difference between

the two modes up to 1.2 THz, the conversion efficiency depending on the detuning frequency has been investigated. It decreases with increasing detuning frequency and its asymmetric dependence on positive and negative detuning shows that ultrafast carrier dynamics such as carrier heating and spectral hole burning are responsible for the nonlinear optical process in the detuning range of several hundred GHz. Since both modes share the same gain medium, an increase in power of one mode accompanies a decrease in that of the other mode. This relation limits the generated powers of new waves. The maximum power of the newly generated waves is reached when the power ratio of both mode is about ±6 dB. It has also been found out that the conversion efficiency has a minimum when both modes have equal power. Furthermore, the conversion efficiency decreases as total optical power increases. It is attributed to the reduction of the free-carrier density due to the stimulated recombination. Further quantitative studies such as spatially resolved streak-camera investigations should give more detailed insight into the dynamics of the simultaneous dual-mode operation in the semiconductor laser.

6.2 Investigation to Direct THz Emission from a Semiconductor Laser

The generation of THz radiation using SL and external photomixing allows a compact and cost-effective THz source. Still, the photomixing method has limitations and complexities arising from the external photomixing device. The accessible operation frequency is limited by the photoconductive materials and the antenna characteristics. The possible thermal damage of the photomixer limits the operation condition. Furthermore, the alignment of the optical beam incident on the photomixer is crucial for an effective generation of THz radiation. Therefore, the most desirable way to generate THz radiation is to realize a THz source which directly emits THz radiation without any help of external components. An important achievement in recent THz technology is the realization of THz lasers in which THz waves are generated based on intersubband transitions in a semiconductor material [21]. However, such THz sources operate so far only at cryogenic temperatures. Furthermore, their limited frequency tunability is another drawback for the application to spectroscopy. Recently, it has been reported that THz waves can be directly generated in a dual-mode semiconductor laser operating at room-temperature [168]. This would allow a possibility to exclude the external photomixing device, provided that the THz radiation is emitted with an output power comparable to that of the photomixing system.

The four-wave mixing phenomenon in a dual-mode semiconductor laser has been extensively studied in the previous section. It has been attributed to a modulation of

the carrier distribution through carrier density pulsations, carrier heating and spectral hole burning in the SL caused by the beating of two participating modes. The modulation of the carrier distribution in the THz frequency range is of particular interest because it might also act as a radiation source of the difference frequency according to Maxwell's wave equation [169, 170]. The SL would then emit direct THz radiation as a THz source. In order to explore this possibility, the direct THz emission from a dual-mode SL is investigated in the next section.

6.2.1 Experimental Setup

The experimental setup for detection of direct THz emission from the dual-mode SL is shown in Fig. 6.7. The scheme to generate dual-mode emission in a SL is the same as that described in chapter 2. As an optical source, a BAL (FBH) with a center wavelength of 803 nm and a stripe width of 60 μm is employed in the Double-Littman-Configuration. The laser emits TM-polarized light with an output power of up to 670 mW at an injection current of 1 A. In the present investigation, the laser is driven at an injection current of 491 mA. The corresponding optical power of the laser amounts to 160 mW. The temperature of the laser is stabilized at room temperature. The laser front facet having a reflectivity of 5 % is coupled to the external double cavity configuration where desired wavelengths are selected. The zeroth order beam of the grating is used to monitor the optical spectrum of the laser light by an OSA. To detect the THz signal emerging from the SL, an InSb bolometer (QMC Instruments) is placed directly at the rear facet of the laser having a reflectivity of 90 %. The bolometer has a limited detection bandwidth with a maximum frequency of 1.6 THz. Its entrance window consists of PE-material. The detected signal is amplified by a preamplifier within the bolometer with a gain of 1000. In order to detect the THz signal using lock-in technique, a mechanical chopper is inserted in one of the external cavities. The light propagating in this external cavity is chopped with a frequency of 173 Hz. The light propagating in the other external cavity is fed back to the laser for the case of dual-mode operation and blocked by an absorber for the case of single-mode operation. In that way, the signals emerging from the SL under the dual-mode and single-mode operation can be detected for comparison. To analyze the THz radiation emerging from the SL, either a bandpass filter with a frequency pass range between 150 GHz and 375 GHz or a wire-gride THz polarizer is placed between the SL and the bolometer at a position designated by P in Fig. 6.7. Although the bolometer has a PE-window at the entrance, some optical light emerging from the rear facet of the laser reaches the bolometer detection element. If the collimated beam from the facet is directed towards the entrance of the bolometer placed at a distance of 50 cm from the SL, the bolometer responds to the optical beam. The response to the optical wavelength raises

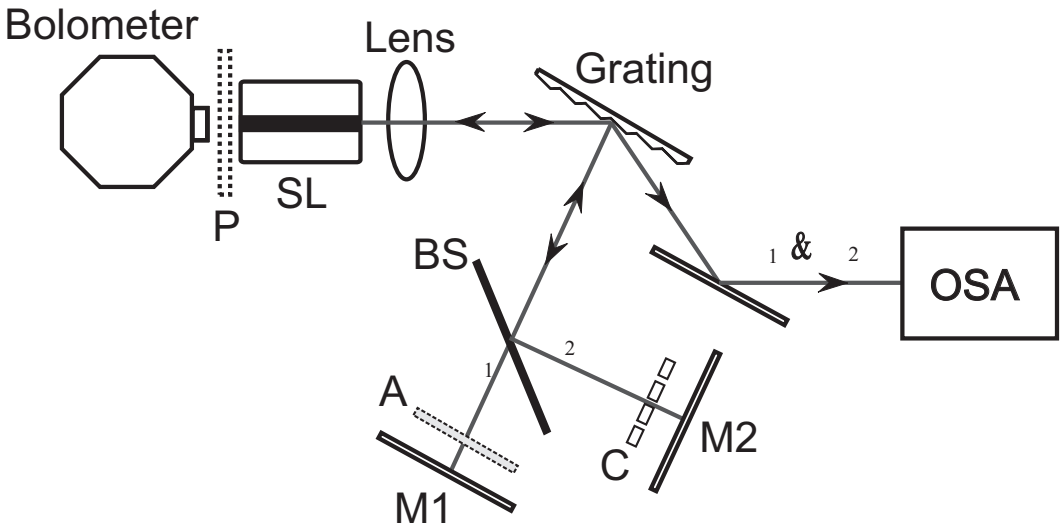

Fig. 6.7: Experimental setup for detection of direct THz emission from the dual-mode SL. BS: beam splitter, A: beam absorber, C: chopper, M1 and M2: Mirrors, P: polarizer or bandpass filter

the background of the detection and limits particularly the sensitive detection of the small signals which lie at the detection limit of the bolometer. Effective methods to circumvent this problem still remain a task to be solved.

6.2.2 Results and Discussion

The dependance of the generated signal as a function of the difference frequency of the laser modes is depicted in Fig. 6.8(a). Starting at 500 GHz the signal increases with an increase in the difference frequency and shows a peak value of 63 μV at a frequency of about 1 THz. A further increase in the difference frequency above 1 THz results in a decrease of the signal down to the noise level of 5.9 μV reached at 1.63 THz. At higher difference frequencies no signal is identified from the lock-in detection. Thus, the result shows a resonant behavior of the signal generation depending on the difference frequency. For comparison, the signal generated at a single-mode operation is also investigated. In Fig. 6.8(a), few representative points are depicted for the signals detected at the single-mode operation. For the whole frequency range, the detected signals lie at a constant level of 20 μV independent of the frequency. The signals generated in the dual-mode operation are higher than that under single-mode operation for all difference frequency below 1.64 THz. At 1.64 THz, it is found that the signal for the single-mode operation is higher than that of the dual-mode operation. While the signal for the single-mode operation remains constant at 20 μV at this frequency, the

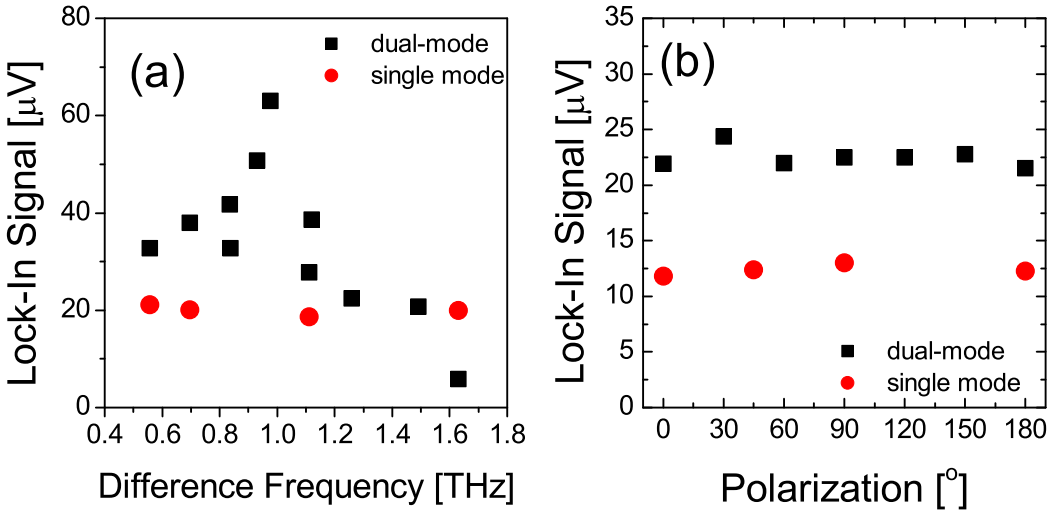

Fig. 6.8: Detected signals (a) as a function of difference frequency of laser modes and (b) as a function of THz polarization at a difference frequency of 1.07 THz

signal for the dual-mode amounts to 5.9 μV which is the noise level of the detection. Even though the upper response-frequency of the bolometer is limited to 1.6 THz, this result depicted in Fig. 6.8(a) indicates that the signals emerging from the SL for the dual-mode operation are probably the THz radiation corresponding to the difference frequencies of the laser modes. It has also been found in the present experiment that the increase in optical power by increasing the injection current induced an increase in the generated signals both for the dual-mode and for the single-mode operation. The amount of increase was more or less of the same magnitude in both cases. However, in spite of the positive signs for the THz generation, the obtained results do not offer clear evidence of the THz generation.

One method to characterize the properties of the eventually generated THz radiation furthermore is to analyze its polarization. To investigate the polarization of the radiation emerging from the SL, a wire-grid THz polarizer is placed directly in front of the bolometer. The laser is driven at an injection current of 500 mA. The difference frequency of the dual-mode operation has been held at 1.07 THz. The polarization direction of the signal has been chosen as zero degree when the signal has the same polarization direction of the laser light. The detected signals for the dual-mode operation are shown in Fig. 6.8(b) as a function of polarization. The signals do not show any polarization dependence and have a constant value of about 22 μV. For comparison, the signals generated at a single-mode operation are also investigated as a function of polarization direction. The detected signal corresponding to the single-mode operation amounts to about 12 μV without any polarization dependence, as expected for

the unpolarized radiation arising from thermal emission. However, the polarization independence of the generated signal for the dual-mode operation is an unexpected result. Because both laser modes are polarized in the same direction, it has been expected that the generated THz radiation shows a well-defined polarization orientation. The polarization independence might indicate that the generated signals in dual-mode operation cannot be associated with the THz radiation corresponding to the difference frequency of the laser modes. As one possibility to investigate the correspondence between the generated signal and the difference frequency of the modes, a bandpass filter which transmits radiation in the frequency range between 150 GHz and 375 GHz has been placed between the laser and the bolometer. The difference frequency has been varied between 185 GHz and 556 GHz. For comparison, the signals under single-mode operation have also been investigated. The measurements showed no significant signals independent of either dual-mode or single-mode operation. The used bandpass filter blocked all the signals emerging from the laser so that the correspondence between the detected signals and the difference frequency cannot be identified yet.

The results obtained in the present investigation indicate two possible explanations. One possibility is the weak power of the generated THz radiation. Because the SL offers no effective waveguide for the THz radiation, the generated THz radiation propagates in all direction in the SL so that much of the THz radiation cannot be guided towards the bolometer. In addition, the THz radiation is absorbed by free-carriers in the SL when the THz radiation propagates through the SL. Therefore, the detected THz radiation is mainly the portion emitted near the rear facet of the SL. The attenuation of the bandpass filter is too high so that no detectable signal can reach the bolometer. In particular, the zero-response of the bolometer to the signal generated in dual-mode operation at a frequency of 1.6 THz indicate that the frequency of the generated signal is above the detectable range of the bolometer. Compared to that, the bolometer responded to the signal under single-mode operation. This indicates the generation of frequency-dependent radiation as the difference frequency of the modes is varied. The decrease of the detected signal above 1 THz can be explained by the fact that the responsivity of the bolometer decreases with the frequency over 1 THz and reaches its limit at the frequency of 1.6 THz. The other possibility is that there is no generation of THz radiation corresponding to the difference frequency of the laser modes. The result of the polarization independence directs towards this possibility. As mentioned above, the generated radiation should exhibit a definite polarization if it is generated due to beating of the modes with a well-defined polarization orientation. In this case, the resonant behavior for the dual-mode operation would be induced by some thermal effect in the SL, which could be distinguished from the case for the single-mode operation. This can also be some resonance effect, for example, due to a waveguide in the Winston cone placed in the bolometer or some mixing effect of the two laser modes occurring

in the detection element of the bolometer. This resonant effect could not be identified in the present experiment yet. Another unsolved question is the zero-response of the bolometer to the signal for the dual-mode operation over the difference frequency of 1.6 THz. This result infers rather direct generation of the THz radiation corresponding to the difference frequency of the laser modes. However, an apparent proof of the direct THz emission could not yet be achieved in the present work.

6.2.3 Summary

In conclusion, a signal for dual-mode operation of a SL distinguishable from that for the single-mode operation has been detected with the bolometer. The radiation shows a frequency dependence, however no well-defined polarization orientation. Furthermore, it cannot be identified by using a bandpass filter. The results allow two possible interpretations: very weak THz radiation corresponding to the difference frequency of the laser modes has been generated, or artefacts which could be induced by either thermal effects in the SL or optical beams reaching the bolometer have been detected. The definite identification could not be achieved in the present experiment. However, the zero-detection above 1.6 THz surmises that the detected signals for dual-mode operation might indeed be a THz signal corresponding to the difference frequency of the laser modes.

To realize and identify the direct THz emission from a SL, it is suggested that some technical methods should be improved. Firstly, the optical beams from the laser must be effectively blocked to lower the background noise without attenuating the THz radiation. Secondly, using a narrow stripe SL with high output power would increase the effectiveness of the direct THz emission because the interaction of the laser modes is confined in the narrow lateral region with high intensity. It is supposed that a SL with higher optical intensity directly generates THz radiation with higher power. Thirdly, the SL itself should be designed and constructed to be appropriate for the direct THz generation, e.g. including a THz waveguide. With such improvements, there is a hope for a simple tunable THz source operating at room temperature.

Chapter 7

Summary – Zusammenfassung

Summary

THz technology attracts increasing interest due to its versatile application possibilities in medical imaging, spectroscopy, THz communication, nondestructive screening, and identification of many chemical elements. For such applications, it is necessary to realize compact and cost-efficient THz sources, which emit a broadband spectrum on the one hand, and can be tuned in frequency with a narrow linewidth on the other hand. Thus, the realization of a compact, cost-efficient and frequency-tunable CW THz radiation source was pursued in this work. As a result, tunable CW THz radiation has been successfully generated via photomixing of two modes emitted from a frequency-tunable dual-mode external cavity semiconductor laser(2λ-ECSL). This achievement is based on the successful realization of frequency-tunable 2λ-ECSLs. The achieved results will be discussed in detail in the following.

In order to realize frequency-tunable dual-mode SL, two concepts were developed. They were based on two double-external-cavity configurations comprising spectrally filtered feedback mechanisms. One concept was a Double-Littman-configuration, in which each of the two desired modes is selected in one of the two external Littman-cavities by means of spectrally filtered feedback. Using an index-guided narrow stripe SL with a maximum output of 50 mW as the gain medium, stable, frequency-tunable dual-mode operation was realized. The difference frequency of the two modes could be changed from 100 GHz to 1.8 THz with a maximum output power of 35 mW and a sidemode suppression ratio of better than 35 dB. Each of the modes contained a single external cavity mode with a linewidth of 60 MHz and could be tuned independently of the other over the entire gain spectrum. The laser emitted spatially a Gaussian intensity distribution. The second concept was a Double-Littrow-configuration. This concept comprises two Littrow-cavities, in each of which the desired mode is selected by spectrally filtered feedback. This configuration provided a particularly compact setup size with high optical feedback strength. By employing a ridge waveguide narrow stripe SL with a maximum output of 120 mW as the gain medium, frequency-tunable dual-mode operation was realized with a difference frequency range from 100 GHz to

10 THz, which is the desired frequency range for THz applications. Each of the two modes contained a single external mode with a linewidth of 120 MHz. A maximum output power of 65 mW was achieved for the dual-mode operation with a sidemode suppression ratio of better than 40 dB. Simultaneous oscillation of the two modes was confirmed for both configurations by intensity autocorrelation measurements.

By using the frequency-tunable 2λ-ECSLs, frequency-tunable CW THz radiation was generated via photomixing of the two laser modes on micro-structured antennas. Two types of antennas were employed to generate THz radiation. One antenna type was a log-periodic toothed antenna (LPTA). The generated THz radiation was quadratically dependent on optical power and photocurrent, as predicted by photomixing theory, which also predicts quadratic dependence of THz radiation on bias voltage of the antenna. The generated THz radiation depended on the bias voltage of the antenna quadratically at low bias and superquadratically at high bias. The superquadratic dependence is due to the superlinear increase of photocurrents at high bias voltage. However, the THz radiation did not exhibit a quadratic dependence on the photocurrent at high bias due to an increase in the DC component of the photocurrent. This increase in DC photocurrent is supposed to be attributed to an increase in carrier lifetime and the contribution of photocarriers with a long lifetime of nanoseconds generated in GaAs substrate. The temporal stability of the generated THz radiation depended on the stability of the optical dual-mode source and was stable over several tens of minutes. Measurements using a Fourier-Transform-Spectrometer confirmed a single THz spectrum with a frequency corresponding to the difference frequency of the two incident laser modes. The linewidth of the generated THz radiation was narrower than the linewidth of each of the optical modes, which is attributed to the common-mode rejection effect of the laser modes experiencing the same fluctuations. This linewidth-narrowing is an advantage of the dual-mode laser compared to the method using two independent lasers, for which the linewidth of the generated THz radiation is the sum of each of the linewidths of the lasers. The generated THz radiation exhibited broadband performance up to about 3 THz. The limit of operating bandwidth is given by the carrier lifetime and capacitance of the photomixer. Furthermore, the THz radiation exhibited nearly linear polarization, the orientation of which depended on the frequency. The frequency dependence of the performance and polarization of THz radiation follows the frequency-characteristics of the LPTA. The conversion efficiency from optical to THz radiation amounted to 10^{-7}. This low efficiency was mainly attributed to the low quantum efficiency of the photomixer and to the impedance mismatch between the photomixer and the antenna. As second antenna type, a H-dipole antenna was used to generate THz radiation. The THz radiation exhibited a resonance behavior around 890 GHz, the resonance frequency of which was given by the geometric dimension of the dipole.

Spectroscopic application of the generated THz radiation showed that THz radiation penetrates non-metallic and non-polar materials such as plastics and wood. Furthermore, the absorption lines of HCl and H_2O were spectroscopically identified. This is the first successful application of CW THz radiation generated by using a dual-mode SL for identification of chemical elements.

For THz applications, high power THz radiation sources are desirable. Since the THz radiation power is quadratically proportional to the incident optical power, higher power of THz radiation can be achieved by using lasers with higher output power. Broad area semiconductor lasers (BALs) generally provide optical output power up to several watts, however, they exhibit poor beam quality due to a multitude of lateral modes. Therefore, dual-mode emission of BALs with controlled mode-characteristics is a challenge for high quality optical sources. By using a commercial BAL as the gain medium in a Double-Littman-configuration (2λ-ECBAL), frequency-tunable dual-mode operation was achieved from 100 GHz to 1 THz with output powers up to 220 mW. Using an antireflection-coated BAL, the tuning range was extended up to 3 THz. By applying a mechanism of spectrally and spatially filtered feedback in the external cavity, longitudinal and lateral modes of the BAL could be controlled. Consequently, mode-controlled dual-mode operation of the BAL was achieved up to an output power of 90 mW, where each of the two laser modes contained a single longitudinal mode with a fundamental lateral mode. However, the beam quality decreased with increasing output power due to oscillation of high-order lateral modes, filamentation and thermal lensing at high optical powers. Investigations of intensity autocorrelation showed constant performance of intensity modulation of the 2λ-ECBAL over a large range of injection currents and detuning frequencies. Additionally, THz photocurrent modulation in the photomixer was estimated using intensity autocorrelation measurements. The AC component of the photocurrent amounted to more than 85 % of the total photocurrent. By photomixing of two modes emitted from the 2λ-ECBAL, THz radiation was generated. The conversion efficiency was lower than that for the case employing a narrow stripe 2λ-ECSL, which is attributed to a lower coupling efficiency of THz radiation into free space and into the bolometer in the experimental investigations. The achieved results indicate that the spectrally and spatially controlled 2λ-ECBAL is a promising high-power laser source for the generation of THz radiation via photomixing.

An interesting phenomenon occurring for dual-mode operation in narrow stripe SLs is the four-wave mixing (FWM) process. The FWM process originates from the nonlinear interaction of the optical field within the semiconductor medium and provides a possibility for spectroscopic methods in the frequency-domain for the study of ultrafast carrier dynamics in SLs. The investigations in this work have shown that the simultaneous oscillation of two modes induces the cascaded generation of new waves,

which are enhanced due to the cavity resonances of the solitary laser. It has been found that ultrafast carrier dynamics such as carrier heating and spectral hole burning are responsible for the nonlinear optical process in the detuning range of several hundred GHz. The newly generated waves reach their maximum power when the power ratio of the two modes is about ±6 dB. The conversion efficiency of the FWM process is minimal when both modes have equal power. Moreover, the conversion efficiency decreases with an increase in total power, which is attributed to the reduction of the free carrier density due to stimulated recombination in the SL.

The nonlinear optical processes in the SL indicate the possibility of direct generation of THz radiation in the SL itself. In the investigations for direct generation of THz radiation in 2λ-ECBAL, a signal was detected for dual-mode operation of the BAL with the bolometer, which was distinguishable from the signal under single-mode operation. The signal showed a frequency dependence, however, its definite frequency could not be identified by using a bandpass filter. Furthermore, the signal exhibited no well-defined polarization orientation. These results allow for two possible interpretations: very weak THz radiation or some unidentified artefacts. The definite identification could not be achieved in this work. For realization and definite identification of the direct THz emission from a SL, some technical improvements remain as a task for future work: better bandpass filter, high power narrow stripe SL as the gain medium, and structural design of SLs aimed for the direct THz generation. With such improvements, there is a hope for a simple tunable THz radiation source operating at room temperature.

The results achieved in this work show that frequency-tunable dual-mode external cavity semiconductor lasers provide generation of temporally and spectrally stable, frequency-tunable CW THz radiation via photomixing. With further improvements, such as mechanical stabilization, higher-power SL, and more efficient antennas, the realized THz radiation source is a promising source for commercial THz applications such as spectroscopy, imaging, and screening.

Zusammenfassung

THz Technologie zieht wegen ihrer vielseitigen Anwendungsmöglichkeiten wie Bildgebung, Spektroskopie, THz-Kommunikation, zerstörungsfreiem Durchleuchten und Identifikation von vielen chemischen Elementen zunehmendes Interesse an. Für solche Anwendungen ist es nötig, kompakte und kostengünstige THz-Strahlungsquellen zu realisieren, die sowohl ein breitbandiges Spektrum emittieren, als auch mit einer schmalen Linienbreite frequenzdurchstimmbar sind. Diese Arbeit verfolgt die Realisierung einer kompakten, kostengüstigen und frequenzdurchstimmbaren Dauerstrich-THz-Strahlungsquelle. Als Ergebnis wurde durchstimmbare Dauerstrich-THz-Strahlung unter Verwendung von Photomischen der beiden Moden eines frequenzdurchstimmbaren Zwei-Moden-Halbleiterlasers erfolgreich generiert. Dieser Erfolg basiert auf der erfolgreichen Realisierung von frequenzdurchstimmbaren Zwei-Moden-Halbleiterlasern mit externen Resonatoren (2λ-ECSL). Die erzielten Ergebnisse werden im Folgenden im Detail diskutiert.

Um einen frequenzdurchstimmbaren Zwei-Moden-Halbleiterlaser zu realisieren, wurden in dieser Arbeit zwei Konzepte entwickelt. Diese Konzepte basieren auf zwei externen Doppel-Resonator-Konfigurationen, die einen spektral selektiven Rückkopplungsmechanismus beinhalten. Ein Konzept ist eine Doppel-Littman-Konfiguration, wobei jeweils eine von zwei gewünschten Moden in jedem externen Resonator durch spektral gefilterte Rückkopplung selektiert wird. Unter Verwendung eines indexgeführten Schmalstreifen-Halbleiterlasers, mit einer maximalen Ausgangsleistung von 50 mW als Verstärkungsmedium, wurde stabile, frequenzdurchstimmbare Zwei-Moden-Emission realisiert. Die Differenzfrequenz beider Moden konnte von 100 GHz bis 1.8 THz variiert werden, mit einer maximalen Ausgangsleistung von 35 mW und einer Seitenmodenunterdrückung von mehr als 35 dB. Jede Mode bestand aus einer einzelnen externen Resonatormode mit einer Linienbreite von 60 MHz und konnte unabhängig von einander auf dem ganzen Verstärkungsspektrum abgestimmt werden. Die räumliche Intensitätsverteilung des Lasers war gaussförmig. Das andere Konzept ist eine Doppel-Littrow-Konfiguration. Das Konzept enthält zwei Littrow-Resonatoren, wobei in jedem von ihnen eine der gewünschten Moden durch spektral gefilterte Rückkopplung selektiert wird. Diese Konfiguration bietet insbesondere einen kompakten Aufbau and eine hohe optische Rückkopplungsstärke. Unter Verwendung eines Ridge-Waveguide Schmalstreifen-Halbleiterlasers mit einer maximalen Ausgangsleistung von 120 mW konnte durchstimmbarer Zwei-Moden-Betrieb realisiert werden, mit einem Differenzfrequenzbereich von 100 GHz bis 10 THz. Dieser abstimmbare Bereich ist der erwünschte Frequenzbereich für THz-Anwendungen. Jede der zwei Moden bestand aus einer einzelnen externen Mode mit einer Linienbreite von 120 MHz. Eine maximale Ausgangsleistung von 65 mW wurde für den Zwei-Moden-Betrieb erziehlt, mit einer Seiten-

modenunterdrückung von mehr als 40 dB. Simultanes Anschwingen beider Moden ist für beide Konfigurationen durch Intensitätsautokorrelationsmessungen nachgewiesen worden.

Frequenzdurchstimmbare THz-Strahlung wurde durch Photomischen zweier Lasermoden auf Mikrostruktur-Antennen generiert, wobei frequenzdurchstimmbare Zwei-Moden-Halbleiterlaser (2λ-ECSLs) verwendet wurden. Zwei Sorten von Antennen wurden für die Erzeugung von THz-Strahlung verwendet. Eine Antenne war eine logarithmisch-periodische, gezahnte Antenne (LPTA). Die erzeugte THz-Strahlung war quadratisch abhängig von der optischen Leistung und dem Photostrom, wie es von der Photomisch-Theorie vohergesagt wird. Die Photomisch-Theorie sagt auch eine quadratische Abhängigkeit der THz-Strahlung von der an der Antenne angelegten Vorspannung voraus. Die erzeugte THz-Strahlung zeigte bei niedriger Vorspannung eine quadratische Spannungsabhängigkeit, bei höherer Vorspannung aber eine superquadratische Abhängigkeit. Die superquadratische Abhängigkeit beruht auf dem superlinearen Anstieg des Photostroms bei hoher Vorspannung, diese wiederum einhergehend mit einem Anstieg der Ladungsträger-Lebenszeit. Die THz-Strahlung weist jedoch, infolge eines Anstiegs des Gleichstromsanteils im Photostrom, bei hoher Vorspannung keine quadratische Abhängigkeit vom Photostrom mehr auf. Dieser Anstieg des Gleichstroms ist vermutlich die Folge eines Anstiegs der Ladungsträger-Lebenszeit und eines Beitrags von langlebigen Ladungsträgern mit einer Lebenszeit von einigen Nanosekunden, die im GaAs-Substrat erzeugt wurden. Die Stabilität der erzeugten THz-Strahlung war abhängig von der Stabilität der optischen Zwei-Moden-Quelle und blieb länger als einige zehn Minuten stabil. Messungen mit dem Fourier-Spektrometer bestätigten einen einzelnen THz-Peak mit der Frequenz, die der Differenzfrequenz der eingestrahlten optischen Moden entspricht. Die Linienbreite der generierten THz-Strahlung war schmaler als die Linienbreite der einzelnen optischen Moden. Dies beruht auf dem sogenannten 'Common-Mode Rejection Effect' zweier Lasermoden, die gleichen Fluktuationen unterliegen. Dieses Einengen der Linienbreite ist ein Vorteil von Zwei-Moden-Lasern, im Gegensatz zu Methoden, die zwei getrennte Laser benutzen. Bei dieser letzteren Methode ist die Linienbreite der erzeugten THz-Strahlung die Summe der Linienbreiten der jeweiligen Laser. Die erzeugte THz-Strahlung zeigte breitbandige Leistung bis zu 3 THz. Die Arbeitsbandbreite ist begrenzt durch die Ladungsträger-Lebensdauer und die Kapazität des Photomischers. Darüber hinaus zeigte die THz-Strahlung eine frequenzabhängige Polarisationsrichtung. Die Frequenzabhängigkeit von Leistung und Polarisation folgt den Frequenzchakteristiken der LPTA. Die Konversionseffizienz von optischem Licht zu THz-Strahlung betrug 10^{-7}. Diese niedrige Effizienz beruht auf der niedrigen Quanteneffizienz vom Photomischer und der Impedanz-Fehlanpassung zwischen dem Photomischer und der Antenne. Als zweite Antenne wurde eine H-Dipolantenne für die Erzeugung von THz-Strahlung benutzt. Die erzeugte THz Strah-

lung zeigte ein Resonanzverhalten bei einer Frequenz um 890 GHz. Diese Resonanzfrequenz war durch die geometrische Dimension des Dipols gegeben.

Die spektroskopische Anwendung von THz-Strahlung zeigte, dass THz-Strahlung nichtmetallische und nicht-polarisierte Materialen wie Kunststoffe und Holz durchdringt. Darüber hinaus wurden Absorptionslinien von HCl und H_2O identifiziert. Dies ist die erste erfolgreiche Anwendung zur Identifikation von chemischen Elementen mit Dauerstrich-THz-Strahlung, die durch einen Zwei-Moden-Halbleiterlaser erzeugt wurde.

Für THz-Anwendungen sind THz-Quellen mit hoher Leistung erwünscht. Da die THz-Leistung proportional zu der quadratischen Leistung des einfallenden Lichtes ist, kann höhere THz-Leistung durch Verwendung von Lasern mit höherer Ausgangsleistung erzielt werden. Breitstreifenhalbleiterlaser (BAL) emittieren allgemein hohe Ausgangsleistungen von einigen Watt, jedoch zeigen BAL schlechte Strahlqualitäten wegen ihrer lateralen Multimodigkeit. Daher ist Zwei-Moden-Emission mit kontrollierten Modencharakteristiken eine Herausforderung für optische Quellen mit hoher Qualität. Unter Verwendung eines kommeziellen BALs in einer Doppel-Littman-Konfiguration (2λ-ECBAL) wurde frequenzdurchstimmbarer Zwei-Moden-Betrieb von 100 GHz bis 1 THz mit einer Ausgangsleistung von bis zu 220 mW erzielt. Unter Verwendung eines antireflektions-beschichteten BAL wurde der durchstimmbare Bereich bis auf 3 THz erweitert. Longitudinale und laterale Moden von BALn konnten durch spektrale und räumliche Filterungsmechanismen im externen Resonator kontrolliert werden. Somit wurde modenkontrollierter Zwei-Moden-Betrieb mit einer Ausgangsleistung bis zu 90 mW erzielt, wobei jede Lasermode aus einer einzelnen longitudinalen Mode mit einer fundamentalen lateralen Mode bestand. Allerdings hat sich die Strahlqualität wegen dem Anschwingen von lateralen Moden, Filamentation und thermischer Linsenbildung bei noch höherer optischer Leistung mit zunehmender Ausgangsleistung verschlechtert. Untersuchungen von Intensitätsautokorrelationen zeigten konstantes Verhalten der Intensitätsmodulation von 2λ-ECBAL über einen breiten Bereich von Pumpströmen und Verstimmungungsfrequenzen. Ausserdem wurde die THz-Modulation vom Photostrom im Photomischer durch die Intensitätsautokorrelationsmessungen abgeschätzt. Der Wechselstromanteil des Photostroms betrug über 85 % des gesamten Photostroms. THz-Strahlung wurde durch Photomischen zweier Moden aus dem 2λ-ECBAL erzeugt. Die Konversionseffizienz war niedriger als der Wert, der mit dem Schmalstreifenlaser 2λ-ECSL erzielt worden ist. Diese niedrige Effizienz liegt vermutlich an der schlechten Kopplungseffizienz von THz-Srahlung an das Bolometer. Die erzielten Ergebnisse zeigen jedoch, dass der spektral und räumlich kontrollierte 2λ-ECBAL für die Erzeugung von THz-Strahlung durch Photomischen eine vielversprechende Hochleistungslaserquelle ist.

Ein interessantes Phänomen, das bei Zwei-Moden-Betrieb von Schmalstreifenlasern

auftritt, ist ein Vier-Wellen-Mischen-Prozess (FWM-Prozess). Der FWM-Prozess entsteht aus der nichtlinearen Wechselwirkung vom optischen Feld mit dem Halbleitermedium und bietet eine spektroskopische Methode im Frequenzbereich zur Untersuchung von ultraschneller Dynamik in Halbleiterlasern. Die Untersuchungen in dieser Arbeit zeigten, dass das simultane Anschwingen zweier Moden eine Kaskadenentstehung von neuen Wellen veranlasst, die durch die Resonanz des solitären Lasers verstärkt werden. Hierbei ist ultraschnelle Ladungsträgerdynamik, wie Ladungsträgeraufheizung und spektrales Lochbrennen, für die nichtlinearen optischen Prozesse in der Verstimmungsfrequenz von einigen hundert GHz verantwortlich. Die neu entstandenen Wellen erreichen ihr Maximum, wenn das Leistungsverhältniss zweier Moden $\pm 6\,\mathrm{dB}$ beträgt. Die Konversionseffizienz von FWM-Prozess ist minimal, wenn die beiden Moden die gleiche Leistung haben. Darüber hinaus nimmt die Konversionseffizienz mit Zunahme der Gesamtleistung ab. Diese Abnahme der Konversionseffizienz beruht auf der, durch die stimulierte Rekombination verursachten, Abnahme der freien Ladungsträgerdichte im Halbleiterlaser.

Die nichtlinearen optischen Prozesse im Halbleiterlaser deuten die Möglichkeit von Direkterzeugung von THz-Strahlung im Halbleiterlaser selbst an. Bei Untersuchungen der Direkterzeugung von THz-Strahlung in 2λ-ECBALn wurde unter Zwei-Moden-Betrieb ein Signal mit dem Bolometer detektiert, das sich von dem Signal unter Einmoden-Betrieb unterscheidet. Das Signal zeigte eine Frequenzabhängigkeit, dennoch konnte dessen Frequenz mit Hilfe eines Bandpassfilters nicht identifiziert werden. Außerdem zeigten das Signal keine feste Polarisationsrichtung. Diese Ergebnisse deuten zwei Möglichkeiten an: Eine sehr schwache THz-Strahlung oder ein nicht identifiziertes Artefakt. Eine eindeutige Identifizierung konnte in dieser Arbeit nicht erzielt werden. Um direkte THz-Emission in Halbleiterlasern zu realisieren und identifizieren, müssen einige technische Verbesserungen wie bessere Bandpassfilter, Verwendung von Schmalstreifen-Halbleiterlaser mit hoher Leistung als Verstärkungsmedium, und strukturelle Konstruktion von Halbleiterlasern gezielt für die direkte THz-Erzeugung vorgenommen werden. Mit solchen Verbesserungen ist auf die Realisierung einer bei Zimmertemperatur arbeitenden, einfachen THz-Strahlungsquelle zu hoffen.

Die in dieser Arbeit erzielten Ergebnisse zeigen, dass frequenzdurchstimmbare Zwei-Moden-Halbleiterlaser mit externen Resonatorkonfigurationen durch Photomischen zeitlich und spektral stabile, frequenzdurchstimmbare Dauerstrich-THz-Strahlung erzeugen. Mit weiteren Verbesserungen wie mechanischer Stabilisierung, Halbleiterlaser mit hoher Leistung und effizienteren Antennen ist die realisierte THz-Quelle eine vielversprechende Strahlungsquelle für kommerzielle Anwendungen wie Spektroskopie, Bildgebung und Durchleuchten.

Bibliography

[1] D. H. Auston, Appl. Phys. Lett. **26**, 101 (1975).

[2] P. H. Siegel, IEEE Trans. Microwave Theory Tech. **50**, 910 (2002).

[3] B. B. Hu and M. C. Nuss, Opt. Lett. **20**, 1716 (1995).

[4] A. W. M. Lee and Q. Hu, Opt. Lett. **30**, 2563 (2005).

[5] K. Kawase, Y. Ogawa, and Y. Watanabe, Opt. Express **11**, 2549 (2003).

[6] E. Pickwell and V. P. Wallace, J. Phys. D: Appl. Phys. **39**, R301 (2006).

[7] M. Nagel, P. H. Bolivar, M. Brucherseifer, and H. Kurz, Appl. Phys. Lett. **80**, 154 (2002).

[8] R. A. Kaindl, M. A. Carnahan, D. Hägele, R. Löwenich, and D. S. Chemla, Nature **423**, 734 (2003).

[9] S. Verghese, K. A. McIntosh, S. D. Calawa, W. F. Dinatale, E. K. Duerr, and K. A. Molvar, Appl. Phys. Lett. **73**, 384 (1998).

[10] S. Kono, M. Tani, and K. Sakai, IEE Proc. Optoelectron. **149**, 105 (2002).

[11] Q. Wu and X.-C. Zhang, Appl. Phys. Lett. **68**, 1604 (1996).

[12] C. Winnewisser, P. U. Jepsen, M. Schall, V. Schyja, and H. Helm, Appl. Phys. Lett. **70**, 3069 (1997).

[13] G. Mourou, C. V. Stancampiano, and D. Blumenthal, Appl. Phys. Lett. **38**, 470 (1981).

[14] D. H. Auston, K. P. Cheung, and P. R. Smith, Appl. Phys. Lett. **45**, 284 (1984).

[15] L. Xu, X.-C. Zhang, and D. H. Auston, Appl. Phys. Lett. **61**, 1784 (1992).

[16] X.-C. Zhang, B. B. Hu, J. T. Darrow, and D. H. Auston, Appl. Phys. Lett. **56**, 1011 (1990).

[17] R. Ascázubi, I. Wilke, K. Denniston, H. Lu, and W. J. Schaff, Phys. Lett. **84**, 4810 (2004).

[18] A. Bonvalet, M. Joffre, J.-L. Martin, and A. Migus, Appl. Phys. Lett. **67**, 2907 (1995).

[19] Y. R. Shen, Prog. Quant. Electr. **4**, 207 (1976).

[20] K. Kawase, J.-I. Shikata, K. Imai, and H. Ito, Appl. Phys. Lett. **78**, 2819 (2001).

[21] R. Köhler, A. Tredicucci, F. Beltram, H. E. Beere, E. H. Linfield, A. G. Davies, D. A. Ritchie, R. C. Iotti, and F. Rossi, Nature **417**, 156 (2002).

[22] E. R. Brown, F. W. Smith, and K. A. McIntosh, J. Appl. Phys. **73**, 1480 (1993).

[23] F. Siebe, K. Siebert, R. Leonhardt, and H. G. Roskos, IEEE J. Quantum Electron. **35**, 1731 (1999).

[24] J. M. Battiato, T. F. Morse, and R. K. Kostuk, IEEE Photon. Technol. Lett. **9**, 913 (1997).

[25] R. M. Sova, C.-S. Kim, and J. U. Kang, IEEE Photon. Technol. Lett. **14**, 287 (2002).

[26] C.-L. Wang and C.-L. Pan, Appl. Phys. Lett. **64**, 3089 (1994).

[27] S. Ito, M. Suehiro, T. Hirata, and T. Hidaka, IEEE Photon. Technol. Lett. **7**, 959 (1995).

[28] S. Pajarola, G. Guekos, and J. Mørk, IEEE Photon. Technol. Lett. **8**, 157 (1996).

[29] C.-F. Lin, M.-J. Chen, and B.-L. Lee, IEEE Photon. Technol. Lett. **10**, 1208 (1998).

[30] J. Struckmeier, A. Euteneuer, B. Smarsly, M. Breede, M. Born, M. Hofmann, L. Hildebrand, and J. Sacher, Opt. Lett. **24**, 1573 (1999).

[31] M. Brunner, K. Gulden, R. Hövel, M. Moser, J. F. Carlin, R. P. Stanley, and M. Ilegems, IEEE Photon. Technol. Lett. **12**, 1316 (2000).

[32] F. Rogister, D. W. Sukow, A. Gavrielides, P. Mégret, O. Deparis, and M. Blondel, Opt. Lett. **25**, 808 (2000).

[33] C.-C. Huang, C.-H. Cheng, Y.-S. Su, and C.-F. Lin, IEEE Photon. Technol. Lett. **16**, 371 (2004).

[34] A. Yariv, *Quantum Electronics,* 3rd ed. (Wiley, New York, 1989).

[35] C. E. Wieman and L. Hollberg, Rev. Sci. Instrum. **62**, 1 (1991).

[36] P.-J. Rigole, S. Nilsson, L. Bäckbom, T. Klinga, J. Wallin, B. Stålnacke, E. Berglind, and B. Stoltz, IEEE Photon. Technol. Lett. **7**, 697 (1995).

[37] T. W. Hänsch, Appl. Opt. **11**, 895 (1972).

[38] M. G. Littman and H. J. Metcalf, Appl. Opt. **17**, 2224 (1978).

[39] M. G. Littman, Opt. Lett. **3**, 138 (1978).

[40] K. Liu and M. G. Littman, Opt. Lett. **6**, 117 (1981).

[41] K. C. Harvey and C. J. Myatt, Opt. Lett. **16**, 910 (1991).

[42] H. Tabuchi and H. Ishikawa, Electron. Lett. **26**, 742 (1990).

[43] M. Sargent III, M. O. Scully, and W. E. Lamb, Jr., *Laser Physics* (Addison-Wesley, London, 1974).

[44] A. E. Siegman, *Lasers* (Universtity Science, Mill Valley, Califonia, 1985).

[45] W. Elsäßer and E. O. Göbel, IEEE J. Quantum Electron. QE-**25**, 687 (1985).

[46] C.-F. Lin and P.-C. Ku, IEEE J. Quantum Electron. **32**, 1377 (1996).

[47] M. Matus, M. Kolesik, J. V. Moloney, M. Hofmann, and S. W. Koch, J. Opt. Soc. Am. B **21**, 1758 (2004).

[48] J.-F. Lepage and N. McCarthy, Appl. Opt. **41**, 4347 (2002).

[49] L. Hsu, L. Chi, S. Wang, and C.-L. Pan, Opt. Commun. **168**, 195 (1999).

[50] T. Heil, I. Fischer, and W. Elsäßer, Phys. Rev. A **60**, 634 (1999).

[51] M. Yousefi and D. Lenstra, IEEE J. Quantum Electron. **35**, 970 (1999).

[52] A. P. A. Fischer, O. K. Andersen, M. Yousefi, S. Stolte, and D. Lenstra, IEEE J. Quantum Electron. **36**, 375 (2000).

[53] T. Heil, I. Fischer, and W. Elsäßer, Phys. Rev. Lett. **87**, 243901 (2001).

[54] A. P. A. Fischer, M. Yousefi, D. Lenstra, M. W. Carter, and G. Vemuri, IEEE J. Select. Topics Quantum Electron. **10**, 944 (2004).

[55] D. W. Sukow, M. C. Hegg, J. L. Wright, and A. Gavrielides, Opt. Lett. **27**, 827 (2002).

[56] C.-L. Wang and C.-L. Pan, Opt. Lett. **20**, 1292 (1995).

[57] M. O. Ziegler, M. Münkel, T. Burkhard, G. Jennemann, I. Fischer, and W. Elsässer, J. Opt. Soc. Am. B **16**, 2015 (1999).

[58] M. Tani, O. Morikawa, S. Matsuura, and M. Hangyo, Semicond. Sci. Technol. **20**, S151 (2005).

[59] I. S. Gregory, C. Baker, W. R. Tribe, I. V. Bradley, M. J. Evans, E. H. Linfield, A. G. Davies, and M. Missous, IEEE J. Quantum Electron. **41**, 717 (2005).

[60] R. H. Kingston, *Detection of Optical and Infrared Radiation* (Springer-Verlag, Berlin, 1978).

[61] W. L. Stutzman and G. A. Thiele, *Antenna Theory and Design,* 2nd ed. (Wiley, New York, 1998).

[62] X. Liu, A. Prasad, J. Nishio, E. R. Weber, Z. Liliental-Weber, and W. Walukiewicz, Appl. Phys. Lett. **67**, 279 (1995).

[63] S. Gupa, M. Y. Frankel, J. A. Vladmanis, J. F. Whitaker, G. A. Mourou, F. W. Smith, and A. R. Calawa, Appl. Phys. Lett. **59**, 3276 (1991).

[64] S. Gupa, J. F. Whitaker, and G. A. Mourou, IEEE J. Quantum Electron. **28**, 2464 (1992).

[65] K. M. Yu, M. Kaminska, and Z. Liliental-Weber, J. Appl. Phys. **72**, 2850 (1992).

[66] M. Kaminska, Z. Liliental-Weber, E. R. Weber, T. George, J. B. Kortright, F. W. Smith, B. Tsaur, and A. R. Calawa, Appl. Phys. Lett. **54**, 1881 (1989).

[67] D. C. Look, Thin Solid Films **231**, 61 (1993).

[68] K. A. McIntosh, K. B. Nichols, S. Verghese, and E. R. Brown, Appl. Phys. Lett. **70**, 353 (1997).

[69] D. C. Look, D. C. Walters, M. Q. Manashreh, J. R. Sizelove, C. E. Stutz, and K. R. Evans, Phys. Rev. B **42**, 3578 (1990).

[70] I. S. Gregory, C. Baker, W. R. Tribe, M. J. Evans, H. E. Beere, E. H. Linfield, A. G. Davies, and M. Missous, Appl. Phys. Lett. **83**, 4199 (2003).

[71] A. C. Warren, J. M. Woodall, P. D. Kirchner, X. Yin, F. Pollak, M. R. Melloch, N. Otsuka, and K. Mahalingam, Phys. Rev. B **46**, 4617 (1992).

[72] A. J. Lochtefeld, M. R. Melloch, J. C. P. Chang, and E. S. Harmon, Appl. Phys. Lett. **69**, 1465 (1996).

[73] M. Stellmacher, J.-P. Schnell, D. Adam, and J. Nagle, Appl. Phys. Lett. **74**, 1239 (1999).

[74] G. Segschneider, F. Jacob, T. Löffler, H. G. Roskos, S. Tautz, P. Kiesel, and G. Döhler, Phys. Rev. B **65**, 125205 (2002).

[75] H. Němec, A. Pashkin, P. Kužel, M. Khazan, S. Schnüll, and I. Wilke, J. Appl. Phys. **90**, 1303 (2001).

[76] C. A. Balanis, *Antenna Theory: Analysis and Design,* 2nd ed. (Wiley, New York, 1997).

[77] V. H. Rumsey, IRE Nat. Convent. Record **5**, 114 (1957).

[78] Y. Mushiake, *Self-Complementary Antennas* (Springer-Verlag, Berlin, 1996).

[79] R. H. DuHamel and D. Isbell, IRE Nat. Convent. Record **5**, 119 (1957).

[80] D. B. Rutledge and M. S. Muha, IEEE Trans. Antennas Propag. AP-**30**, 535 (1982).

[81] D. F. Filipovic, S. S. Gearhart, and G. M. Rebeiz, IEEE Trans. Microwave Theory Tech. **41**, 1738 (1993).

[82] J. V. Rudd, J. L. Johnson, and D. M. Mittleman, J. Opt. Soc. Am. B **18**, 1524 (2001).

[83] J. V. Rudd and D. M. Mittleman, J. Opt. Soc. Am. B **19**, 319 (2002).

[84] I. S. Gregory, W. R. Tribe, B. E. Cole, M. J. Evans, E. H. Linfield, A. G. Davies, and M. Missous, Appl. Phys. Lett. **85**, 1622 (2004).

[85] The log-periodic circular-toothed antenna has been fabricated by C. Sydlo at Institut für Hochfrequenztechnik, Technische Universität Darmstadt.

[86] R. Mendis, C. Sydlo, J. Sigmund, M. Feiginov, P. Meissner, and H. L. Hartnagel, Solid-State Electronics **48**, 2041 (2004).

[87] C. Sydlo, Private communication, Institut für Hochfrequenztechnik, Technische Universität Darmstadt.

[88] The simulation has been performed by C. Sydlo. Institut für Hochfrequenztechnik, Technische Universität Darmstadt.

[89] B. K. Kormanyos, P. H. Ostdiek, W. Bishop, T. W. Crowe, and G. M. Rebeiz, IEEE Trans. Microwave Theory Tech. **41**, 1730 (1993).

[90] M. M. Gitin, F. W. Wise, G. Arjavalingam, Y. Pastol, and R. C. Compton, IEEE Trans. Antennas Propag. **42**, 1738 (1994).

[91] H. Ohtake, Y. Suzuki, N. Sarukura, S. Ono, T. Tsukamoto, A. Nakanishi, M. L. Stock, M. Yoshida, and H. Endert, Jpn. J. Appl. Phys. **40**, L 1223 (2001).

[92] P. L. Richards, J. Appl. Phys. **76**, 1 (1994).

[93] A. J. Kreisler and A. Gaugue, Supercond. Sci. Technol. **13**, 1235 (2000).

[94] R. J. Bell, *Introductory Fourier Transform Spectroscopy* (Academic Press, New York, 1972).

[95] K. D. Möller and W. G. Rothschild, *Far-Infrared Spectroscopy* (Wiley, New York, 1971).

[96] S. Bakić, Diploma thesis, Institut für Angewandte Physik, Technische Universität Darmstadt (2004).

[97] K. A. McIntosh, E. R. Brown, K. B. Nichols, O. B. McMahon, W. F. DiNatale, and T. M. Lyszczarz, Appl. Phys. Lett. **67**, 3844 (1995).

[98] E. R. Brown, Appl. Phys. Lett. **75**, 1480 (1999).

[99] E. R. Brown, K. A. McIntosh, F. W. Smith, K. B. Nichols, M. J. Manfra, C. L. Dennis, and J. P. Mattita, Appl. Phys. Lett. **64**, 3311 (1994).

[100] J. P. Ibbetson and U. K. Mishra, Appl. Phys. Lett. **68**, 3781 (1996).

[101] N. Zamdmer, Q. Hu, K. A. McIntosh, and S. Verghese, Appl. Phys. Lett. **75**, 2313 (1999).

[102] R. Wipf, Diploma thesis, Physikalisches Institut, Johann Wolfgang Goethe-Universität Frankfurt (2005).

[103] J. J. Kuta, H. M. van Driel, and D. Landheer, Appl. Phys. Lett. **64**, 140 (1994).

[104] E. Chen and S. Y. Chou, Appl. Phys. Lett. **70**, 140 (1997).

[105] E. H. Böttcher, E. Dröge, D. Bimberg, A. Umbach, H. Engel, and M. Collischon, IEEE Photonics Technol. Lett. **9**, 809 (1997).

[106] P. G. Huggard, C. J. Shaw, J. A. Cluff, and S. R. Andrew, Appl. Phys. Lett. **72**, 2069 (1998).

[107] P. Gu, M. Tani, M. Hyodo, K. Sakai, and T. Hidaka, Jpn. J. Appl. Phys. **37**, L976 (1998).

[108] A. Lisauskas, Private communication, Physikalisches Institut, Johann Wolfgang Goethe-Universität Frankfurt.

[109] R. Mendis, C. Sydlo, J. Sigmund, M. Feiginov, P. Meissner, and H. L. Hartnagel, IEEE Antennas and Wireless Propag. Lett. **4**, 85 (2005).

[110] S. Matsuura, M. Tani, and K. Sakai, Appl. Phys. Lett. **70**, 559 (1997).

[111] J. E. Bjarnason, T. L. J. Chan, A. W. M. Lee, M. A. Celis, and E. R. Brown, Appl. Phys. Lett. **85**, 519 (2004).

[112] A. S. Pine, R. D. Suenram, E. R. Brown, and K. A. McIntosh, J. Mol. Spectrosc. **175**, 37 (1996).

[113] M. van Exter, C. Fattinger, and D. Grischkowsky, Optics Lett. **14**, 1128 (1989).

[114] D. M. Mittleman, R. H. Jacobsen, R. Neelamani, R. G. Baraniuk, and M. C. Nuss, Appl. Phys. B **67**, 379 (1998).

[115] S. Matsuura, M. Tani, H. Abe, K. Sakai, H. Ozeki, and S. Saito, J. Mol. Spectrosc. **187**, 97 (1998).

[116] T. Ikeda, A. Matsushita, M. Tatsuno, Y. Minami, M. Yamaguchi, K. Yamamoto, M. Tani, and M. Hangyo, Appl. Phys. Lett. **87**, 034105 (2005).

[117] T. Klaus, S. P. Belov, and G. Winnewisser, J. Mol. Spectrosc. **187**, 109 (1998).

[118] J. K. Messer, F. C. D. Lucia, and P. Helminger, Int. J. of Infrared and Millimeter Waves **4**, 505 (1983).

[119] J. R. Marciante and G. P. Agrawal, IEEE J. Quantum Electron. **32**, 590 (1996).

[120] G. H. B. Thompson, Opto-electronics **4**, 257 (1972).

[121] I. Fischer, O. Hess, W. Elsässer, and E. Göbel, Europhys. Lett. **35**, 579 (1996).

[122] J. Martin-Regaldo, S. Balle, and N. B. Abraham, IEE Proc.-Optoelecron. **143**, 17 (1996).

[123] J. R. Marciante and G. P. Agrawal, IEEE Photon. Technol. Lett. **10**, 54 (1998).

[124] T. Burkhard, M. O. Ziegler, I. Fischer, and W. Elsässer, Chaos, Solitons & Fract **10**, 845 (1999).

[125] T. Burkhard, *Raum-zeitliche Dynamik von Breitstreifenlasern auf Pikosekunden Zeitskalen,* Dissertation (Shaker Verlag, Aachen, 2000).

[126] S. K. Mandre, I. Fischer, and W. Elsässer, Opt. Lett. **28**, 1135 (2003).

[127] S. K. Mandre, I. Fischer, and W. Elsässer, Opt. Commun. **244**, 355 (2005).

[128] J. Kaiser, *Raumzeitliche Ladungsträger- und Modendynamik von Breitstreifen-Halbleiterlasern auf Piko- und Subpikosekunden-Zeitskalen,* Dissertation (Shaker Verlag, Aachen, 2005).

[129] R. Menzel, *Photonics: Linear & Nonlinear Interactions of Laser Light and Matter* (Springer-Verlag, Berlin, 2001).

[130] Y. Liu, S.-G. Park, and A. M. Weiner, Opt. Lett. **21**, 1762 (1996).

[131] C. Simmendinger, D. Preißer, and O. Hess, Opt. Express **99**, 48 (1999).

[132] G. L. Abbas, S. Yang, and V. W. S. Chan, Opt. Lett. **12**, 605 (1987).

[133] E. Samsøe, P. E. Andersen, S. Anderson-Engels, and P. M. Petersen, Opt. Express **12**, 609 (2004).

[134] V. Raab and R. Menzel, Opt. Lett. **27**, 167 (2002).

[135] S. Wolff, A. Rodionov, V. E. Sherstobitov, and H. Fouckhardt, IEEE J. Quantum Electron. **39**, 448 (2003).

[136] J.-C. Diels and W. Rudolph, *Fundamentals, Techniques, and Applications on a Femtosecond Time Scale* (Academic Press, San Diego, 1996).

[137] D. F. Geraghty, R. B. Lee, M. Verdiell, M. Ziari, A. Mathur, and K. J. Vahala, IEEE J. Select. Topics Quantum Electron. **3**, 1146 (1997).

[138] M. C. Tatham, G. Sherlock, and L. D. Westbrook, Electron. Lett. **28**, 1851 (1993).

[139] M. P. Kesler and E. P. Ippen, Appl. Phys. Lett. **51**, 1765 (1987).

[140] P. A. Franken, A. E. Hill, C. W. Peters, and G. Weinreich, Phys. Rev. Lett. **7**, 118 (1961).

[141] Y. R. Shen, *The Principles of Nonlinear Optics* (Wiley, New York, 1984).

[142] G. P. Agrawal, J. Opt. Soc. Am. B **5**, 147 (1988).

[143] R. Nietzke, P. Panknin, W. Elsäßer, and E. O. Göbel, IEEE J. Quantum Electron. **25**, 1399 (1989).

[144] R. Nietzke, W. Elsäßer, A. N. Baranov, and K. Wünstel, Appl. Phys. Lett. **58**, 554 (1991).

[145] L. F. Tiemeijer, Appl. Phys. Lett. **59**, 499 (1991).

[146] K. Kikuchi, M. Kakui, C.-E. Zah, and T.-P. Lee, IEEE J. Quantum Electron. **28**, 151 (1992).

[147] A. Uskov, J. Mørk, and J. Mark, IEEE J. Quantum Electron. **30**, 1769 (1994).

[148] A. Mecozzi, S. Scotti, A. D'Ottavi, E. Iannone, and P. Spano, IEEE J. Quantum Electron. **31**, 689 (1995).

[149] J. Zhou, N. Park, J. W. Dawson, K. Vahala, M. A. Newkirk, and B. I. Miller, Appl. Phys. Lett. **63**, 1179 (1993).

[150] K. L. Hall, J. Mark, E. Ippen, and G. Eisenstein, Appl. Phys. Lett. **56**, 1740 (1990).

[151] G. P. Agrawal, IEEE J. Quantum Electron. **QE-23**, 860 (1987).

[152] R. Paiella and K. J. Vahala, Appl. Phys. Lett. **66**, 2619 (1995).

[153] S. Murata, A. Tomita, J. Shimizu, M. Kitamura, and A. Suzuki, Appl. Phys. Lett. **58**, 1458 (1991).

[154] J. G. Provost and R. Frey, Appl. Phys. Lett. **55**, 519 (1989).

[155] S. Jiang and M. Dagenais, Appl. Phys. Lett. **62**, 2757 (1993).

[156] G. P. Agrawal, Appl. Phys. Lett. **51**, 302 (1987).

[157] R. Nietzke, P. Fenz, W. Elsäßer, and E. O. Göbel, Appl. Phys. Lett. **51**, 1298 (1987).

[158] M. P. Kesler and E. P. Ippen, Electronics Letters **25**, 640 (1989).

[159] A. D'Ottavi, F. Girardin, L. Graziani, F. Martelli, P. Spano, A. Mecozzi, S. Scotti, R. Dall'Ara, J. Eckner, and G. Guekos, IEEE J. Select. Topics Quantum Electron. **3**, 522 (1997).

[160] G. P. Bava, P. Debernardi, and G. Osella, IEE Proc. Optoelectron. **141**, 119 (1996).

[161] I. Koltchanov, S. Kindt, K. Petermann, S. Diez, R. Ludwig, R. Schnabel, and H. G. Weber, Appl. Phys. Lett. **68**, 2787 (1996).

[162] A. D'Ottavi, E. Iannone, A. Mecozzi, S. Scotti, P. Spano, R. Dall'Ara, G. Guekos, and J. Eckner, Appl. Phys. Lett. **65**, 2633 (1994).

[163] A. D'Ottavi, E. Iannone, A. Mecozzi, S. Scotti, P. Spano, J. Landreau, A. Ougazzaden, and J. C. Bouley, Appl. Phys. Lett. **64**, 2492 (1994).

[164] N. C. Kothari and D. J. Blumenthal, IEEE J. Quantum Electron. **32**, 1810 (1996).

[165] A. D'Ottavi, A. Mecozzi, S. Scotti, F. C. Romeo, F. Martelli, P. Spano, R. Dall'Ara, J. Eckner, and G. Guekos, Appl. Phys. Lett. **67**, 2753 (1995).

[166] A. D'Ottavi, F. Martelli, P. Spano, A. Mecozzi, S. Scotti, R. Dall'Ara, J. Eckner, and G. Guekos, Appl. Phys. Lett. **68**, 2186 (1996).

[167] G. P. Agrawal, Opt. Lett. **12**, 260 (1987).

[168] S. Hoffmann, M. Hofmann, E. Bründermann, M. Havenith, M. Matus, J. V. Moloney, A. S. Moskalenko, M. Kira, S. W. Koch, S. Saito, and K. Sakai, Appl. Phys. Lett. **84**, 3585 (2004).

[169] M. Kira, W. Hoyer, and S. W. Koch, Solid State Commun. **129**, 733 (2004).

[170] M. Kira, W. Hoyer, and S. W. Koch, Phys. Stat. Sol. (b) **238**, 443 (2003).

Acknowledgements - Danksagung

Ich möchte mich bei allen herzlich bedanken, die zum Gelinge dieser Arbeit beigetragen haben bzw. mir zu einer schönen Zeit in der Arbeitsgruppe Halbleiteroptik verholfen haben. Ich danke

Herrn Prof. Dr. Wolfgang Elsäßer für die freundliche Aufnahme in die Arbeitsgruppe, die hervorrangenden Arbeitsbedingungen, die Freiheit, meine Arbeit eigenverantwortlich durchführen zu können, sowie die exzellente Betreuung meiner Doktorarbeit.

Herrn Dr. Ingo Fischer für die engagierte Betreuung meiner Arbeit mit wertvollen fachlichen Diskussionen sowie die vielen Ratschläge bei alltäglichen Angelegenheiten. Du hast mich bei allen Problemen in der AG HLO immer mit Geduld und großem Verständnis unterstützt.

Herrn Prof. Dr. Peter Meißner für das Interesse an meiner Arbeit und die freundliche Übernahme des Zweitgutachtens.

Allen Projektpartnern des THz-Verbundprojektes:
Ich danke Herrn Prof. Dr. Hartmut G. Roskos, Dr. Alvydas Lisauskaus, Gabriel Loata, Dr. Torsten Löffler und Dr. Karsten Siebert an der Johann Wolfgang Goethe-Universität Frankfurt am Main für die wertvolle Zusammenarbeit und die fruchtbaren fachlichen Diskussionen über die THz-Welt.
Ich danke Herrn Prof. Dr. Hans L. Hartnagel, Prof. Dr. Peter Meißner, Dr. Michael Feiginov, Dr. Rajind Mendis, Dr. Jochen Sigmund und Dr. Cezary Sydlo im Fachbereich Elektrotechnik, TU Darmstadt, für die fruchtbare Zusammenarbeit und die freundliche Bereitstellung von Antennen. Ich danke auch Herrn Dr. Kabula Mutamba für das unzählige Bonding von Antennen.

Herrn Robert Wipf für die Hilfestellung und die umfangreichen Diskussionen über die THz-Problematik nicht nur an der Uni Frankfurt sondern auch an der TU Darmstadt.

Meinem Diplomanden Herrn Saša Bakić für den Beitrag zu meiner Arbeit und die Unterstützung bei der Modifikation des alten FT-Spektrometers.

Herrn Dr. Tilman Groth, Dr. Joachim Kaiser, Dr. Shyam Mandre und Jens von Staden für die schöne gemeinsame Doktorandenzeit, die kulinarische Ausflüge, die gegenseitige Unterstützung bei sowohl physikalischen als auch alltäglichen Problemen und insbesondere die unzähligen Korrekturen bei sprachlichen Formulierungen. Ich danke

Herrn Dr. Tobias Gensty und Dr. Michael Peil für die Hilfsbereitschaft bei Problemen jeglicher Art in der gemeinsamen Doktorandenzeit, die stetige Kaffeeversorgung und das schärfste Pepperoni-Pulver. Ich danke auch allen restlichen ehemaligen und neuen Mitgliedern der AG HLO Andreas Barchanski, Klaus Becker, Sebastian Berning, Richard Birkner, Martin Blazek, Dominik Blömer, Matthias Breuer, Stefan Breuer, Dr. Christian Degen, Lukas Drzewietzki, Erol Durmus, Hartmut Erzgräber, Christian Fuchs, Boris Gromann, Dr. Tilmann Heil, Karl Koch, Dr. Harald Lehmberg, Markus Merkel, (dem Ehrenmitglied) Dr. Kristian Motzek, Philip Kappe, Wolfgang Rick, Sandra Würtenberger und Eric Wille für das angenehme Arbeitsklima bei AG HLO.

Herrn Karl-Heinz Vetter und allen Mitgliedern der Mechanikwerkstatt für die hervorrangende Beratung und Herstellung vieler opto-mechanischer Komponenten. Ich danke Herrn Gerhard Jourdan für die Bereitstellung vieler chemischer Substanzen und die Elektronenmikroskop-Aufnahmen von Antennen und Lasern.

Herrn Günter Gräfe und Ulrich Baumann von der Elektronikwerkstatt für die Beratung und zügige Bearbeitung im elektronischen Bereich. Ich danke Herrn Günter Schmutzler für die Hilfe bei Problemen mit dem Computer.

Herrn Dagobert Freytag von der Helium-Anlage für die zügige Versorgung mit flüssigem Helium.

Frau Roswitha Jaschik, Petra Gebert und Maria Teresa Musso für die Unterstützung bei allen Verwaltungsaufgaben und die netten Gespräche. Ich danke auch Frau Barbara Hackel für die hervorrangende Bearbeitung von Grafiken und Bildern.

Herrn Dr. Götz Erbert für die freundliche Bereitstellung der FBH-Laser.

Der Deutschen Forschungsgemeinschaft für die finanzielle Unterstützung des THz-Projektes.

Der größte Dank gilt meiner Familie, insbesondere meinen Eltern, meiner Frau Eun-Hee und meiner Tochter Sol. Ich danke Euch recht herzlich für Eure unerschöpfliche Unterstützung in jeder Hinsicht während meiner Studien- und Doktorandenzeit. Ich habe das größte Glück, mein Leben mit Euch zu führen. Ohne Euch wäre das alles sicherlich nicht möglich gewesen.

Curriculum Vitae

Icksoon Park
Waltherstr. 1
64289 Darmstadt

Geburtsdatum:	29.10.1964
Geburtsort:	Yeonsan/Südkorea
Staatsangehörigkeit:	koreanisch
1980-1983:	Hansung High School
1983:	Abitur
1983-1987:	Studium Nuclear Engineering an Hanyang University, Seoul/Südkorea
1987:	Bachelor of Science
1987-1989:	Militärdienst in Südkorea
1992-2001:	Physik-Studium an der TU Darmstadt
2001:	Diplomarbeit in der AG Halbleiteroptik bei Prof. Elsäßer: *Quantenrauschen elektrisch gekoppelter Leuchtdioden: Untersuchung zu Korrelationen des Intensitätsrauschens* Physik-Diplom
2001-2006:	Wissenschaftlicher Mitarbeiter in der AG Halbleiteroptik, Institut für Angewandte Physik, TU Darmstadt
2001-2007:	Promotionsstudent in der AG Halbleiteroptik, Institut für Angewandte Physik, TU Darmstadt